CHALMERS
UNIVERSITY OF TECHNOLOGY

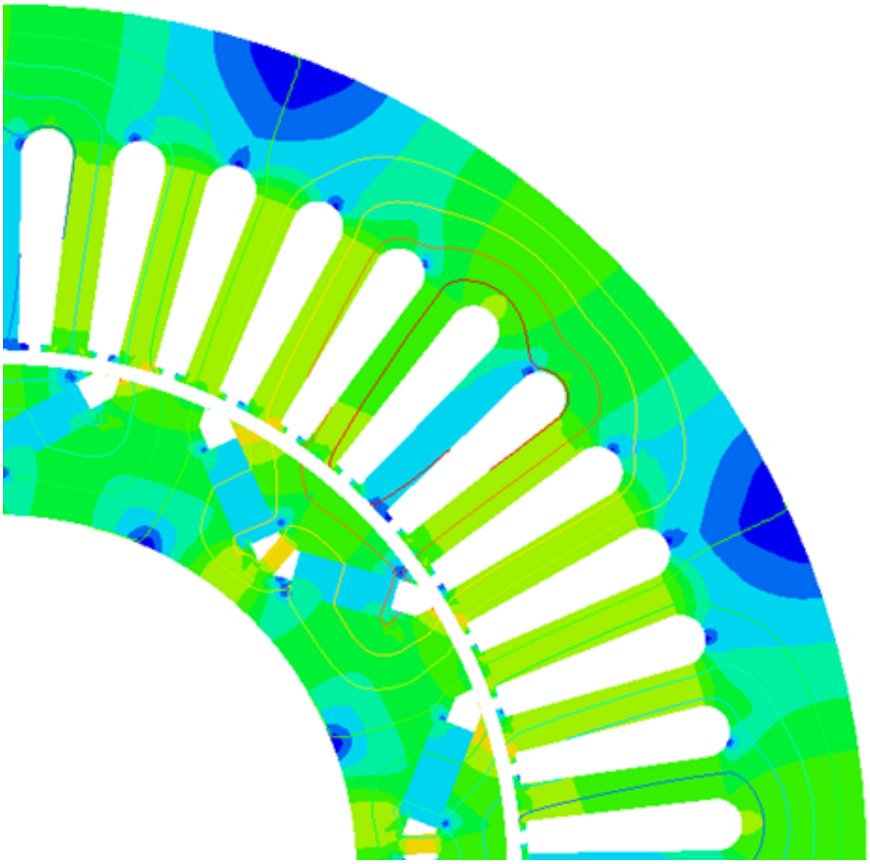

Efficiency Optimization of Electric Drives with Variable Switching Frequency using Wide-Bandgap Motor Drives

Master's thesis in Mobility Engineering

SHIJIE ZHANG, PRANAV KATTA

DEPARTMENT OF ELECTRICAL ENGINEERING
CHALMERS UNIVERSITY OF TECHNOLOGY
Gothenburg, Sweden 2023
www.chalmers.se

Master's thesis 2023

Efficiency Optimization of Electric Drives with Variable Switching Frequency using Wide-Bandgap Motor Drives

Shijie Zhang
Pranav Katta

CHALMERS
UNIVERSITY OF TECHNOLOGY

Department of Electrical Engineering
Chalmers University of Technology
Gothenburg, Sweden 2023

Efficiency Optimization of Electric Drives with Variable Switching Frequency using Wide-Bandgap Motor Drives

SHIJIE ZHANG
PRANAV KATTA

Supervisor: Sepideh Amirpour, Department of High Voltage & Climate, China Euro Vehicle Technology AB
Examiner: Torbjörn Thiringer, Department of Electrical Engineering, Chalmers University of Technology

Master's Thesis 2023
Department of Electrical Engineering
Division of Electric Power Engineering
Chalmers University of Technology
SE-412 96 Gothenburg
Telephone +46 31 772 1000

Typeset in LaTeX
Printed by Chalmers Reproservice
Gothenburg, Sweden 2023

Efficiency Optimization of Electric Drives with Variable Switching Frequency using Wide-Bandgap Motor Drives

SHIJIE ZHANG
PRANAV KATTA
Department of Electrical Engineering
Chalmers University of Technology

Abstract

The quest for increased energy efficiency for electrified vehicle propulsion systems has led to the adoption of fast-switching Wide Band Gap (WBG) motor drives. As research continues to focus on improving energy efficiency, the necessity arises to construct entire model, conduct co-simulation and analyze the power losses for these drive systems.

The proposed work in this thesis presents a comprehensive investigation into the overall efficiency of an electric drive system, employed by variable switching frequency for sinusoidal pulse-width modulation (SPWM) over selected operating conditions. Utilizing ANSYS software tools, a drive system model containing an interior permanent magnet synchronous machine (IPMSM), a 3-phase inverter circuit, and a control system are developed.

A preliminary study is carried out to compare the finite element analysis simulation with numerical calculations of the fundamental losses in the IPMSM when subjected to a sinusoidal power supply. The results illustrate the different control strategies that can be implemented, with the maximum torque per ampere (MTPA) method identified as ideal for the analysis.

The process is subsequently repeated where the power is supplied through an SPWM-controlled 3-phase inverter operating under the same set of conditions. The inverter-motor losses are obtained for different switching frequencies at each tested operating point in the speed-torque envelope. The total energy efficiency of the inverter circuit and motor is determined for each operating point and corresponding switching frequency. Finally, the analysis produces an optimal switching frequency map, identifying the most efficient configuration for the entire drive system.

Keywords: Electric Vehicle, FEM, PMSM, Power Inverter Circuit, PWM Control, Switching Frequency, MTPA Control, Efficiency Map

Acknowledgements

First, we would like to thank our supervisor, industrial PhD student Sepideh Amirpour, for her weekly guidance on our design proposal and the provision of literature. Second, we like to thank our examiner, professor Torbjörn Thiringer, for his suggestion and correction on our thesis work. Last but not least, We also want to thank everyone who has given us advice for our thesis, including senior lecturer Stefan Lundberg, industrial PhD student Yu Xu and postdoc student Nimananda Sharma, etc.

At the same time, we also want to thank our friends, colleagues in CEVT, and other master thesis students for their help in our study and other daily life.

Shijie Zhang & Pranav Katta, Gothenburg, August 2023

List of Acronyms

AC	Alternating Current
BEV	Battery Electric Vehicle
DC	Direct Current
EMF	Electromotive Force
EV	Electric Vehicle
FEM	Finite Element Method
FFT	Fast Fourier Transformation
FOC	Field-Oriented Control
FW	Field Weakening
ICEV	Internal Combustion Engine Vehicle
IGBT	Insulated-Gate Bipolar Transistor
IPMSM	Interior Permanent Magnet Synchronous Machine
IM	Induction Machine
LIB	Lithium-ion Battery
MOSFET	Metal-Oxide Field Effect Transistor
MTPA	Maximum Torque Per Ampere
MTPV	Maximum Torque Per Volt
PI	Proportional Integral
PM	Permanent Magnet
PMSM	Permanent Magnet Synchronous Motor
PWM	Pulse Width Modulation
RMS	Root Mean Square
SiC	Silicon Carbide
SPMSM	Surface Mounted Permanent Magnet Synchronous Machine
SPWM	Sinusoidal Pulse Width Modulation
SVPWM	Space Vector Pulse Width Modulation
THIPWM	Third harmonic injection pulse width modulation
VSI	Voltage Source Inverter
WBG	Wide-Bandgap

Nomenclature

$\hat{\psi_m}$	Estimated Magnetic Flux Linkage [Wb]
α_c	Bandwidth of Closed-Loop System [rad/s]
β	Angle of Stator Current [rad]
θ_r	Transformation Angle [rad]
λ_{lew}	Permeance Factor of Axial Length of End Winding
λ_{Wew}	Permeance Factor of Coil Span of End Winding
μ_0	Vacuum Permeability [Wb/A·m]
μ_r	Relative Permeability [Wb/A·m]
ρ	Resistivity [Ω·m]
ρ_{cu}	Mass Density of Copper [kg/m^3]
ρ_{fe}	Mass Density of Iron [kg/m^3]
σ	Conductivity [S/m]
ψ	Phase Angle Between Stator Voltage and Current [rad]
ψ_d	Flux Linkage in d-direction [Wb]
ψ_m	Flux Linkage from Magnets [Wb]
ψ_q	Flux Linkage in q-direction [Wb]
Ω_r	Mechanical Speed of Rotor [rad/s]
ω_r	Electrical Speed of Rotor [rad/s]
$\hat{L_{sd}}$	Estimated Stator Inductance in d-Direction [H]
$\hat{L_{sq}}$	Estimated Stator Inductance in q-Direction [H]
A_{strand}	Cross-Section Area [m^2]
a	Major Radius of Voltage-Limited Ellipse
B	Viscous Damping Constant
B_1	Duct Thickness [mm]
B_m	Amplitude of Magnetic Flux Density [T]
B_{s0}	Slot Opening Width [mm]
B_{s1}	Slot Wedge Maximum Width [mm]
B_{s2}	Slot Body Bottom Width [mm]
b	Minor Radius of Voltage-Limited Ellipse
C_{iss}	Input Capacitance [C]
C_{oss}	Output Capacitance [C]
C_{rss}	Reverse Transfer Capacitance [C]
D_1	Limited Diameter of PM Ducts [mm]
E_{offD}	Turn-Off Energy Losses in Diode [J]
E_{offM}	Turn-Off Energy Losses in MOSFET [J]

E_{onD}	Turn-On Energy Losses in Diode [J]
E_{onM}	Turn-On Energy Losses in MOSFET [J]
f	Frequency of Magnetic Flux Density [Hz]
f_{el}	Fundamental Frequency of Motor [Hz]
f_{sw}	Switching Frequency [Hz]
H	Magnet Magnitude [A/m]
H_{s0}	Slot Opening Height [mm]
H_{s01}	Slot Closed Bridge Height [mm]
H_{s1}	Slot Wedge Height [mm]
H_{s2}	Slot Body Height [mm]
I_{Drms}	RMS Value of MOSFET On-State Current [A]
I_{DS}	Drain-Source Current [A]
I_{d0}	Current of Center of Voltage-Limited Ellipse [A]
I_F	Current Through Diode [A]
I_{Fav}	Average Value of Diode Current [A]
I_{Frms}	RMS Value of Diode Current [A]
I_{max}	Maximum Branch Current [A]
I_{min}	Minimum Branch Current [A]
I_o	Peak Current [A]
I_{ref}	Reference Drain-Source Current [A]
i_{mag}	Amplitude of Stator Current [A]
i_s	Stator Current [A]
$i_{s,max}$	Maximum Magnitude of Stator Current [A]
i_{sd}	Stator Current in d-Direction [A]
i_{sq}	Stator Current in q-Direction [A]
J	Rotational Inertia of Rotor [kg·m^2]
J_e	Eddy Current Density in Permanent Magnets [A/m^2]
J_e^*	Complex Conjugate of J_e
k_c	Coefficient of Classical Eddy Current Loss
k_e	Coefficient of Excess Loss
k_i	Coefficient of PI Controller
k_h	Coefficient of Hysteresis Loss
k_p	Coefficient of PI Controller
L	Motor Depth [mm]
L_s	Stator Inductance [H]
L_{sd}	Stator Inductance in d-direction [H]
L_{sq}	Stator Inductance in q-direction [H]
$L_{s,w}$	End Winding Leakage Inductance [H]
l_a	Active Length Per Coil [m]
l_{ew}	Axial Length of End Winding [m]
l_w	End Winding Length Per Coil [m]
M_a	Amplitude Modulation Index
m	Number of Phase
$N_{parallel}$	Number of parallel branches Per Phase
N_{strand}	Number of Strands Per Turn
N_{turn}	Number of Turns Per Coil

n	Branch Number
n_{max}	Maximum Operating Speed [rpm]
n_p	Pole Pair Number
n_r	Mechanical Speed of Rotor [rpm]
n_s	Mechanical Synchronous Speed [rpm]
O_1	Bottom Width for Separate Duct [mm]
O_2	Distance from Duct Bottom to Shaft Surface [mm]
P_b	Blocking Losses [W]
P_c	Conduction Losses [W]
P_{cD}	Instantaneous Conduction Loss in Diode [W]
$P_{cD,avg}$	Average Conduction Loss in Diode [W]
P_{cM}	Instantaneous Conduction Loss in MOSFET [W]
$P_{cM,avg}$	Average Conduction Loss in MOSFET
P_{cu}	Copper Losses [W]
P_e	Electromagnetic Power [W]
P_{fe}	Iron Losses [W]
$P_{fe,c}$	Classical Eddy Current Loss [W]
$P_{fe,e}$	Excess Loss [W]
$P_{fe,h}$	Hysteresis Loss [W]
P_l	Total Losses within Inverter [W]
$P_{mag,e}$	Eddy Current Loss in Permanent Magnets
P_{rated}	Rated Power [W]
P_{sw}	Switching Losses [W]
P_{swM}	Switching Losses in MOSFET [W]
P_{swMoff}	Turn-Off Switching Losses in MOSFET [W]
P_{swMon}	Turn-On Switching Losses in MOSFET [W]
P_{swD}	Switching Losses in Diode [W]
p	Frequency Ratio
Q	Number of Coils
Q_{rr}	Reverse-Recovery Charge [C]
q	Number of Slots Per Pole Per Phase
R_a	Active Resistance [Ω]
R_{ad}	Active Resistance in d-Direction [Ω]
R_{aq}	Active Resistance in q-Direction [Ω]
R_D	Diode On-State Resistance [Ω]
R_{DSon}	Drain-Source On-State Resistance [Ω]
R_s	Winding Resistance Per Phase [Ω]
$R_{th,JC}$	Thermal Resistance from Virtual Junction to Case [K/W]
$R_{th,CH}$	Thermal Resistance from Case to Heatsink [K/W]
$R_{th,HA}$	Thermal Resistance from Heatsink to Ambient Condition [K/W]
r	Number of Winding Layers
S	Slew Rate [V/μS]
T_A	Ambient Temperature [K]
T_C	Case Temperature [K]
T_e	Output Electromagnetic Torque [N·m]
T_H	Heatsink Temperature [K]

T_J	Junction Temperature [K]
T_L	Load Torque [N·m]
T_{PM}	Alignment Torque [N·m]
T_R	Reluctance Torque [N·m]
T_{sw}	Switching Cycle [s]
t_{fu}	Voltage-Fall Time [s]
t_{ri}	Current-Rise Time [s]
U_{DC}	DC-Link Voltage [V]
U_{Dr}	Drive Output Voltage [V]
U_{ref}	Reference Drain-Source Voltage [V]
U_D	Voltage Across Diode [V]
U_{D0}	Diode On-State Zero-Current Voltage
U_{DS}	Drain-Source Voltage Drop [V]
U_{GS}	Gate-Source Voltage [V]
$U_{GS,th}$	Threshold of Gate-Source Voltage [V]
u_s	Stator Voltage [V]
$u_{s,max}$	Maximum Magnitude of Stator Voltage [V]
u_{sd}	Stator Voltage in d-Direction [V]
u_{sq}	Stator Voltage in q-Direction [V]
V	Volume of Permanent Magnets [m^3]
W_{ew}	Coil Span of End Winding [m]

Contents

1
Introduction

The transportation sector is one of the major contributors to greenhouse gas emissions, and the move towards electrification of vehicles is seen as a promising solution to mitigate this problem. However, in the present day, improving the energy efficiency of electric propulsion systems in battery electric vehicles (BEVs) remains a significant challenge.

The key components of an electric drive include the electric machine, responsible for transforming the electric energy into mechanical energy, and the power inverter circuit, which converts direct current (DC) from the power electrical battery into alternating current (AC) to power the electric machine.

1.1 Problem Background

The growing demand for various types of AC electric machines within the market is primarily attributed to the exceptional performances of the permanent magnet synchronous motors (PMSMs). This motor type is favored for its remarkable power density, impressive torque-to-current ratio, and high energy efficiency[1]. Moreover, the WBG silicon carbide metal-oxide-semiconductor field-effect transistors (SiC-MOSFETs) have substantially shown superior performance when compared to the conventional insulated-gate bipolar transistor (IGBT) inverter systems[2]. Therefore, nowadays, the research efforts have increasingly concentrated on the investigation of WBG SiC-based inverter drive systems in the domain of BEVs.

However, the driving range of BEVs before requiring recharging and the limitations imposed by the initial investment costs are gradually acting as main worries for vehicle consumers. Enhancing the energy efficiency of the entire motor drive system has the capacity to address these concerns, as it can result in reduced energy consumption, thereby extending the vehicle's range and lowering total expenses[3].

In the past years, various studies have been conducted to improve the energy efficiency of SiC MOSFET-based motor drives. One example is the introduction of an improved control strategy based on the flatness properties for PMSM-based EVs[4]. Additionally, the alterable current flux-weakening angle has been identified as a contributing factor in ensuring efficiency enhancement[5]. However, these studies have usually overlooked the impact of the switching frequency of inverters on the overall system energy efficiency.

1.2 Purpose and Contribution

By employing an IPMSM in combination with a WBG SiC-based inverter technology, the objective of this thesis is to minimize the overall power losses across the electric drive system, with a primary focus on the variable switching frequencies and slew rates. This thesis also aims to achieve an optimal switching frequency scheme through investigating various operating regions of the IPMSM.

Based on the finite element method (FEM), a detailed electric drive system is going to be constructed and simulated to achieve comprehensive power losses data for the IPMSM. Moreover, different current vector control strategies will be developed for IPMSM and evaluated in terms of their feasibility and efficiency. Finally, the optimal strategy will be identified and adopted for conducting the co-simulation process.

To meet sustainability targets, it is critical for reducing carbon emissions to improve the energy efficiency of BEVs. By optimizing the drive system components, a reduction in power losses and an enhancement in overall energy efficiency can be observed. This advancement could increase the driving range, making BEVs more practical and competitive in comparison with traditional internal combustion engine vehicles. Additionally, this thesis has the potential to the advancement of WBG Sic-based inverter technology, which could find broader applications beyond electric vehicles.

2
Theoretical Background

This chapter outlines the overview of the essential theoretical background related to the components of the electric powertrain system for BEVs. The discussion contains the electric machine, the 3-phase inverter circuit, the control techniques and the diverse power loss types within the entire drive system.

2.1 Electric Powertrain System

The basic arrangement of an electric powertrain consists of a drive system powered by a rechargeable battery pack. The drive system includes an AC machine connected to a power inverter circuit, responsible for converting DC power from the battery into AC power, as shown in Fig.2.1. The research of this thesis is based on the characteristics of the electric machine, the inverter circuit and the controller, all of which will be comprehensively discussed in the following sections.

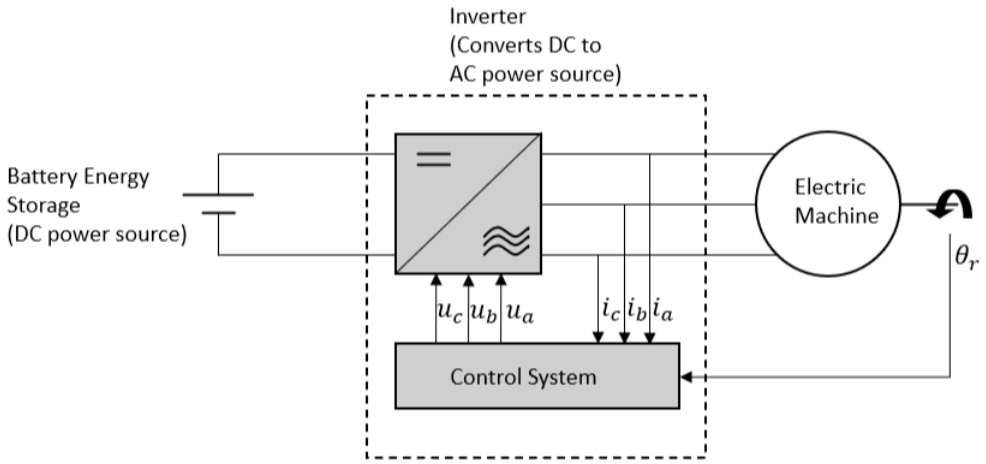

Figure 2.1: Basic layout of an electric powertrain system in BEVs

2.2 Electric Machine

2.2.1 Basic Structure and Working Principle

In simple terms, an electric machine is a device that transforms electromagnetic energy into mechanical rotating motion[6]. The fundamental components of an electric

machine mainly include:

- Stator: As the name describes, the stator is the stationary part of the motor that surrounds the rotor. It comprises a core created by stacking thin lamination sheets and houses a set of insulated wire windings arranged in a particular pattern. These windings receive power from an external AC source, generating a rotating magnetic field that interacts with the rotor.

- Rotor: The rotor is a rotating part of the motor responsible for driving an external shaft load. Based on the rotor structure, an electric machine can be classified as an induction machine or a permanent magnet machine.

- Shaft: The shaft serves as a link between the mechanical power produced by the motor and the shaft load. It is constructed from high-strength materials capable of withstanding the demands of high torque and speed applications.

A PMSM is an electric machine that applies permanent magnets (PMs) to establish a consistent field within the rotor, which subsequently interacts with the revolving magnetic field produced by the stator and generating motion. In this type of machine, the rotor is constructed using thin lamination sheets with high magnetic permeability, and these sheets are arranged in various configurations alongside PMs.

The PMSM can be mainly categorized into surface-mounted PMSMs (SPMSMs) and IPMSMs, as depicted in Fig.2.2. This thesis will entirely focus on the IPMSM, a specific type where the rotor incorporates embedded PMs to achieve higher torque density within the machine, brought about by the rise in its saliency[7]. The PMs are positioned in a manner that directs the magnetic flux from the north pole to the south pole, spanning through the stator. Moreover, the design and attributes of the IPMSM makes it a highly promising selection for applications in vehicles.

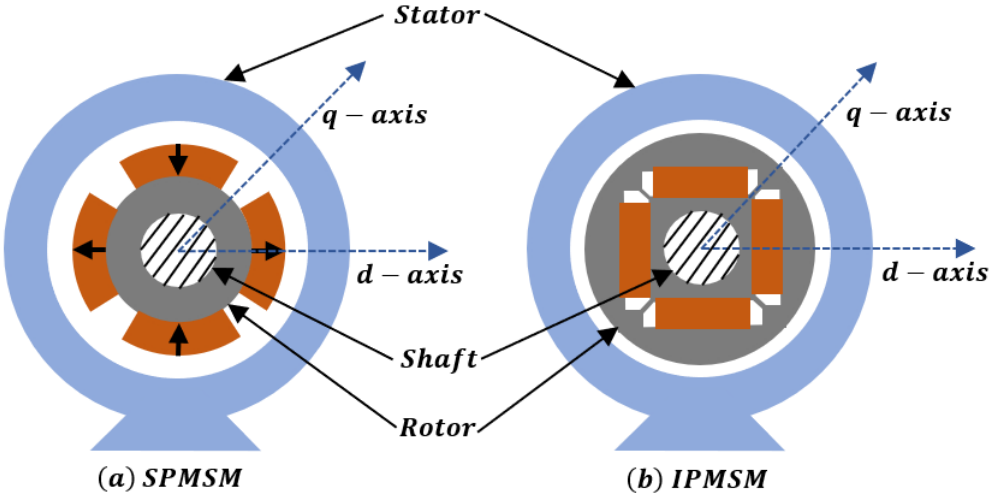

Figure 2.2: Structure of PMSM: SPMSM (left) and IPMSM (right)

In order to induce the rotating motion of the rotor, a rotating magnetic flux is

generated in the stator with a 3-phase AC current source. Through the interaction of the magnetic fields of the stator and rotor, the rotor aligns itself with the stator's magnetic field. Therefore, the rotational speed of rotor matches the magnetic field of stator, thus giving rise to the term "synchronous motor".

2.2.2 Transformation Form for Space Vectors

In electric machines, the electrical properties involve 3-phase alternating variables, which can complicate the control of the machine. In order to simplify this process, the transformation for space vectors can be introduced as follows

$$\begin{bmatrix} x_\alpha(t) \\ x_\beta(t) \end{bmatrix} = \frac{1}{K} \begin{bmatrix} \frac{2}{3} & -\frac{1}{3} & -\frac{1}{3} \\ 0 & \frac{1}{\sqrt{3}} & -\frac{1}{\sqrt{3}} \end{bmatrix} \begin{bmatrix} x_a(t) \\ x_b(t) \\ x_c(t) \end{bmatrix} \tag{2.1}$$

$$\begin{bmatrix} x_d(t) \\ x_q(t) \end{bmatrix} = \begin{bmatrix} \cos(\theta_r) & \sin(\theta_r) \\ -\sin(\theta_r) & \cos(\theta_r) \end{bmatrix} \begin{bmatrix} x_\alpha(t) \\ x_\beta(t) \end{bmatrix} \tag{2.2}$$

where x_a, x_b and x_c represent the space vectors of electrical quantities in the 3-phase coordinate system; x_α and x_β are recorded from the alpha-beta ($\alpha\beta$-) coordinate system; x_d and x_q are derived from the direct-quadrature (dq-) coordinate system; θ_r represents the transformation angle, which is based on that the rotor flux is oriented in d- direction. Through the Clark transformation (2.1), a 3-phase quantity can be transformed into 2-phase space vectors in a stationary system. Afterwards, the 2-phase space vector can be further transformed into a rotating system by Park transformation (2.2). These processes are clearly illustrated in Fig.2.3.

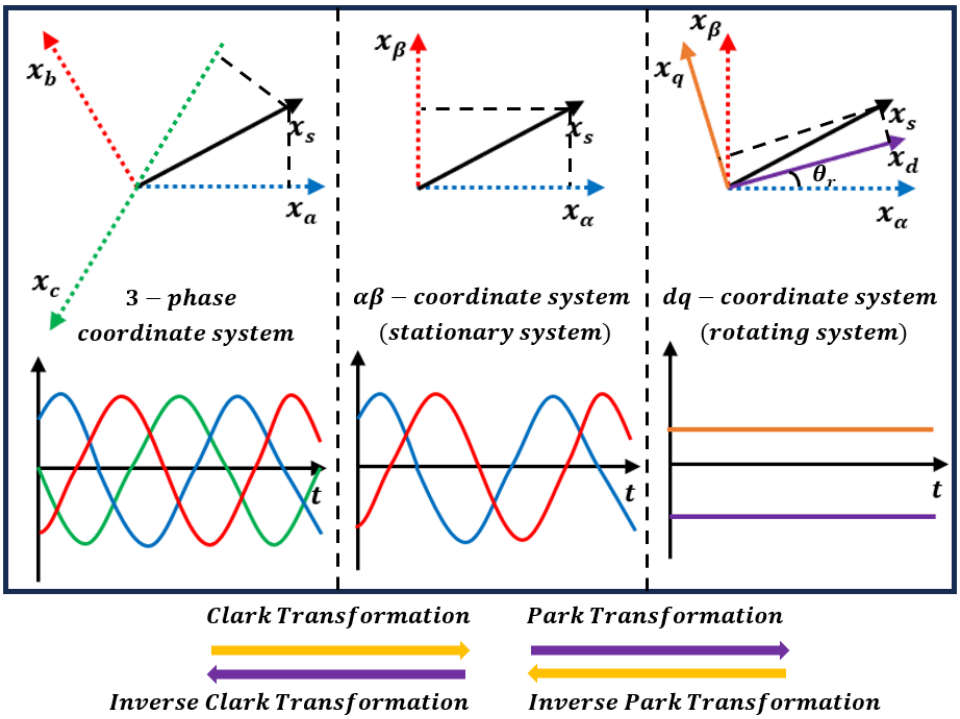

Figure 2.3: Transformation from stationary to rotating frame

The dq-coordinate system rotates at the same speed as the rotor speed, making it stationary with respect to the rotor. In this system, the d-axis aligns with the rotor flux direction, and resulting in x_d and x_q becoming two constant values within this reference frame.

These transformations simplify the analysis of various electrical quantities associated with PMSM. This study will apply an amplitude-invariant transformation with a constant factor of K=1, as defined in (2.1). The 3-phase quantities can also be computed from the dq-frame by applying the inverse of (2.1) and (2.2).

2.2.3 Dynamic Model and Electrical Properties

In the dq- coordinate system, the dynamic model of an IPMSM can be represented as a circuit equivalent model as displayed in Fig.2.4, which illustrates the distribution of stator voltages across the windings and flux linkages during a transient state.

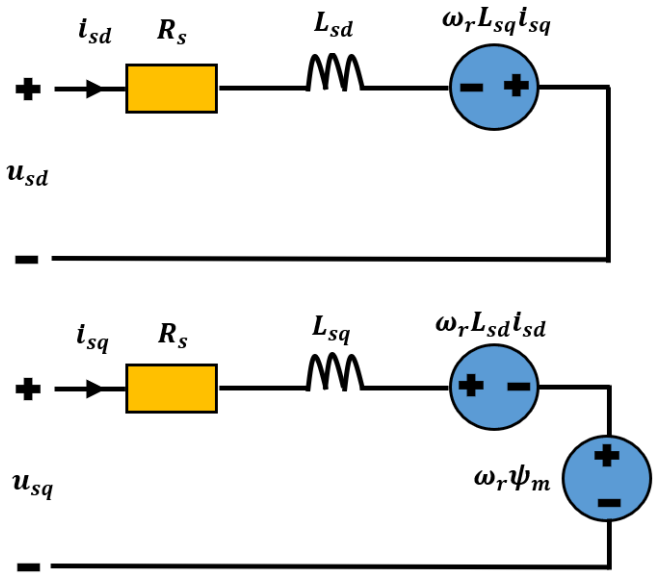

Figure 2.4: The dynamic model of IPMSM within dq-coordinate system

In this model, R_s is the stator phase winding resistance; L_{sd} and L_{sq} are stator inductance in dq-frame; ψ_m is the magnetic flux linkage; i_{sd} and i_{sq} are dq-stator current; u_{sd} and u_{sq} are dq-stator voltage; ω_r is the electrical speed of the rotor.

According to the dynamic model, the relationship between stator voltage and stator current can be expressed as

$$u_{sd} = R_s i_{sd} + L_{sd}\frac{di_{sd}}{dt} - \omega_r \psi_q \tag{2.3}$$

$$u_{sq} = R_s i_{sq} + L_{sd}\frac{di_{sq}}{dt} + \omega_r \psi_d \tag{2.4}$$

where ψ_d and ψ_q are stator flux linkage in dq-frame, which can be expressed as

$$\psi_d = L_{sd} i_{sd} + \psi_m \tag{2.5}$$

$$\psi_q = L_{sq} i_{sq} \tag{2.6}$$

In the steady state, (2.3) and (2.4) can be rewritten as

$$u_{sd} = R_s i_{sd} - \omega_r L_{sq} i_{sq} \tag{2.7}$$

$$u_{sq} = R_s i_{sq} + \omega_r L_{sd} i_{sd} + \omega_r \psi_m \tag{2.8}$$

For IPMSMs, the output electromagnetic torque[8] can be expressed as

$$T_e = T_{PM} + T_R = \frac{3n_p}{2}(\psi_m i_{sq} + (L_{sd} - L_{sq}) i_{sd} i_{sq}) \tag{2.9}$$

where n_p is the pole pair number of the machine and T_{PM} represents the alignment torque. Additionally, the reluctance torque T_R also emerges due to the inconsistent reluctance between the d- and q-directions. This occurs because the magnetic flux always prioritizes the path with the lowest magnetic resistance.

And from the mechanical dynamics perspective, the mechanical speed of rotor Ω_r is described by the following differential equation

$$\frac{d\Omega_r}{dt} = \frac{1}{J}\left(T_e - T_L - \frac{B}{n_p}\omega_r\right) \tag{2.10}$$

where T_L is the load torque applied on the shaft and B is the viscous damping constant, which represents the slope of the speed-dependent load torque. Moreover, J is the rotational inertia of the shaft.

The relationship between the electrical and mechanical speed of the rotor can be expressed as

$$\omega_r = n_p \Omega_r \tag{2.11}$$

The electromagnetic power generated by the electric machine at the shaft is given by

$$P_e = T_e \Omega_r = T_e \frac{\omega_r}{n_p} \tag{2.12}$$

And the fundamental frequency of the electric machine is calculated as

$$f_{el} = \frac{n_s n_p}{60} \tag{2.13}$$

where n_s represents the mechanical synchronous speed of the stator field, which is same as the mechanical speed of rotor n_r, can be expressed as

$$n_r = \frac{30}{\pi}\Omega_r \tag{2.14}$$

At the stator, the winding resistance per phase R_s is calculated as

$$R_s = \frac{\rho}{A_{strand}} \cdot \frac{N_{turn} \cdot q \cdot r \cdot n_p \cdot (l_a + l_w)}{N_{strand} \cdot N_{parallel}^2} \tag{2.15}$$

where ρ is the resistivity; A_{strand} is the cross-section area of a strand; q is the number of slots per pole per phase; r is the number of winding layers; N_{turn} is the number of turns per coil; N_{strand} is the number of strands per turn; $N_{parallel}$ is the number of parallel branches per phase; l_a and l_w represent the active length and end winding length per coil.

The end winding leakage inductance $L_{s,w}$ caused by the currents flowing through the end windings[9], can be calculated as

$$L_{s,w} = \frac{Q}{m} q \left(\frac{N_{turn}}{N_{parallel}} \right)^2 \mu_0 l_w \lambda_w \tag{2.16}$$

where Q, m and μ_0 represent the number of coils, number of phases and vacuum permeability, respectively. Additionally, the end winding length can be redefined as

$$\begin{cases} l_w = 2l_{ew} + W_{ew} \\ l_w \lambda_w = 2l_{ew}\lambda_{lew} + W_{ew}\lambda_{Wew} \end{cases} \tag{2.17}$$

where l_{ew} and W_{ew} signify the axial length and coil span of the end winding separately, as depicted in Fig.2.5. Furthermore, λ_{lew} and λ_{Wew} donate the associated permeance factor, which closely related to the winding structure.

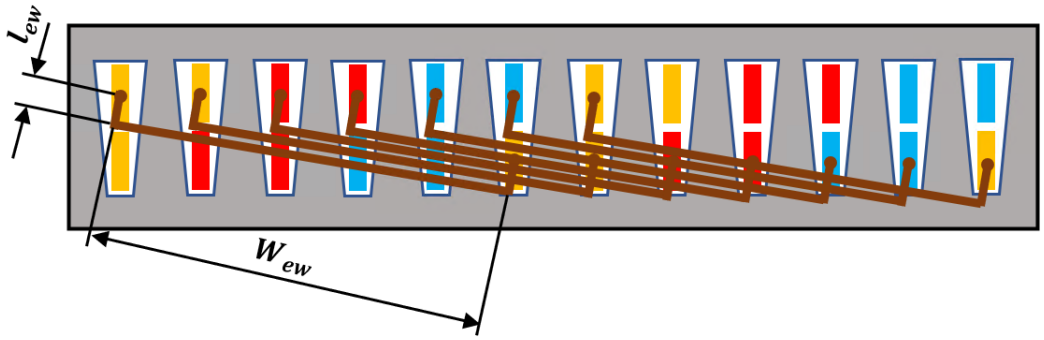

Figure 2.5: The arrangement of stator end windings

2.2.4 Power Losses and Energy Efficiency

In comparison to induction machines (IMs), PMSMs possess a rotor without current-carrying windings, which leads to reduced resistive losses and higher electrical energy efficiency[10]. When assessing the energy efficiency of a PMSM, the power losses primarily arise from copper losses in the windings, losses in the PMs, and iron losses in both the stator and rotor[11].

2.2.4.1 Copper Losses

Copper losses, also known as resistive losses or ohmic losses, stem from the resistance encountered by the current flowing through the conductor[12]. These losses lead to the generation of heat[13], and can be calculated as

$$P_{cu} = \frac{3}{2}(i_{sd}^2 + i_{sq}^2)R_s = \frac{3}{2}i_s^2 R_s \tag{2.18}$$

where i_s is the amplitude of the stator phase current.

2.2.4.2 Iron Losses

Based on Bertotti's theory, the iron losses are primarily composed of hysteresis loss $P_{fe,h}$, classical eddy current loss $P_{fe,c}$ and excess loss $P_{fe,e}$[14], which can be modeled as

$$P_{fe} = P_{fe,h} + P_{fe,c} + P_{fe,e} \tag{2.19}$$

The hysteresis loss and classical eddy current loss occur in both the stator and rotor lamination. Hysteresis loss arise due to the hysteresis behavior of electrical lamination. Classical eddy current loss, on the other hand, arise from fluctuates in flux linkage, inducing eddy currents within the core material[15]. Additionally, the excess loss mainly result from the distortion of motor's magnetic field[16].

The modified Steinmetz equations are used to describe $P_{fe,h}$, $P_{fe,c}$ and $P_{fe,e}$, which can be expressed by[17]

$$P_{fe,h} = k_h f B_m^2 \tag{2.20}$$

$$P_{fe,c} = k_c f^2 B_m^2 \tag{2.21}$$

$$P_{fe,e} = k_e f^{1.5} B_m^{1.5} \tag{2.22}$$

where f and B_m represent the frequency and the amplitude of magnetic flux density of the motor, and the parameter k_h, k_c and k_e are coefficients of hysteresis loss, classical eddy current loss and excess loss, respectively.

2.2.4.3 Losses in PMs

The eddy current loss induced in the PMs of synchronous AC machines have traditionally been ignored. This is because the harmonics in the current waveform and space harmonics in the winding distribution are typically small[18].

However, driven by the objective of enhancing performance in areas such as higher torque density and reduced torque ripple, the development of PMSMs towards fractional wound machines introduces time and space harmonics in the stator current[19]. These harmonics, rotating at different speeds from the rotor magnets, induce significant eddy currents in the PMs and lead to losses. Furthermore, during high-speed

or high-frequency operation, the eddy current loss in the PMs can contribute to increased temperatures, and pose a risk of irreversible demagnetization in the PMs of the PMSM[20]. Therefore, it is crucial to pay attention to this loss type.

The eddy current loss in PMs can be calculated as[21]

$$P_{mag,e} = \frac{1}{\sigma} \int J_e \cdot J_e^* dV \tag{2.23}$$

where σ and V represents the conductivity and volume of PM material, respectively. J_e is the eddy current density in PMs and J_e^* is the complex conjugate of J_e.

Although a study claims that significant hysteresis loss also exist in PMs[22]. While, the measurement result from Juha *et al.*[23] suggests that hysteresis loss in carefully designed machines play no important role in magnet materials when normally used in rotating electrical machines. As a result, hysteresis loss in PMs can be safely neglected in practice.

2.2.4.4 Energy Efficiency of PMSM

When neglecting stray losses and mechanical losses, the energy efficiency of a PMSM can be calculated as

$$\eta_p = \frac{P_{out}}{P_{in}} \cdot 100\% = \frac{P_e}{P_e + P_{cu} + P_{fe} + P_{mag,e}} \cdot 100\% \tag{2.24}$$

where P_{in} and P_{out} define the input and output power of a PMSM.

2.2.5 Current Vector Control Strategies

The main objective of the current vector control strategies is to obtain the desired reference torque by effectively controlling the stator current of the electric machine. In this thesis, two different control strategies of PMSM will be introduced: traditional maximum torque per ampere (MTPA) control strategy and loss minimization control strategy.

2.2.5.1 MTPA Control Strategy and Its Operating Range

The motor operation is constrained by two electrical limits, which includes stator current and voltage[24]. The current limit is determined by the maximum current magnitude of the motor ($i_{s,max}$), while the voltage limit is defined by the restrictions of the inverter. The current limit can be visualized as a circular boundary with a radius of $i_{s,max}$, and the voltage limit is represented by an elliptical shape whose size varies depending on the rotor operating speed, as illustrated in Fig.2.6.

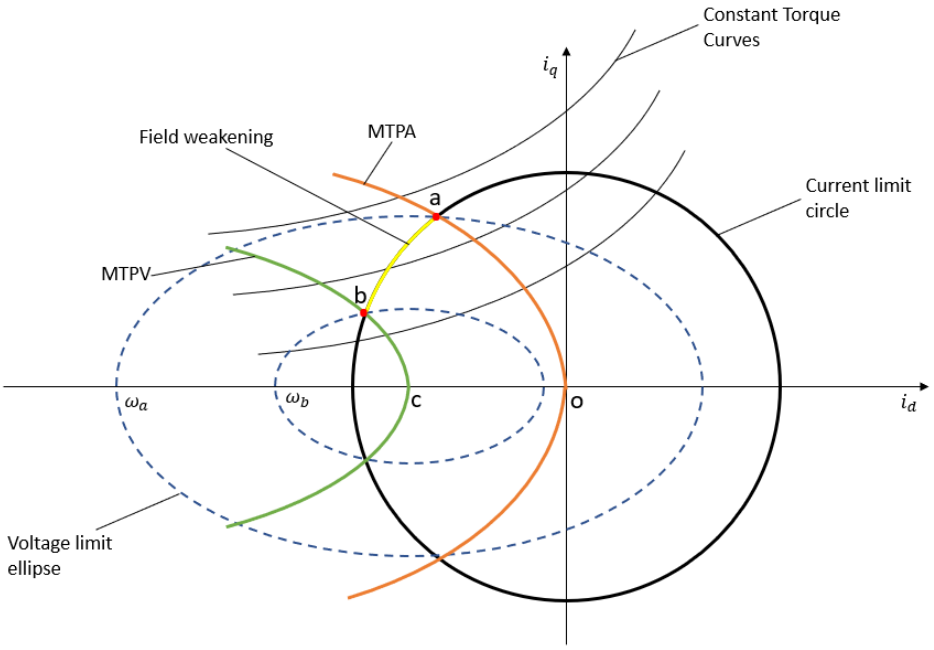

Figure 2.6: Limitations on stator current and voltage in a PMSM

The amplitude of stator currents can be represented in the *dq*-frame, which can be expressed as

$$i_{mag} = \sqrt{i_{sd}^2 + i_{sq}^2} \tag{2.25}$$

Additionally, i_{sd} and i_{sq} can also be written as

$$i_{sd} = i_{mag} cos\beta \tag{2.26}$$

$$i_{sq} = i_{mag} sin\beta \tag{2.27}$$

where β represents the stator current angle in radiance. The current limitation takes the form of a circle, as shown by the thick black line in Fig.2.6, which is defined as

$$\sqrt{i_{sd}^2 + i_{sq}^2} \leq i_{s,max} \tag{2.28}$$

By combining (2.26) and (2.27) with (2.9), the output electromagnetic torque of PMSM can be rewritten as

$$T_e = \frac{3n_p}{2}(\psi_m i_{mag} + (L_{sd} - L_{sq}) i_{mag}^2 sin\beta cos\beta) \tag{2.29}$$

It is obvious that the torque is dependent on β and i_{mag}. The maximum output torque can be determined by differentiating (2.29) with respect to β, as shown in the following expression

$$cos\beta = -\frac{\psi_m}{4(L_{sd} - L_{sq}) i_{mag}} - \sqrt{\frac{1}{2} + \left(\frac{\psi_m}{4(L_{sd} - L_{sq}) i_{mag}}\right)^2} \tag{2.30}$$

Based on (2.7) and (2.8), neglecting the effect of winding resistance R_s, the stator voltage in the dq-frame can be expressed as

$$u_{sd} = -\omega_r L_{sq} i_{sq} \tag{2.31}$$

$$u_{sq} = \omega_r (L_{sd} i_{sd} + \psi_m) \tag{2.32}$$

Therefore, by combining (2.31) and (2.32), the expression for the voltage-limited ellipse can be written as

$$\frac{u_s^2}{\omega_r^2} = (L_{sq} i_{sq})^2 + (L_{sd} i_{sd} + \psi_m)^2 \tag{2.33}$$

$$\Rightarrow \frac{\left(i_{sd} + \frac{\psi_m}{L_{sd}}\right)^2}{\frac{u_s^2}{\omega_r^2 L_{sd}^2}} + \frac{i_{sq}^2}{\frac{u_s^2}{\omega_r^2 L_{sd}^2}} = 1$$

The parameters defining the ellipse include the major radius (a), minor radius (b), and the intercept of the center on the x-axis (i_{d0}), which can be represented as

$$a = \frac{u_s}{\omega_r L_{sd}} \tag{2.34}$$

$$b = \frac{u_s}{\omega_r L_{sq}} \tag{2.35}$$

$$i_{d0} = -\frac{\psi_m}{L_{sd}} \tag{2.36}$$

This voltage-limited ellipse, as shown by the dotted line in Fig.2.6, is bounded by the maximum voltage, which is defined as

$$\sqrt{u_{sd}^2 + u_{sq}^2} \leq u_{s,max} \tag{2.37}$$

Fig.2.7 depicts the operating regions on a torque-speed graph, which can be divided into three distinct regions: constant torque, constant power, and high-speed. In each of these regions, different control methods are employed to effectively manage the motor's operation.

At the beginning of the operation, the motor torque increases from 0 to the rated torque. During this stage, the MTPA control strategy is employed, which aims to generate the highest possible torque for a given current[25]. This control algorithm selects the MTPA operating points as long as the currents and voltages remain within the limits of both the motor and the inverter. For every torque value up to the rated torque, the current vectors i_{sd} and i_{sq} are calculated to minimize the resultant i_{mag}. These points trace the trajectory $'oa'$ in Fig.2.6, the rated torque is achieved at the intersection point of the current limit circle and voltage-limited ellipse. The operating speed at which the PMSM accomplishes this process is known as the rated speed or base speed.

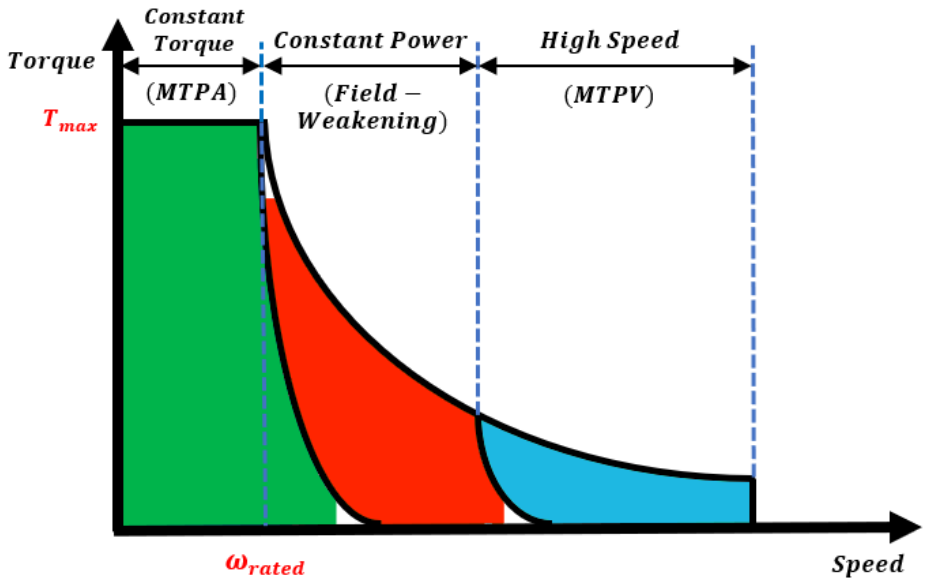

Figure 2.7: Operating range of a PMSM

Subsequently, an extended range of speeds is achieved through the implementation of field-weakening control[26]. As the machine reaches the rated speed, the back-electromotive force (EMF) reaches its highest limit and is effectively balanced with the maximum input voltage. The field-weakening involves reducing the flux generated by the PMs through the introduction of a negative d-current, which is also referred to as the demagnetizing current. Afterwards, the machine's ability to produce maximum torque is compromised, as observed in the constant power region illustrated in Fig.2.7 and the curve $'ab'$ in Fig.2.6.

Beyond the point $'b'$, the trajectory of maximum torque per voltage (MTPV) control, following the curve $'bc'$ in Fig.2.6, enable the motor to generate the maximum torque up to the point where the maximum speed is reached. As the speed rises, the voltage limit ellipse further contracts[27]. Theoretically, the maximum speed is limitless. However, when considering the presence of frictional components, the maximum speed is achieved when the frictional torque and motor torque are in equilibrium.

2.2.5.2 Loss Minimization Control Strategy

A significant limitation of the MTPA control strategy is that it cannot guarantee the stator current combination that simultaneously minimizes the total losses in PMSM. Hence, an alternative control strategy called loss minimization control is proposed to address this issue.

The objective of loss minimization control is to identify a series of current trajectories that consistently minimize motor losses under different operating speed. When the input current amplitude is constant, the current angle can be obtained by

$$\frac{d(P_{cu} + P_{fe})}{d\beta} = 0 \tag{2.38}$$

According to (2.18), the partial derivative of the copper loss can be expressed as

$$\frac{dP_{cu}}{d\beta} = \frac{d(3R_s i_{mag}^2(sin^2\beta + cos^2\beta))}{d\beta} = 6R_s i_{mag}^2(sin\beta cos\beta - sin\beta cos\beta) = 0 \quad (2.39)$$

This suggests that the influence of copper loss can be disregarded in this control strategy. Additionally, in comparison to the other two types of losses in the IPMSM, the eddy current loss in PMs can be ignored when the winding is excited with a 3-phase sinusoidal current by minimal ripples. Therefore, the current trajectory is solely determined by the iron loss model within the IPMSM.

2.3 Three-Phase Voltage Source Inverter Circuit

An inverter serve as a switching device that transforms the DC signals, typically obtained from a battery source, into an AC source with a desired voltage and frequency. This conversion is achieved through employing high-frequency switching of the semiconductors.

A simple half-bridge inverter circuit incorporates three converters to achieve a 2-level voltage source inverter (VSI) configuration[28], as illustrated in Fig.2.8. This type of inverter is frequently employed in automotive applications due to its compact design, lightweight structure, and excellent performance.

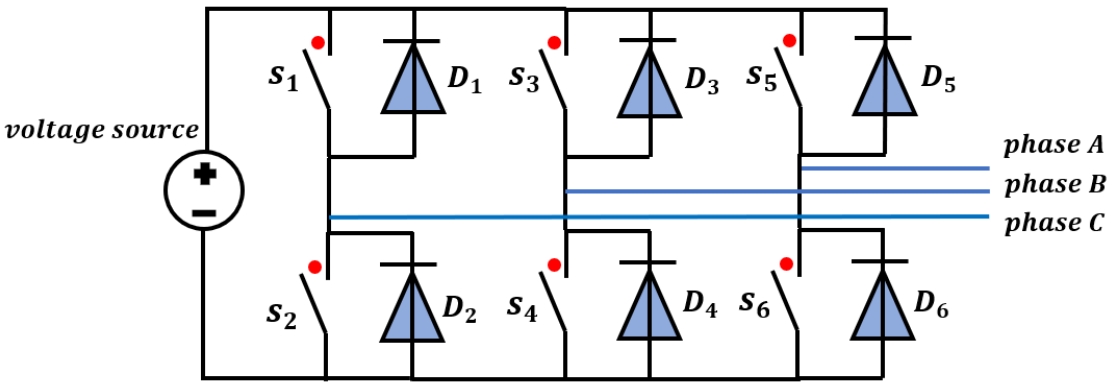

Figure 2.8: A simple 2-level VSI circuit

This inverter circuit consists 6 switching devices, labeled $S1$-$S6$ (typically MOSFETs or IGBTs), paired with 6 anti-parallel diodes, denoted as $D1$-$D6$. By selecting a particular switching arrangement for these 6 semiconductors, a 3-phase sinusoidal current is generated, with each phase shifted by 120°. This allows the electric machine to generate controllable speed and torque by modifying the frequency and amplitude of the sinusoidal current, respectively.

2.3.1 Power electronic components

The most commonly used power electronic components utilized in a voltage-source inverter circuit are MOSFETs and IGBTs, as shown by their symbols in Fig.2.9.

Both of them have their own strengths and shortages. However, with the rapid development of power SiC MOSFETs, they have shown a superior advantage in motor drive application[29]. Therefore, this work specifically concentrates on SiC MOSFETs due to its remarkable ability to operate at higher voltage levels, frequencies, and junction temperatures[30].

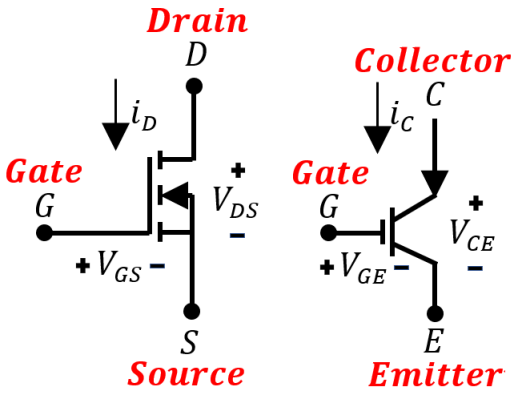

Figure 2.9: Symbol of MOSFETs (left) and IGBTs (right)

2.3.1.1 MOSFET and diode

A MOSFET is a type of voltage-controlled field-effect transistor device, where the voltage between the gate and source, V_{GS}, controls the current from drain to source. The excellent characteristics of a SiC MOSFET, including its high gate input impedance and rapid switching speed, makes it ideal for motor drive applications[31].

Moreover, a diode is a type of semiconductor that conducts current in only one direction while blocking its flow in the opposite direction. As the motor load is inductive, a simple diode is connected in an anti-parallel arrangement with the MOSFETs. This aims to dissipate the back-EMF generated by the motor when the MOSFET is in the "OFF" state.

2.3.2 Inverter Control Method

Sinusoidal Pulse Width Modulation (SPWM) is a widely used method for controlling inverters. With SPWM, the inverter switches are controlled based on a comparison between a high-frequency triangular wave (termed carrier wave) and a sinusoidal reference signal (as illustrated in Fig.2.10) with a desired frequency and amplitude.

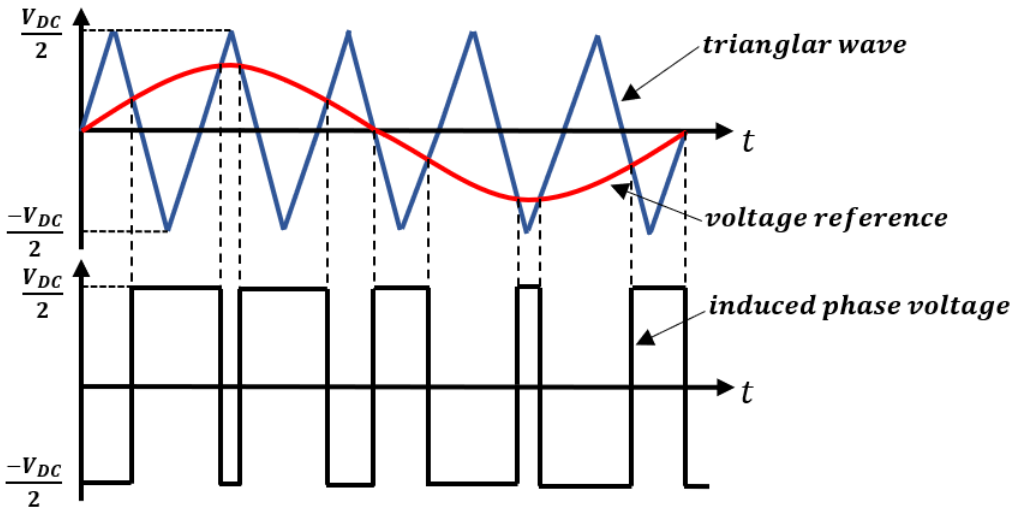

Figure 2.10: The process of SPWM control strategy

As depicted in the figure, the amplitude of the triangular wave equals half of the DC-link voltage. During the time period when the reference phase voltage exceeds the triangular wave, the upper device switch is turned on while the lower device switch is turned off, directing the I_{DS} flows through the upper device. Otherwise, the lower device switch is turned on and the I_{DS} flows through the lower device. Therefore, a sequence of PWM pulse waveforms with equal width but different intervals are generated, which is used as a reference for controlling the switching state of the inverter.

The intersection point of the sine wave with the triangle wave determines the timing of the state transitions. The frequency of the triangular wave far exceeds that of the reference wave, and the ratio between them is defined as the frequency modulation index (M_f)[32]. Additionally, the ratio between the amplitude of the reference wave and the triangular wave is known as the amplitude modulation index (M_a).

2.3.3 Harmonics

In the design of electric machines or any other electric appliances, an ideal sinusoidal power supply is assumed, making design calculations simpler. However, this is impossible in practical applications. A distorted wave consists of a fundamental frequency along with various sinusoidal waves (harmonic components) with frequencies that are an integral multiple of the fundamental frequency [33].

In order to analyze this distorted waveform, Fourier analysis is used to convert the signal represented in the time domain to the frequency domain and vice versa. The signal can be decomposed using Fourier transformation which is given as

$$f(t) = A_o + \sum_{h=1}^{\infty} [A_h cos(h\omega_o t) + B_h sin(h\omega_o t)] \tag{2.40a}$$

$$= A_o + \sum_{h=1}^{\infty} C_h sin(h\omega_o t + \psi_h) \tag{2.40b}$$

where, A_o, A_h, and B_h are Fourier series coefficients given as

$$\begin{cases} A_o = \frac{1}{T}\int_0^T f(t)dt \\ A_h = \frac{2}{T}\int_0^T f(t)cos(h\omega_o t)dt \\ B_h = \frac{2}{T}\int_0^T f(t)sin(h\omega_o t)dt \\ C_h = \sqrt{A_h^2 + B_h^2} \\ \psi_h = tan^{-1}\left(\frac{A_h}{B_h}\right) \end{cases} \tag{2.41}$$

where $f(t)$ is a periodic function of frequency f_o , ω_o is its angular frequency, and T is the time period. $C_h{\cdot}sin(h\omega_o t + \psi_h)$ is the h^{th} harmonic with an amplitude C_h and phase ψ_h.

2.3.4 Slew rate

In the application of power electronics, the term "slew rate" can be considered as the rate of change of voltage or current over time. It is generally expressed in (2.42) with the units of $V/\mu s$ or $A/\mu s$. Additionally, Fig.2.11 depicts the slew rate of a square wave.

$$S = \frac{\delta V}{\delta t} \tag{2.42}$$

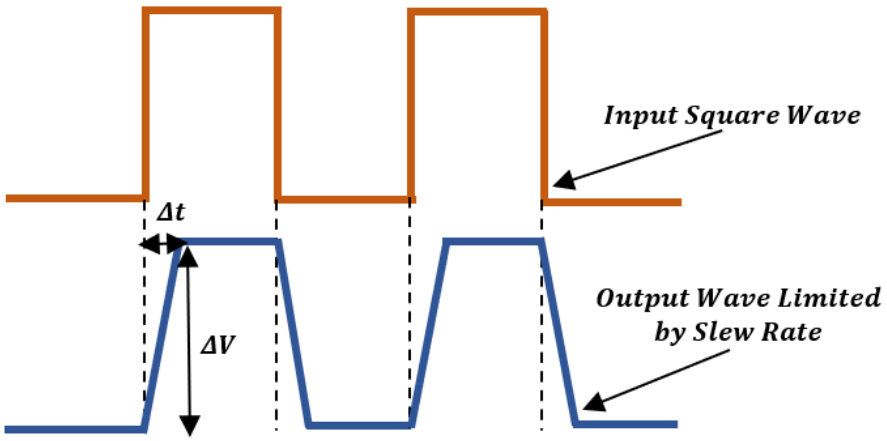

Figure 2.11: Slew rate of a square wave signal

2.3.5 Power Losses in One Phase Leg of the Inverter

In each phase leg, the power losses are influenced by the current waveform, which consists of the fundamental value and current ripple. The fundamental value depends on the type of load, while the current ripple is determined by the switching frequency. The main overall losses P_l within a 3-phase VSI are attributed to conduction losses and switching losses while blocking losses are neglected[34], which can be expressed as

$$P_l = P_c + P_{sw} + P_b \approx P_c + P_{sw} \tag{2.43}$$

where P_c, P_{sw}, and P_b represent conduction losses, switching losses, and blocking losses, respectively.

2.3.5.1 Conduction Losses

Considering the forward voltage drop for power SiC MOSFETs as zero[35], the corresponding drain-source voltage drop U_{DS} can be estimated by

$$U_{DS}(I_{DS}) = R_{DSon}(I_{DS}) \cdot I_{DS} \tag{2.44}$$

where R_{DSon} and I_{DS} represent the drain-source on-state resistance and drain-source current of SiC MOSFETs respectively, and it is necessary to highlight that R_{DSon} varies with I_{DS} across diverse virtual junction temperatures.

Therefore, the instantaneous and average conduction loss in a SiC MOSFET is given by[36]

$$\begin{cases} P_{cM}(t) = U_{DS}(t) \cdot I_{DS}(t) = R_{DSon} \cdot I_{DS}^2(t) \\ P_{cM,avg} = \frac{1}{T_{sw}} \int_0^{T_{sw}} P_{cM}(t)dt \end{cases} \tag{2.45}$$

$$\Rightarrow P_{cM,avg} = R_{DSon} \cdot I_{Drms}^2$$

The switching cycle T_{sw} is taken into account when calculating the average value, and I_{Drms} represents the root mean square (RMS) value of the MOSFET on-state current.

The instantaneous conduction loss of the anti-parallel diode can be estimated using the voltage across the diode U_D, which is

$$U_D = U_{D0} + R_D \cdot I_F \tag{2.46}$$

where U_{D0} is the diode on-state zero-current voltage and R_D is the diode on-state resistance. By applying a current I_F, through the diode, the instantaneous and average conduction loss in the diode can be expressed as[36]

$$\begin{cases} P_{cD}(t) = U_D(t) \cdot I_F(t) = U_{D0} \cdot I_F(t) + R_D \cdot I_F^2(t) \\ P_{cD,avg} = \frac{1}{T_{sw}} \int_0^{T_{sw}} P_{cD}(t)dt \end{cases} \tag{2.47}$$

$$\Rightarrow P_{cD,avg} = U_{D0} \cdot I_{Fav} + R_D \cdot I_{Frms}^2$$

where I_{Fav} and I_{Frms} represent the average and RMS value of the diode current, respectively.

In a three-phase VSI, the conduction loss for power SiC MOSFETs and body diodes can be modeled according to the peak current value I_o, power factor $\cos(\psi)$, and amplitude modulation index M_a, which can be expressed as

$$P_{cM} = R_{DSon} \cdot I_{Drms}^2 = R_{DSon} \cdot I_o^2 \cdot \left(\frac{1}{8} + \frac{M_a cos(\psi)}{3\pi} \right) \tag{2.48}$$

$$P_{cD} = U_{D0} \cdot I_{Fav} + R_D \cdot I_{Frms}^2 = U_{D0} \cdot I_o \cdot \left(\frac{1}{2\pi} - \frac{M_a cos(\psi)}{8} \right) + R_D \cdot I_o^2 \cdot \left(\frac{1}{8} - \frac{M_a cos(\psi)}{3\pi} \right) \tag{2.49}$$

The phase angle ψ and M_a can be given as

$$\psi = arctan(\frac{u_{sq}}{u_{sd}}) - arctan(\frac{i_{sq}}{i_{sd}}) \tag{2.50}$$

$$M_a = \frac{2|u_s|}{U_{DC}} \tag{2.51}$$

where the U_{DC} represents the DC-link voltage in the 3-phase inverter circuit.

2.3.5.2 Switching Losses

The modeling circuit for analyzing transient switching losses is shown in Fig.2.12[36]. It comprises a single-quadrant chopper and a highly inductive load. The internal diode of the power MOSFET is utilized as a freewheeling diode. This configuration is commonly employed in power electronic converters, which typically consist of one or more MOSFET-based half bridges in 3-phase AC motor drives.

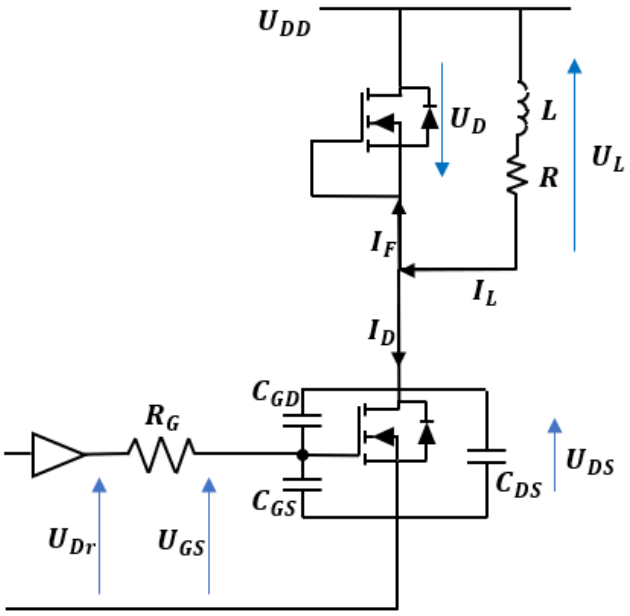

Figure 2.12: MOSFET transient modeling circuit with an inductive load

The U_{Dr} indicates the drive output voltage. And the component C_{GD}, C_{GS}, and C_{DS} are internal capacitances of the MOSFET, which correspond to the input capacitance C_{iss}, reverse transfer capacitance C_{rss}, and output capacitance C_{oss} by the following relations

$$\begin{cases} C_{GD} = C_{rss} \\ C_{GS} = C_{iss} - C_{rss} \\ C_{DS} = C_{oss} - C_{rss} \end{cases} \tag{2.52}$$

The switch-on transient is simulated in Fig.2.13. At the beginning, the load current flows through the diode, the drive circuit changes the state from $0V$ to U_{Dr}, and the gate-source voltage U_{GS} starts to rise from $0V$. Meanwhile, the capacitance C_{GD} and C_{GS} begin to charge through the gate resistor R_G.

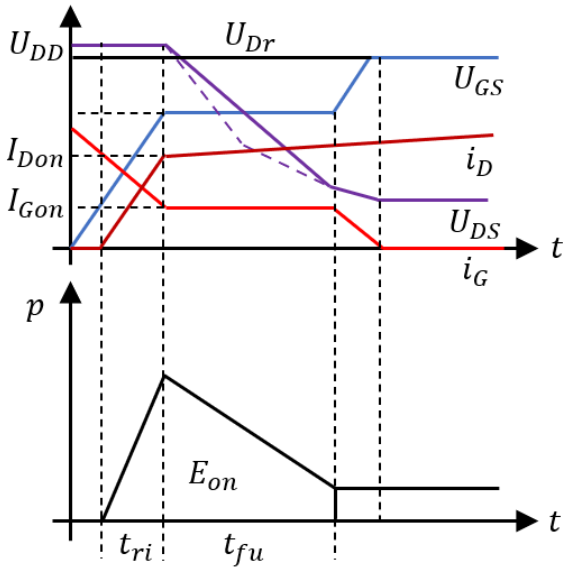

Figure 2.13: Switch-on transient waveforms

The drain current I_D remains at $0A$ until U_{GS} reaches its threshold $U_{GS,th}$, and afterwards, the load current I_L starts to be taken over by I_D. During the current-rise time period t_{ri}, the drain-source voltage U_{DS} remains constant at U_{DD}. Subsequently, it begins to decline to the on-state value by the end of the voltage-fall time period t_{fu} to facilitate the switching off of the diode. However, at the same time, this action also induces a reverse-recovery current, which greatly affects the power losses in power MOSFETs.

Therefore, the turn-on energy losses in a SiC MOSFET can be divided into two components: the switch-on energy and the switch-on energy caused by the reverse recovery of the diode. These energy losses can be represented by

$$E_{onM} = \int_0^{t_{ri}+t_{fu}} U_{DS}(t) \cdot I_D(t)dt = U_{DD} \cdot I_{Don} \cdot \frac{t_{ri} + t_{fu}}{2} + Q_{rr} \cdot U_{DD} \tag{2.53}$$

where Q_{rr} represents the reverse-recovery charge. And the turn-on energy losses in a body diode can be expressed as

$$E_{onD} = \int_0^{t_{ri}+t_{fu}} U_D(t) \cdot I_F(t)dt = \frac{1}{4} \cdot Q_{rr} \cdot U_{Dr} \tag{2.54}$$

The switch-off transient starts with the decrease of the gate-source voltage U_{GS}, as shown in Fig.2.14.

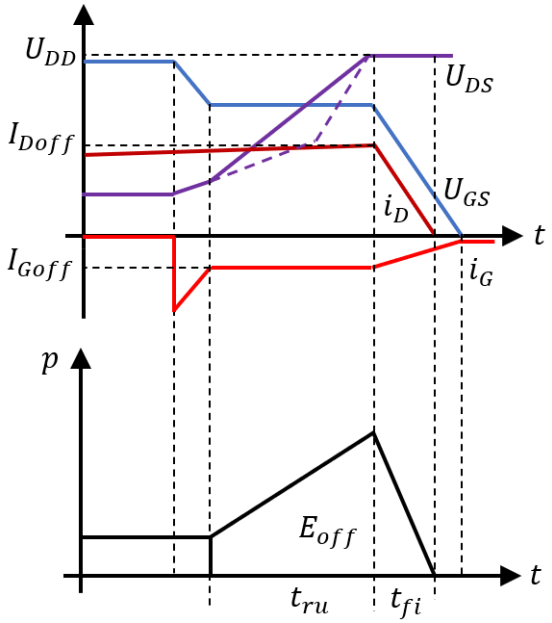

Figure 2.14: Switch-off transient waveforms

At this point, the internal capacitance C_{GD} and C_{GS} start discharging through R_G and the drain current I_D remains nearly constant. Afterwards, U_{GS} keeps unchanged and all currents are drawn from the capacitance C_{GD} during the voltage-rise time period t_{ru}.

At the start of the current-fall period t_{fi}, the drain-source voltage U_{DS} reaches the DC voltage, resulting in the diode being switched on. Finally, I_D drops to $0A$ while U_{GS} descends to the threshold voltage $U_{GS(th)}$ and further reaches $0V$. This indicates that the MOSFET is completely switched off[37].

Compared to the switch-on process, the most significant difference in the switch-off process is the absence of reverse recovery. Therefore, the turn-off energy loss in one SiC MOSFET consists of only one part, which is expressed as

$$E_{offM} = \int_0^{t_{ru}+t_{fi}} U_{DS}(t) \cdot I_D(t) dt = U_{DD} \cdot I_{Doff} \cdot \frac{t_{ru} + t_{fi}}{2} \tag{2.55}$$

While the turn-on loss in one diode can be considered negligible, which can be signified as

$$E_{onD} \approx 0 \tag{2.56}$$

The switching losses in one SiC MOSFET and diode can be modeled as the product of switching energies and switching frequency[36]

$$P_{swM} = (E_{onM} + E_{offM}) \cdot f_{sw} \tag{2.57}$$

$$P_{swD} = E_{offD} \cdot f_{sw} \tag{2.58}$$

In the three-phase AC motor drive system, the switching losses for power SiC MOSFETs and body diodes can be modeled as

$$P_{swMon} = \frac{f_{el} \cdot I_o \cdot U_{DC} \cdot E_{onM}}{2 \cdot U_{ref} \cdot I_{ref}} \left(\frac{2p}{\pi} - \frac{M_a \pi}{4}\left(\frac{\pi}{2p} cos\psi + sin\psi\right)\right) \tag{2.59}$$

$$P_{swMoff} = \frac{f_{el} \cdot I_o \cdot U_{DC} \cdot E_{offM}}{2 \cdot U_{ref} \cdot I_{ref}} \left(\frac{2p}{\pi} - \frac{M_a \pi}{4}\left(\frac{\pi}{2p} cos\psi - sin\psi\right)\right) \tag{2.60}$$

$$P_{swD} = \frac{f_{el} \cdot I_o \cdot U_{DC} \cdot E_{rr}}{2 \cdot U_{ref} \cdot I_{ref}} \left(\frac{2p}{\pi} - \frac{M_a \pi}{4}\left(\frac{\pi}{2p} cos\psi + sin\psi\right)\right) \tag{2.61}$$

where U_{ref} and I_{ref} represent the testing drain-source voltage and current used to determine the switching energy. And the parameter p represents the frequency ratio between the switching frequency and fundamental frequency ($p = f_{sw}/f_{el}$).

2.3.6 Thermal Networks of Inverters

According to statistics, temperature rise is the main reason for failure in semiconductor devices, accounting for over 50%[38]. Therefore, accurate junction temperature estimation is important for the reliability of SiC MOSFETs[39]. Meanwhile, accurate temperature estimation can promote more precise calculation of electrical parameters, thereby improving the analysis of power losses.

As illustrated in Fig.2.15, heat conduction in power SiC MOSFETs can be mainly divided into three processes: from the virtual junction to the case, from the case to the heat sink, and from the heat sink to the ambient conditions.

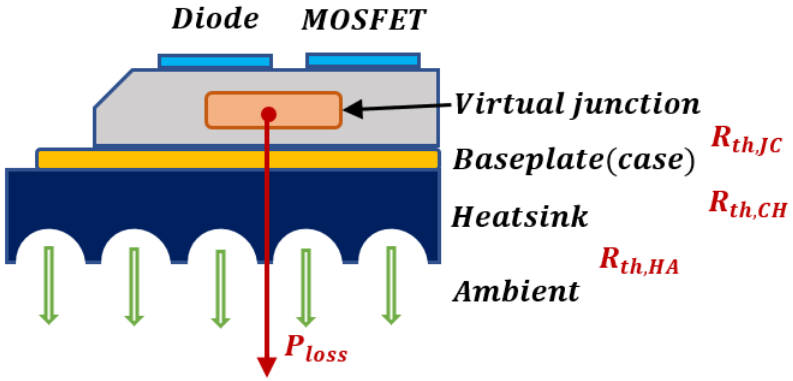

Figure 2.15: Heat power conduction in MOSFETs

The thermal resistances in these processes are denoted as $R_{th,JC}$, $R_{th,CH}$, and $R_{th,HA}$ respectively, which can be expressed by

$$R_{th,JC} = \frac{T_J - T_C}{P_l} \tag{2.62}$$

$$R_{th,CH} = \frac{T_C - T_H}{P_l} \tag{2.63}$$

$$R_{th,HA} = \frac{T_H - T_A}{P_l} \tag{2.64}$$

where T_J to T_A signifies the temperature values from the junction to ambient condition. If considering P_l as the current and T as the voltage in a DC circuit, the junction temperature can be modeled as

$$T_J = T_A + (R_{th,JC} + R_{th,CH} + R_{th,HA})P_l \tag{2.65}$$

Two commonly used thermal models, the partial fraction circuit model (Foster model) and the continued fraction circuit model (Cauer model), provide effective interpretations of this thermal process. These models are illustrated in Fig.2.16[40].

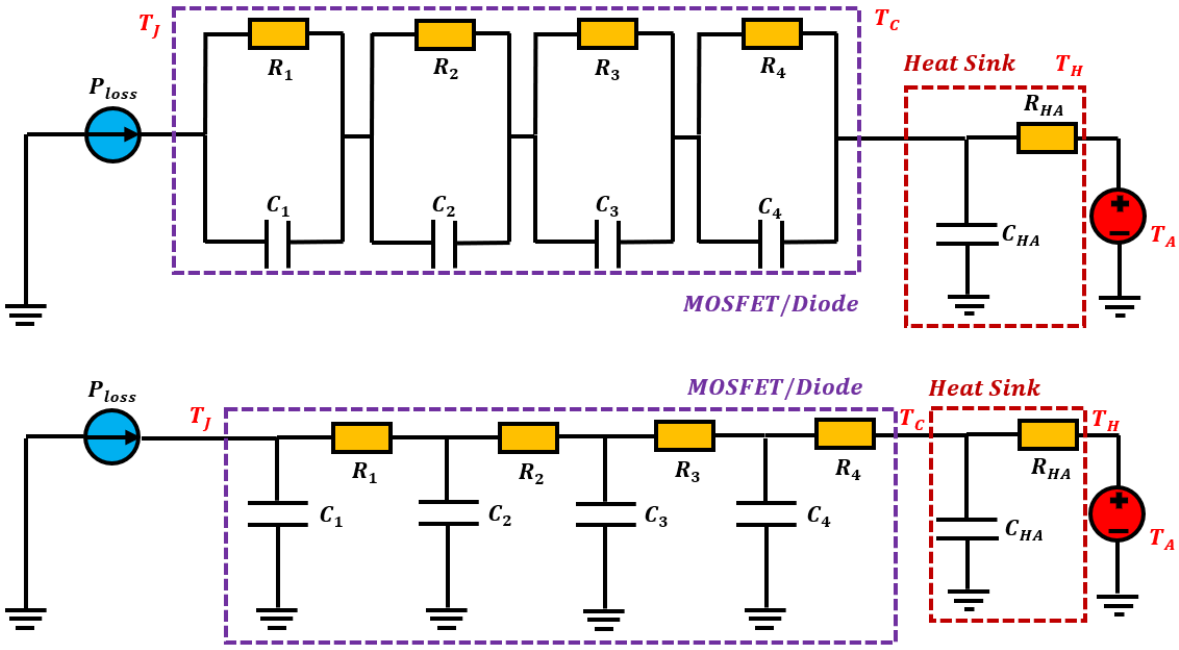

Figure 2.16: Foster (top) and Cauer (bottom) model circuit

The Cauer model represents the physical structure of a semiconductor device by incorporating thermal capacitances with thermal resistances. This model can be built when the material characteristics of the individual layers are determined. Meanwhile, the individual RC elements in the model can be assigned to the corresponding layers of the module, enabling access to the internal temperatures of the layer sequence through the network nodes.

On the other hand, the Foster model does not directly represent the layer sequence with its individual RC elements, and the network nodes within this model do not posses any physical significance. This simplified representation is often employed in

the datasheets, as the coefficients can be obtained from a measured cooling curve of the module. Additionally, this model is particularly useful for analytical calculations.

2.3.7 Parallel Operation of Inverters

The requirement for switching very high currents, which often exceed the current capability of a single-power device, is continuously increasing in the modern electric vehicle industry. In micro-hybrid applications, it may even be necessary to switch currents higher than $1000A$. Therefore, it is typically essential to design a parallel configuration of multiple power SiC MOSFETs to reach the desired current rating and increased capability[41].

Theoretically, the MOSFETs connected in parallel, as illustrated in Fig.2.17, should share the overall current equally, resulting in the same power loss and temperature in each branch. However, because of the variation in parameters among MOSFET dies on a wafer, their actual values can be distributed in anywhere within the range demonstrated in datasheet. As a result, the current and power sharing among the parallel MOSFETs may not be perfectly balanced, and their junction temperatures are likely dissimilar[42].

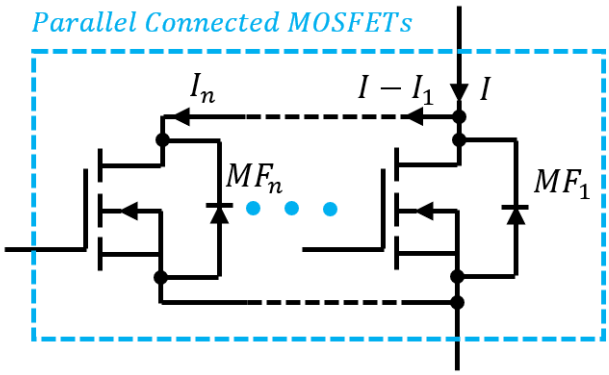

Figure 2.17: Parallel connection of power SiC MOSFETs

The phenomenon is significantly influenced by two key parameters: the drain-source on-state resistance R_{DSon} and the gate threshold voltage $U_{GS,th}$. These parameters contribute distinct impacts to both static and dynamic current sharing.

In Fig.2.17, the current distribution among the branches depends on the value of R_{DSon} in each MOSFET. The worst-case scenario occurs when one MOSFET has the lowest $R_{DSon,min}$ within the reasonable range, resulting in the highest current I_{max}, while the other MOSFETs have the highest $R_{DSon,max}$, and thus the lowest current I_{min}. It is reasonable to assume that the minimal and maximal values of R_{DSon} are symmetrically distributed around the typical value[41]. Therefore, the $R_{DSon,min}$ can be expressed as

$$R_{DSon,min} = R_{DSon,max} - 2(R_{DSon,max} - R_{DSon,typ}) \tag{2.66}$$

The MOSFET with the lowest R_{DSon} value will carry the largest portion of the total current, with the maximal value given by

$$I_{max} = \frac{\frac{R_{DSon,max}}{n-1}}{R_{DSon,min} + \frac{R_{DSon,max}}{n-1}} I \tag{2.67}$$

where n represents the number of branches, and the highest power dissipation occurs in this branch, as determined by (2.45).

During the instantaneous turn-on/off state of a MOSFET, $U_{GS,th}$ becomes the most significant parameter influencing equal power sharing. In the beginning, the MOSFET with the lowest $U_{GS,th}$ will begin conducting channel current first, resulting in higher power dissipation and heat generation. As a result, its $U_{GS,th}$ will further decrease, exacerbating the power imbalance. This leads to the hottest MOSFET occupying a larger proportion of the power. Unfortunately, this process is unsustainable and may result in MOSFET failures unless the generated power is effectively limited[42].

2.4 PMSM Control Techniques

In order to obtain the 3-phase reference voltage as input for the inverter circuit and ensure the proper operation of the 3-phase inverter, the import of an appropriate machine controller is indispensable.

During machine control, the field-oriented control (FOC) strategy is widely recognized as one of the most suitable methods for achieving smooth rotation, quick acceleration, and deceleration in a PMSM drive[43]. The objective of FOC is to precisely control the space vector of magnetic flux, current, and voltage of the electric machine in order to achieve the desired target of operating speed[44].

The proportional-integral (PI) controller is generally used as a speed and torque controller in order to eliminate the steady-state error in FOC PMSM drives[45, 46]. In this Section, the mathematical model and parameter setting of the current and speed controller will be introduced specifically.

2.4.1 Process Model of PMSM

As shown in Section 2.2, the 3-phase PMSM can be converted into a dynamic model within the *dq*-coordinate system, based on (2.3) and (2.4), the expression for the stator current can be modeled as

$$L_{sd}\frac{di_{sd}}{dt} = u_{sd} - R_s i_{sd} + \omega_r L_{sq} i_{sq} \tag{2.68}$$

$$L_{sq}\frac{di_{sq}}{dt} = u_{sq} - R_s i_{sq} - \omega_r L_{sd} i_{sd} - \omega_r \psi_m \tag{2.69}$$

These equations indicate how two first-order systems interact with each other and how the stator current is affected by the stator voltage, which can be considered as internal electric properties of the PMSM and remain independent of external control systems.

By applying the Laplace transform, (2.68) and (2.69) can be rewritten as

$$i_{sd} = \frac{1}{L_{sd}s + R_s}(u_{sd} + \omega_r L_{sq} i_{sq}) \tag{2.70}$$

$$i_{sq} = \frac{1}{L_{sq}s + R_s}(u_{sq} - \omega_r L_{sd} i_{sd} - \omega_r \psi_m) \tag{2.71}$$

Therefore, the transfer function inside the PMSM can be given as

$$G_{cd}(s) = \frac{1}{L_{sd}s + R_s} \tag{2.72}$$

$$G_{cq}(s) = \frac{1}{L_{sq}s + R_s} \tag{2.73}$$

The whole process model of IPMSM can be modeled as Fig.2.18, with the cross-coupling $\omega_r L_s i_s$ and back-EMF E shown in the blue and red block, respectively.

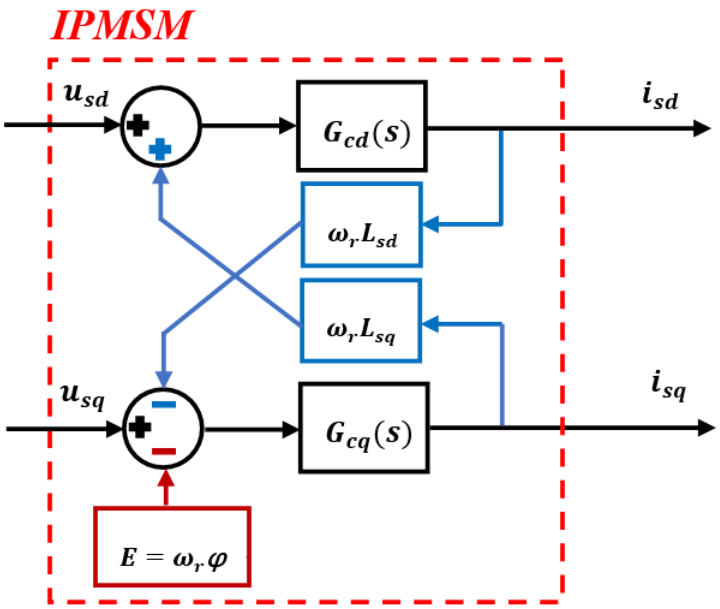

Figure 2.18: Process model of IPMSM

2.4.2 Current Controller

Based on the process model of PMSM, a closed-loop control system can be built around the electric dynamics, as shown in Fig.2.19. The output current i_s is measured and compared with the reference current i_{ref}, and the error e between them

can be act as the input of the current controller $F_c(s)$.

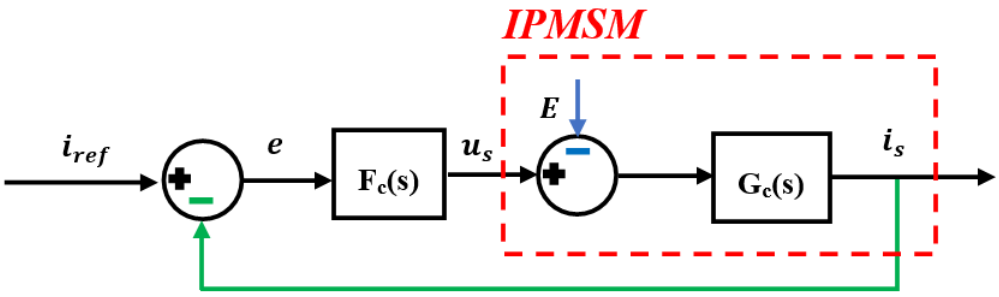

Figure 2.19: Closed-loop control system of IPMSM

With the bandwidth α_c of closed-loop system, the transfer function of the closed-loop current control system can be expressed as

$$G_{ce}(s) = \frac{i_s}{i_{ref}} = \frac{F_c(s)G_c(s)}{1 + F_c(s)G_c(s)} = \frac{\alpha_c}{s + \alpha_c} = \frac{\frac{\alpha_c}{s}}{1 + \frac{\alpha_c}{s}} \tag{2.74}$$

2.4.2.1 Active Resistance

Sometimes, the load disturbance caused by back-EMF can greatly affect the accuracy of the controller. If the load disturbance E and the current error e is considered as the input and output of system, the transfer function of current controller can be expressed as

$$G_{Ee}(s) = \frac{e}{E} = \frac{G_c(s)}{1 + F_c(s)G_c(s)} = \frac{s}{s + \alpha_c}G_c(s) \tag{2.75}$$

Based on (2.72) and (2.73), (2.75) can be rewritten as

$$G_{Ee}(s) = \frac{s}{s + \alpha_c}\frac{1}{L_s s + R_s} \tag{2.76}$$

Usually, the load disturbance E is time-varying. Therefore, the steady-state gain from dE/dt to the controller error is

$$[\frac{G_{Ee}(s)}{s}]_{s=0} = \frac{1}{\alpha_e R_s} \tag{2.77}$$

Due to the electrical dynamics are much faster than the mechanical dynamics, dE/dt can be regarded as constant and the control error can be calculated by

$$e = \frac{1}{\alpha_e R_s}\frac{dE}{dt} = \frac{\psi}{\alpha_e R_s}\frac{d\omega_r}{dt} \tag{2.78}$$

By replacing the differential part of electric speed with dynamics according to (2.10), (2.78) can be further written as

$$e = \frac{n_p \psi}{\alpha_e R_s J}(T_e - T_{L,extra} - \frac{B}{n_p}\omega_r) \tag{2.79}$$

Indeed, the current error e will decrease as the winding resistance R_s increases. However, based on (2.18), increasing the winding resistance of the machine can leads to an increase in copper loss. To achieve the desired effect without increasing copper loss, an active resistance R_a can be added to the closed-loop system.

2.4.2.2 Decoupler of Cross-Coupling and Feed-Forward of Back-emf

Next, the cross-coupling and back-emf of IPMSM should be compensated in current controller system. This can be implemented by introducing two decouplers $j\omega_r\hat{L}_s$ and a feed-forward part $\omega_r\hat{\psi}_m$. Here $\hat{L}_s$ represents the estimated inductance and $\hat{\psi}_m$ represents the estimated magnetic flux linkage. The implementation of these decouplers and the feed-forward component is shown in Fig.2.20.

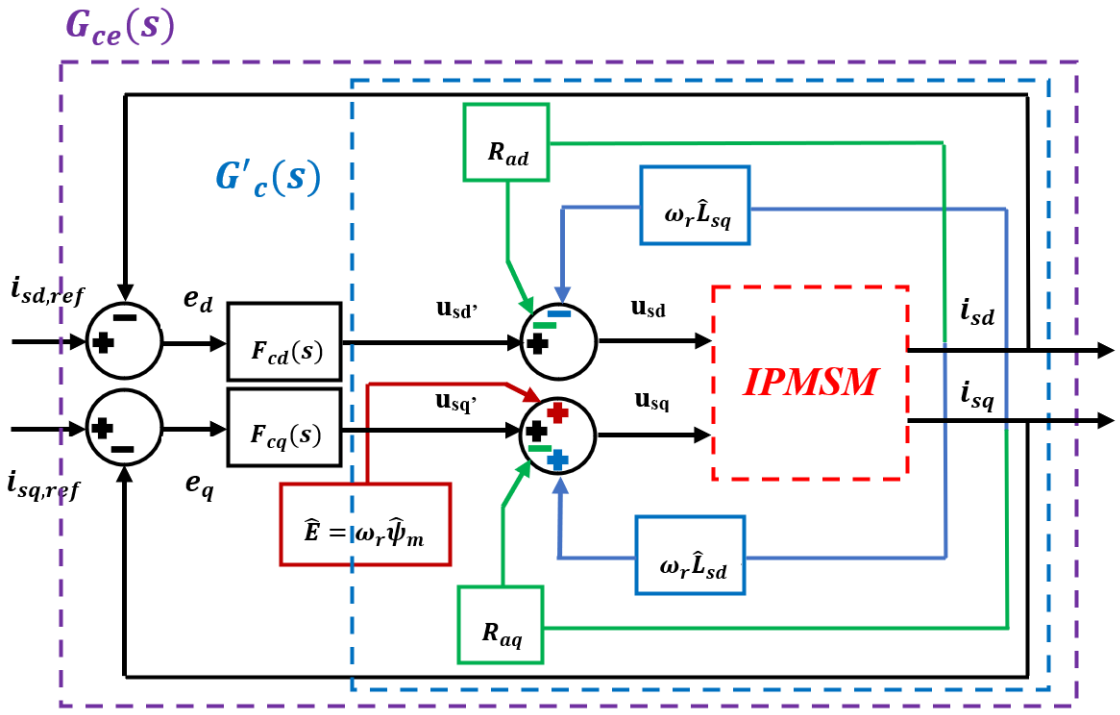

Figure 2.20: Closed-loop current control system with decoupler, feed-forward and active resistance

The expression of the input voltage can be updated as

$$u'_{sd} = u_{sd} + \omega_r\hat{L_{sq}}i_{sq} + R_{ad}i_{sd} = (R_s + R_{ad} + L_{sd}s)i_{sd} \tag{2.80}$$

$$u'_{sq} = u_{sq} - \omega_r\hat{L_{sd}}i_{sd} + R_{aq}i_{sq} - \omega_r\hat{\psi}_m = (R_s + R_{aq} + L_{sq}s)i_{sq} \tag{2.81}$$

Therefore, the transfer function from u'_s to i_s is

$$G'_c(s) = \frac{i_s}{u'_s} = \frac{1}{L_s s + R_s + R_a} \tag{2.82}$$

2.4.2.3 PI Controller

Since the first-order electric dynamics, the mathematical representation of a PI controller in the complex domain can be modeled as[47]

$$F_c(s) = k_p + \frac{k_i}{s} \tag{2.83}$$

Similar with (2.74), the transfer function $F_c(s)$ can be rewritten as

$$F_c(s) = \frac{\alpha_c}{s} G_c'^{-1}(s) = \frac{\alpha_c}{s}(\hat{L}_s s + R_s + R_a) \tag{2.84}$$

Furthermore, the appropriate controller parameters k_p and k_i can be determined as

$$F_c(s) = \alpha_c \hat{L}_s + \frac{\alpha_c(R_s + R_a)}{s} \tag{2.85}$$

Which indicates that

$$\begin{cases} k_{pc} = \alpha_c \hat{L}_s \\ k_{ic} = \alpha_c(R_s + R_a) \end{cases} \tag{2.86}$$

It is necessary to ensure the inner feedback $G_c'(s)$ has the same bandwidth as the entire closed-loop system $G_{ce}(s)$, which represents

$$G_c'(s) = \frac{\frac{1}{L_s}}{s + \frac{R_s + R_a}{L_s}} = \frac{g\alpha_c}{s + \alpha_c} \tag{2.87}$$

Therefore, the active resistance R_a can be expressed as a function dependent on α_c, given by

$$\frac{R_s + R_a}{L_s} = \alpha_c \Rightarrow R_a = \alpha_c L_s - R_s \tag{2.88}$$

2.4.2.4 Voltage Saturation and Antiwindup

Actually, due to the limitation of U_{DC}, the voltage magnitude generated by the PI controller cannot become extremely large. Therefore, the voltage value can be restricted by a limiter known as voltage saturation, which operates based on

$$u_{s,lim} = \begin{cases} u_s & |u_{s,max}| \geqslant |u_s| \geqslant 0 \\ u_{s,max} & |u_s| > |u_{s,max}| \end{cases} \tag{2.89}$$

Therefore, the PI current controller model can be expressed as

$$I = \int e dt \tag{2.90}$$

$$u_s = k_p e + k_i I + ffd \tag{2.91}$$

where I is the integrator state and ffd is the feed-forward disturbance compensation.

However, because of the integrator windup, the integral part of the PI controller continues to absorb control error and always gets overcharged until the windup starts accumulating negative control error. To adress this issue, another error signal $\bar{e}$ can be introduced into the integrator to limit the integration, when the output voltage is limited ($u_s = u_{s,max}$).

The PI controller considering voltage saturation and antiwindup term is modeled as Fig.2.21.

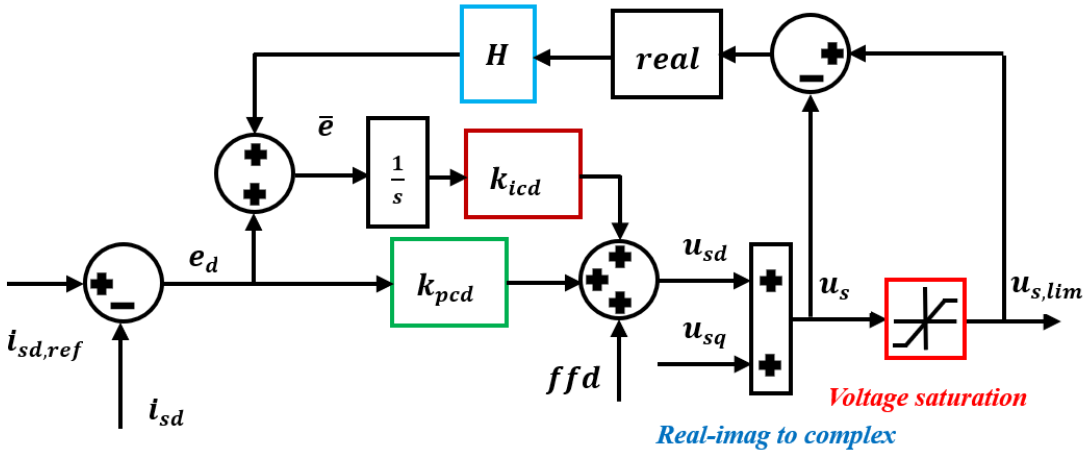

Figure 2.21: Voltage saturation and antiwindup in current controller

After adding antiwindup, the updated expression of output voltage $u_{s,lim}$ is

$$u_{s,lim} = k_p\bar{e} + k_i I + ffd \tag{2.92}$$

And through subtracting (2.91) from (2.92), the "back-calculated" error $\bar{e}$ and antiwindup parameter H are indicated as

$$\bar{e} = e + \frac{1}{k_p}(u_{s,lim} - u_s) \tag{2.93}$$

$$H = \frac{1}{k_p} \tag{2.94}$$

2.4.3 Speed Controller

Similar to the current controller, the purpose of the speed controller is to determine the reference torque by measuring the motor's operating speed and comparing it with the reference speed. In other words, it provides input to the MTPA controller to obtain the reference input current.

The closed-loop speed control system can be modeled in Fig.2.22. Here, the mechanical speed of the rotor is measured based on (2.10), which can be expressed as

$$\Omega_r = \frac{1}{sJ + B}(T_e - T_L) \tag{2.95}$$

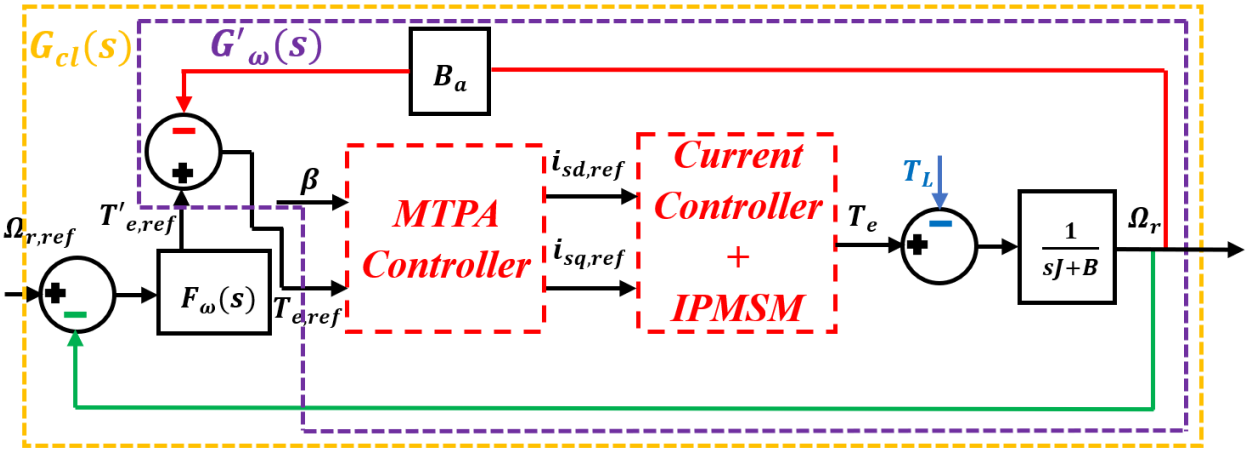

Figure 2.22: Closed-loop speed control system

The load torque T_L that enters the system is similar to the back-EMF in the current controller. Therefore, it is necessary to introduce an active damping B_a to reduce the impact of T_L. The transfer function from $T_{e,ref}$ to Ω_r with the bandwidth α_ω and the active damping can be expressed as

$$G'_{\omega}(s) = \frac{\Omega_r}{T_{e,ref}} = \frac{1}{sJ + B + B_a} = \frac{\frac{1}{J}}{s + \frac{B+B_a}{J}} = \frac{g\alpha_\omega}{s + \alpha_\omega} \tag{2.96}$$

$$\Rightarrow B_a = J\alpha_\omega - B$$

With the same bandwidth of α_ω of closed-loop system, the transfer function of speed controller is

$$G_{cl}(s) = \frac{\Omega_r}{\Omega_{r,ref}} = \frac{F_\omega(s)G'_\omega(s)}{1 + F_\omega(s)G'_\omega(s)} = \frac{\alpha_\omega}{s + \alpha_\omega} = \frac{\frac{\alpha_\omega}{s}}{1 + \frac{\alpha_\omega}{s}} \tag{2.97}$$

$$\Rightarrow \frac{\alpha_\omega}{s} = F_\omega(s)G'_\omega(s)$$

$$\Rightarrow F_\omega(s) = \frac{\alpha_\omega}{s}G'^{-1}_\omega(s) = \frac{\alpha_\omega}{s}(sJ + B + B_a) = J\alpha_\omega + \frac{J\alpha_\omega^2}{s}$$

Therefore, the parameter of PI controller $F_\omega(s)$ can be defined as

$$\begin{cases} k_{p\omega} = J\alpha_\omega \\ k_{i\omega} = J\alpha_\omega^2 \end{cases} \tag{2.98}$$

3

Case Setup

In this chapter, the design parameters and electric characteristics of the entire electric drive system will be modeled and discussed in detail, which includes the operating region of the electric machine, the power loss characteristics of SiC MOSFETs, and the reference input currents of the controller circuit, etc.

3.1 System setup

In this thesis, the schematic diagram of the entire electric drive system is shown in Fig.3.1, which mainly contains an electric machine, a power VSI circuit, and a controller circuit.

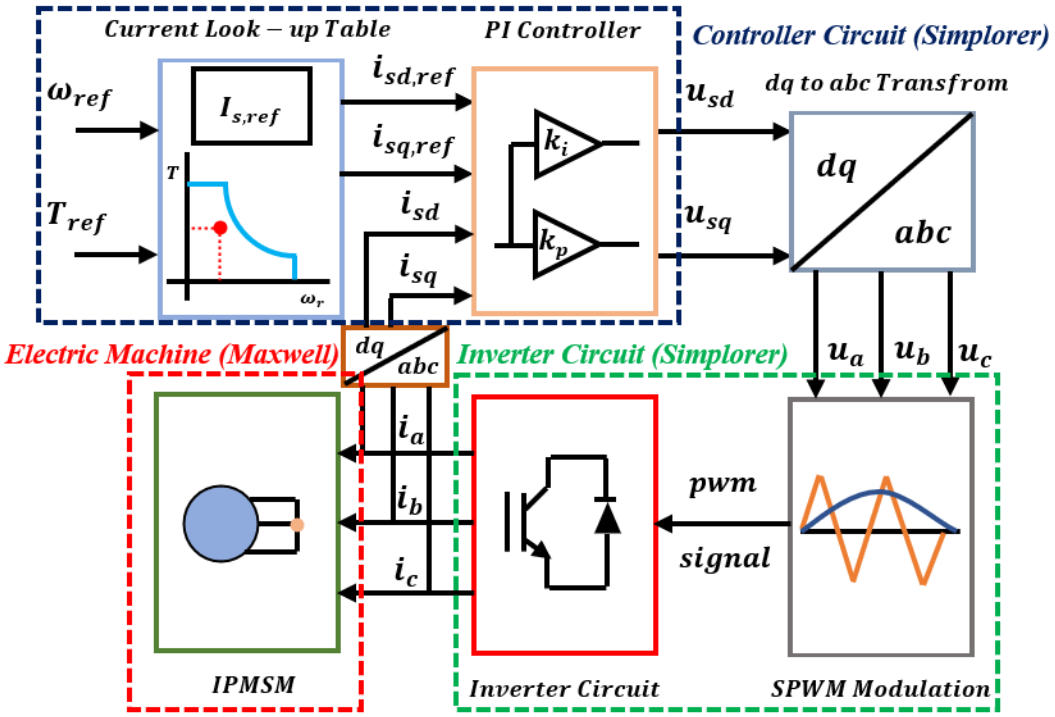

Figure 3.1: Co-simulation between Maxwell and Simplorer

The electric machine used in the system is a 3-phase IPMSM, which draws inspiration from the motor employed in the 2004 Toyota Prius[48]. However, certain modifications have been made to adapt it specifically for the purposes of this thesis.

The complete modeling and analysis of the electric machine are carried out using a FEM-based electromagnetic solver called Maxwell, which is a powerful tool for electromechanical analysis within the ANSYS platform[49].

The 3-phase VSI circuit is built using the library components available in Simplorer, a multi-physics circuit simulator within the ANSYS platform. This model can be interconnected with the machine model in Maxwell and perform a collaborative co-simulation.

Simplorer is also employed to develop a controller model that generates the 3-phase reference voltage as the input to the modulator, which are used to implement SPWM control. Simultaneously, the controller is also required to receive the 3-phase output current excitation from the inverter circuit.

3.2 Electric Machine

In this section, the development of a finite element model for the IPMSM, the calculation of the corresponding dynamic parameters, and the analysis of the fundamental performance of the IPMSM within the torque-speed envelope will be mainly presented.

3.2.1 FEM Model

The FEM model of IPMSM built in Maxwell is illustrated in Fig.3.2. The stator of the machine is modeled with 48 slots with a distributed double-layered short-pitch winding configuration. For improving the computational efficiency, the model size can be reduced to 1/8 of the original size, due to the presence of 8 identical poles.

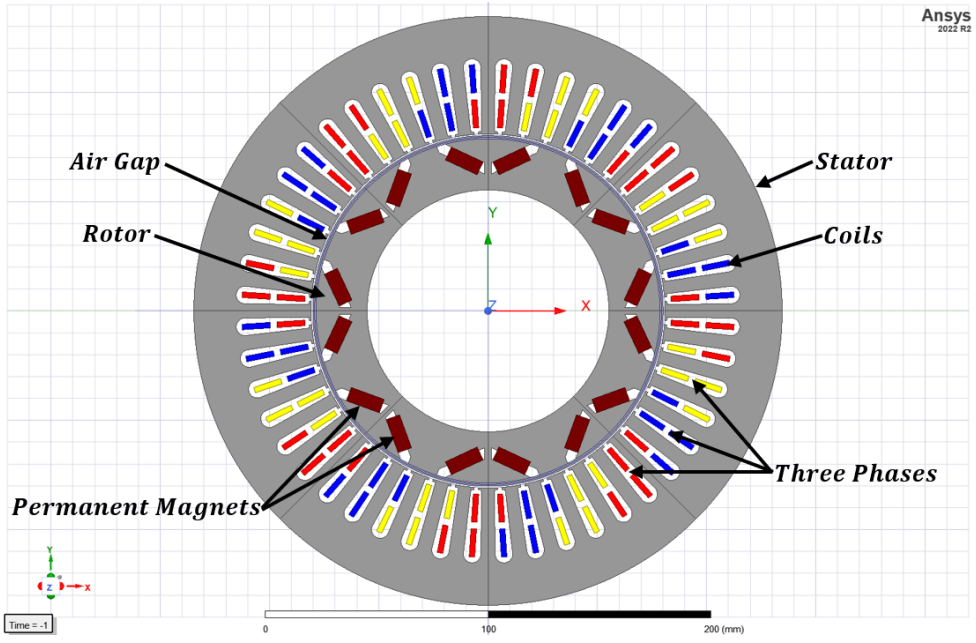

Figure 3.2: The 2D IPMSM model in ANSYS Maxwell

The model is created adopting the built-in *RMxprt* tool integrated within ANSYS, which is a template-based tool that allows for the specification of various parameters, including the type, dimensions, and other relevant details of different components. By feeding in the machine parameters, as demonstrated in Table 3.1, the tool can automatically assemble the comprehensive 2D model.

Table 3.1: Electric Machine Parameters - Type & Dimension

Part	Parameter	Symbol	Value	Unit
IPMSM	Rated power	P_{rated}	200	kW
	Power factor	$\cos\psi$	0.65	
	Stator winding resistance	R_s	0.046	Ω
	Stator end winding inductance	L_{ew}	9.438	μH
	Maximum operating speed	n_{max}	12000	rpm
	Number of phases		3	
	Number of pole pairs		4	
	Number of slots per pole per phase		2	
	Number of total slots		48	
	Number of parallel branches per phase		4	
	Depth	L	83.82	mm
Stator/ Slot	Core diameter on gap side		161.9	mm
	Core diameter on yoke side		269.24	mm
	Slot opening height	H_{s0}	1.03	mm
	Slot closed bridge height	H_{s01}	0	mm
	Slot wedge height	H_{s1}	0	mm
	Slot body height	H_{s2}	29.5	mm
	Slot opening width	B_{s0}	1.93	mm
	Slot wedge maximum width	B_{s1}	5	mm
	Slot body bottom width	B_{s2}	8	mm
	Slot body bottom fillet		5	mm
Rotor/ Magnet	Core diameter on gap side		160.4	mm
	Core diameter on yoke side		110.64	mm
	Limited diameter of PM ducts	D_1	157.44	mm
	Bottom width for separate duct	O_1	3	mm
	Distance from duct bottom to shaft surface	O_2	7.28	mm
	Duct thickness	B_1	4.7	mm
	Rib width		14	mm
	Rib height		3	mm
	Minimum distance between side magnets		4.5	mm
	Magnet thickness		6.48	mm
	Total width of all magnet per pole		32	mm

Table 3.2 presents the materials and their corresponding properties for the different components of the IPMSM. Specifically, the stator and rotor core are constructed using silicon steel, while neodymium magnets and copper are utilized for the PMs and coils, respectively.

Table 3.2: Electric Machine Parameters - Material

Part	Parameter	Symbol	Value/Name	Unit
Stator/ Rotor	Iron material of stator/rotor		M19_29G	
	Iron mass density	ρ_{fe}	7872	kg/m^3
	Hysteresis loss coefficient	k_h	184.23	
	Eddy current loss coefficient	k_c	0.386	
	Excess loss coefficient	k_e	0.27	
Magnet	Magnet material		N36Z_20	
	Magnet relative permeability	μ_r	1.03	
	Magnet bulk conductivity	σ	625000	$siemens/m$
	Magnet magnitude	H	-920000	$A/meter$
Coil	Coil material		Copper	
	Copper relative permeability	μ_r	0.999991	
	Copper bulk conductivity	σ	58000000	$siemens/m$
	Copper mass density	ρ_{cu}	8933	kg/m^3

The loss curves depict the relationship between iron loss density and flux density, as shown in Fig.3.3. These curves provided from the material datasheet from the core material manufacturer, and can be fed into the material properties to calculate iron losses under different frequencies.

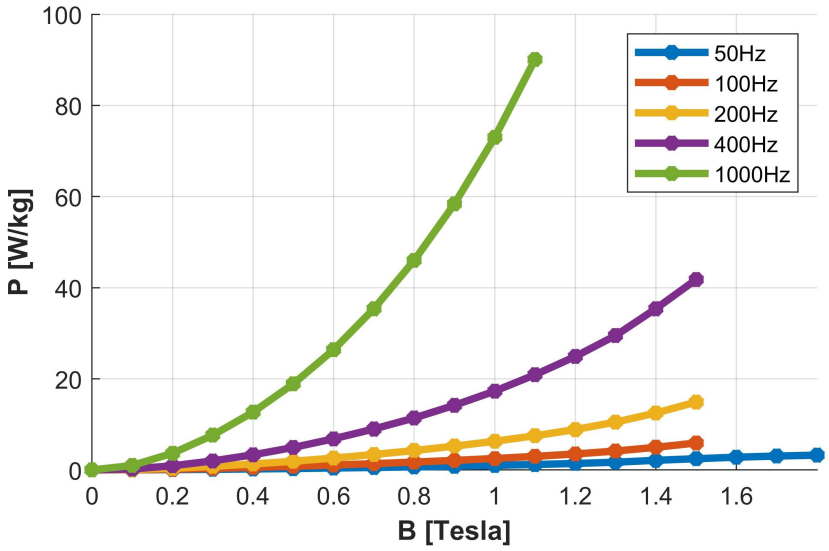

Figure 3.3: Relationship between iron loss density and flux density under different frequency

Subsequently, the external current excitation is applied to the coils, together with a set of boundary conditions. And a transient analysis setup is established to carry out simulations under different operating conditions.

Fig.3.4 displays the mesh division map of the machine. It is noteworthy that a coarser mesh division can damage accuracy, while an excessively fine mesh division can greatly increase simulation time. Therefore, an adaptive element length-based refinement is employed in this model, with the maximum mesh length for each component illustrated in the table on the left side of the figure.

Element Name	*Max. Length of Meshes*
Stator	*4 mm*
Rotor	*3 mm*
Coils	*4 mm*
Magnets	*3 mm*
Air Gap	*3 mm*

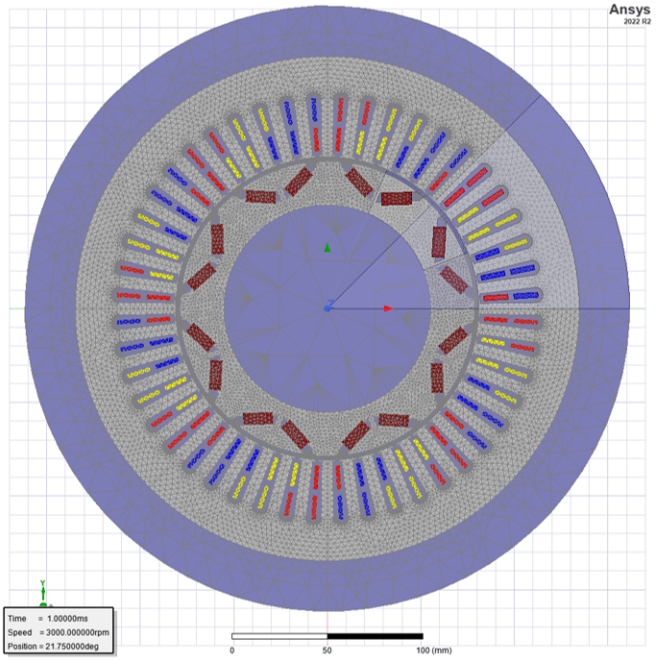

Figure 3.4: The mesh division map with the maximum mesh length at different part of IPMSM

3.2.2 Dynamic Parameter Distribution

In the *dq*-coordinate system, the stator inductance and flux linkages are dependent on the stator currents i_s, rather than maintaining fixed values. According to (2.5)-(2.6), which solely takes into account the influence of i_{sd} and i_{sq}, the equations can be reformulated as

$$\psi_d(i_{sd}, i_{sq}) = L_{sd}(i_{sd}, i_{sq}) \cdot i_{sd} + \psi_m(i_{sq}) \tag{3.1}$$

$$\psi_q(i_{sd}, i_{sq}) = L_{sq}(i_{sd}, i_{sq}) \cdot i_{sq} \tag{3.2}$$

Therefore, both the voltage and output torque not only depends on the current, but also on the L_s and ψ_m, which are displayed as

$$u_{sd}(i_{sd}, i_{sq}) = R_s i_{sd} - \omega_r L_{sq}(i_{sd}, i_{sq}) \cdot i_{sq} \tag{3.3}$$

$$u_{sq}(i_{sd}, i_{sq}) = R_s i_{sq} + \omega_r L_{sd}(i_{sd}, i_{sq}) \cdot i_{sd} + \omega_r \psi_m(i_{sq}) \tag{3.4}$$

$$T_e(i_{sd}, i_{sq}) = \frac{3n_p}{2}(\psi_m(i_{sq}) \cdot i_{sq} + (L_{sd}(i_{sd}, i_{sq}) - L_{sq}(i_{sd}, i_{sq})) \cdot i_{sd} i_{sq}) \tag{3.5}$$

In this situation, a 2D interpolation technique is used to obtain continuously varying values of L_{sd}, L_{sq} and ψ_m with respect to the values of i_{sd} and i_{sq}. To establish a reference map for interpolation, a set of 10 $\times$ 10 combinations of i_{sd} and i_{sq} within the appropriate range (slightly higher than the rated current but within maximum absolute value limits) are selected. These combinations are applied under fixed IPMSM simulation conditions in Maxwell, which are illustrated in Fig.3.5.

$\frac{i_{sd}}{\sqrt{2}}[A]$	$\frac{i_{sq}}{\sqrt{2}}[A]$
−450	−50
−400	0
−350	50
−300	100
−250	150
−200	200
−150	250
−100	300
−50	350
0	400
50	450

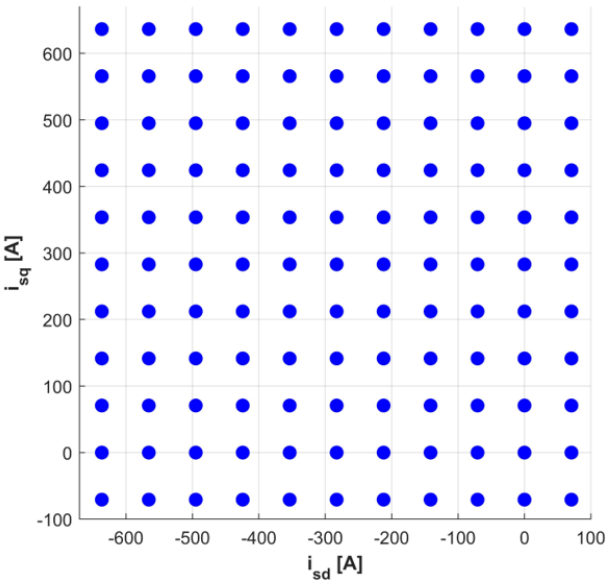

Figure 3.5: The distribution map of tested *dq*-current combinations

Following the simulation, the obtained results contain 3-phase electrical quantities such as currents, voltages, flux linkage, and losses. These quantities are transformed into the *dq*-coordinate system to simplify the calculation. Based on equations (2.5) and (2.6), L_{sd} and L_{sq} can be calculated as

$$L_{sd} = \frac{\psi_d - \psi_m}{i_{sd}} \tag{3.6}$$

$$L_{sq} = \frac{\psi_q}{i_{sq}} \tag{3.7}$$

When $i_{sd} = 0A$, according to (2.5), the flux linkage in the *d*-direction ψ_d is equal to the magnetic flux linkage ψ_m. Therefore, through processing the *dq*-flux linkage generated under all current combinations where $i_{sd} = 0A$, the value of ψ_m can be directly achieved. The distribution map of ψ_m is illustrated in Fig.3.6, and it is evident that ψ_m solely depends on i_{sq}.

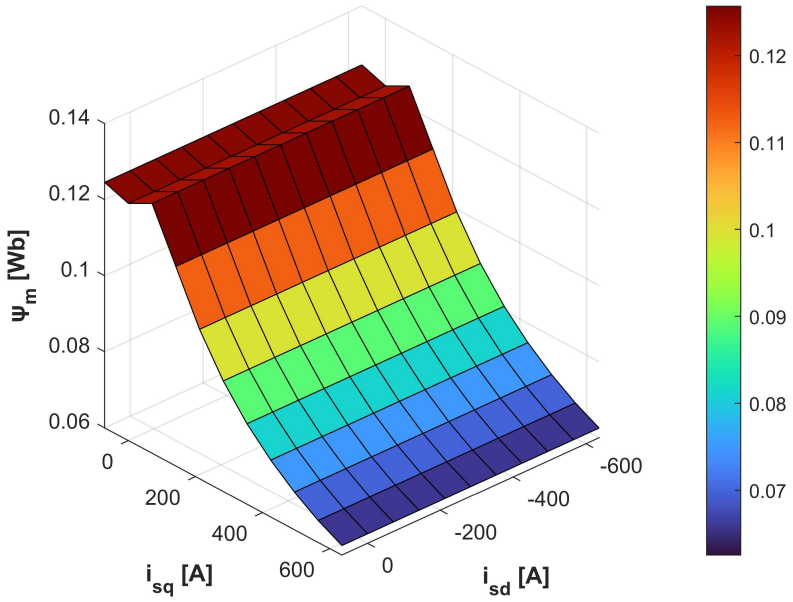

Figure 3.6: The distribution of ψ_m across dq-current combinations

Similarly, the distribution map of L_{sd} and L_{sq} can be calculated from (3.6) and (3.7), as illustrated in Fig.3.7. It should be noted that when both i_{sd} and i_{sq} are equal to $0A$, L_{sd} and L_{sq} tend to approach infinity, which does not accurately reflect the real situation. In order to obtain the value at these points, a series of additional operating points are introduced, where i_{sd} and i_{sq} are $50A$ and -$50A$ respectively. These points are used for calculating interpolation.

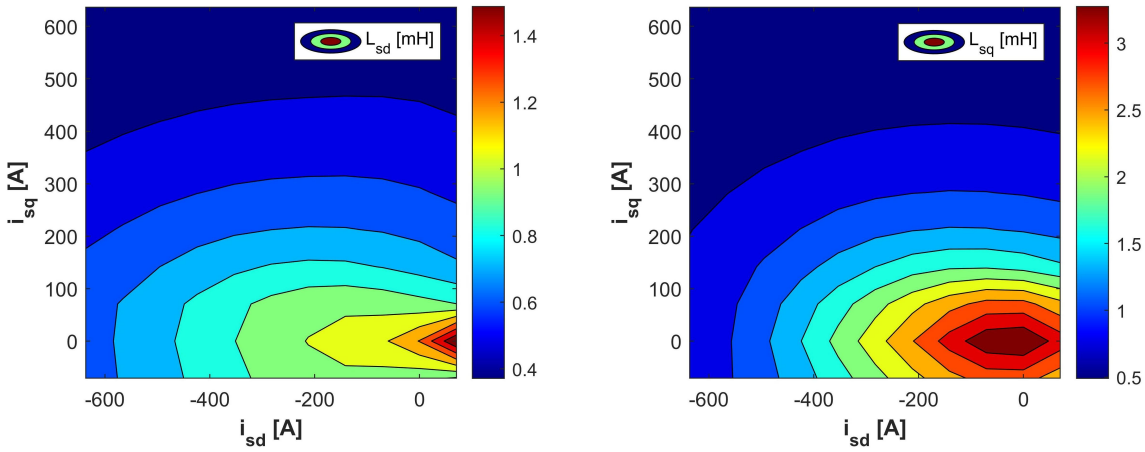

Figure 3.7: The distribution of L_{sd} (left) and L_{sq} (right) across dq-current combinations

Other IPMSM outputs, such as the output torque T_e, can serve as the reference for verifying the accuracy of the dynamic parameter distribution map. The torque obtained from the simulation results in Maxwell and the torque calculated based on (3.5) employing the dynamic parameters of L_{sd}, L_{sq} and ψ_m are presented in 3.8,

together with the corresponding error distribution.

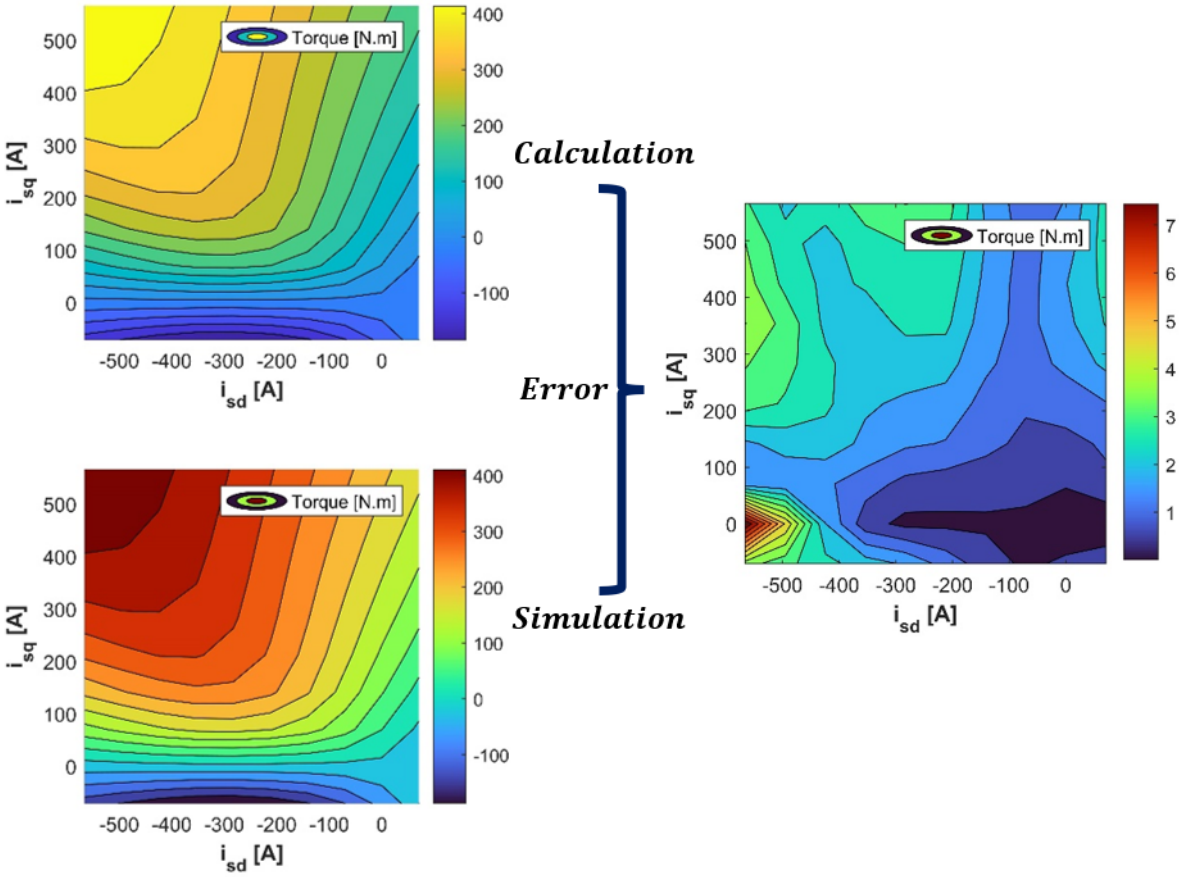

Figure 3.8: The distribution of output torque from equation (left) and Maxwell (right) across *dq*-current combinations

Overall, the error between the calculated and simulated torque values is not significant, with a maximum discrepancy of only $7N \cdot m$. Within the rated operating current range of the IPMSM, the error typically falls between 0 and $3N \cdot m$. This confirms that the calculation of motor dynamic parameters is sufficiently accurate.

3.2.3 Limitations for Stator Current and Voltage

The stator current and voltage limit boundaries of the IPMSM under different operating speeds, along with the output torque distribution, are displayed in Fig.3.9. These limits are determined by (2.3) and (2.4), considering the dynamic parameters of the motor.

In the figure, the voltage limit boundaries are shown for different operating speeds ranging from 2500-12000rpm. These boundaries determine the range of *dq*-current at each operating speed, preventing the motor stator voltage from exceeding its limit of $320V$. The black line represents the maximum current limit of $641A$. These limit boundaries define the operating region of the IPMSM across various speeds.

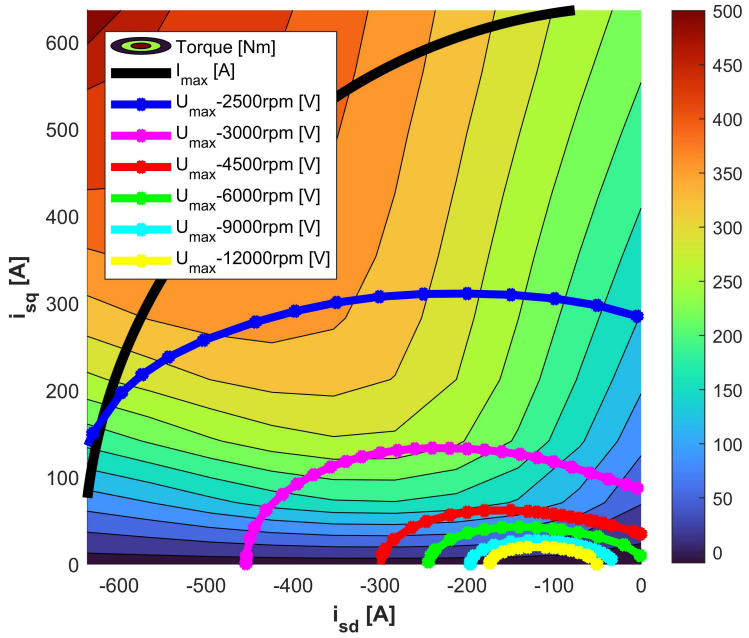

Figure 3.9: The stator current and voltage limit boundaries along with the torque distribution across *dq*-current combinations

3.2.4 Power Losses of IPMSM

Fig.3.10 illustrates the distribution of copper losses across *dq*-coordinate system. As stated in (2.18), the copper losses in an IPMSM are proportional to the square of the stator current and the winding resistance in an electrical system. Notably, these copper losses remain independent of the operating speed.

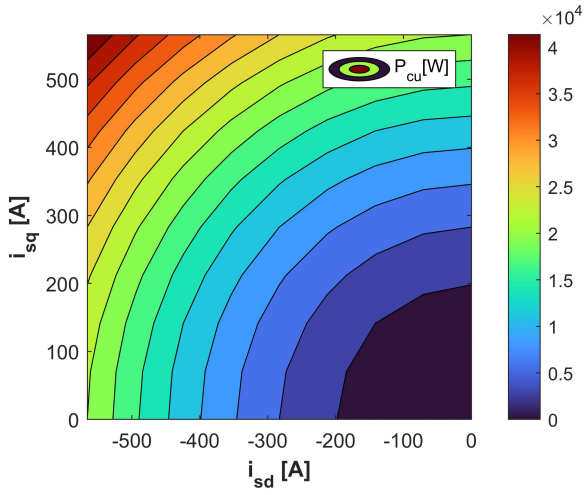

Figure 3.10: The distribution of copper losses across *dq*-current combinations

In contrast to copper losses, iron losses are influenced by both the stator current and the operating speed. As depicted in Fig.3.11, it is noticeable that the iron losses gradually increase as the speed rises within the range of 1000-12000rpm.

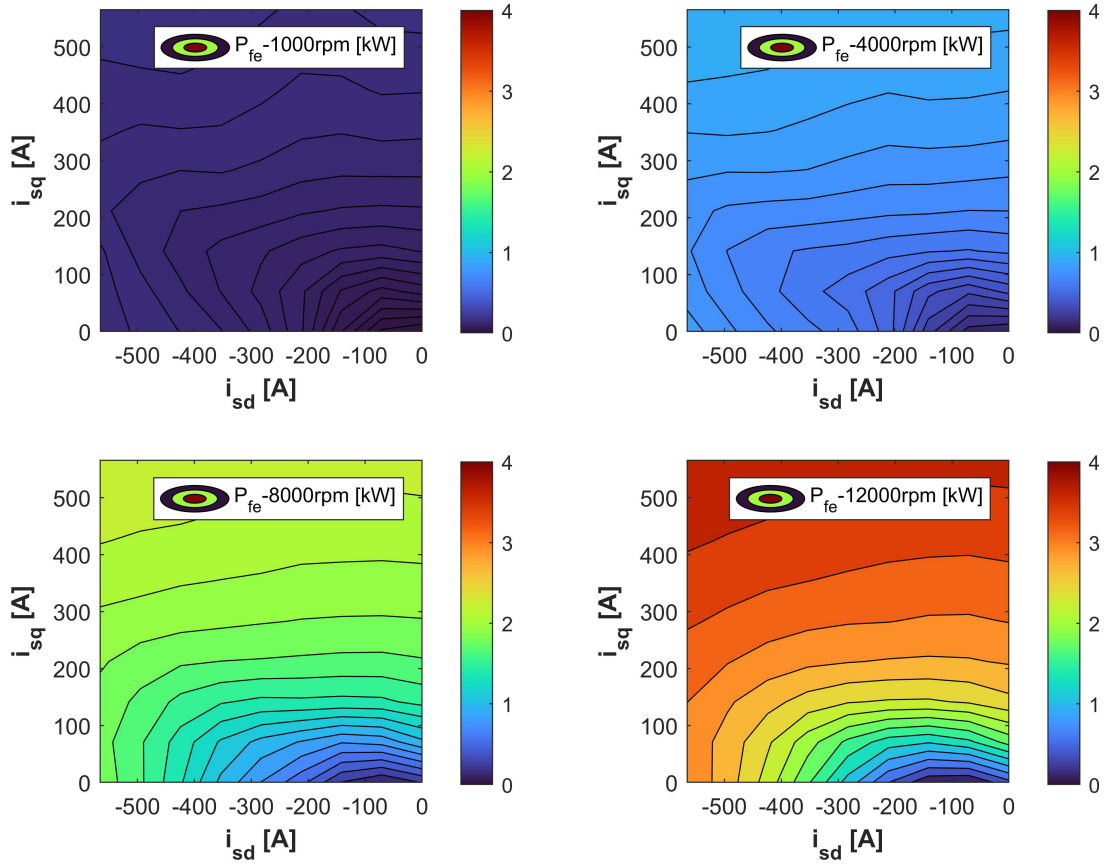

Figure 3.11: The distribution of iron losses across all current combinations at diverse operating speed

Fig.3.12 illustrates that at the given *dq*-current combinations, the rise of iron losses exhibits a linear trend with the increase in speed. However, when the same speed is contemplated, the increase in iron losses decelerates as the current goes up.

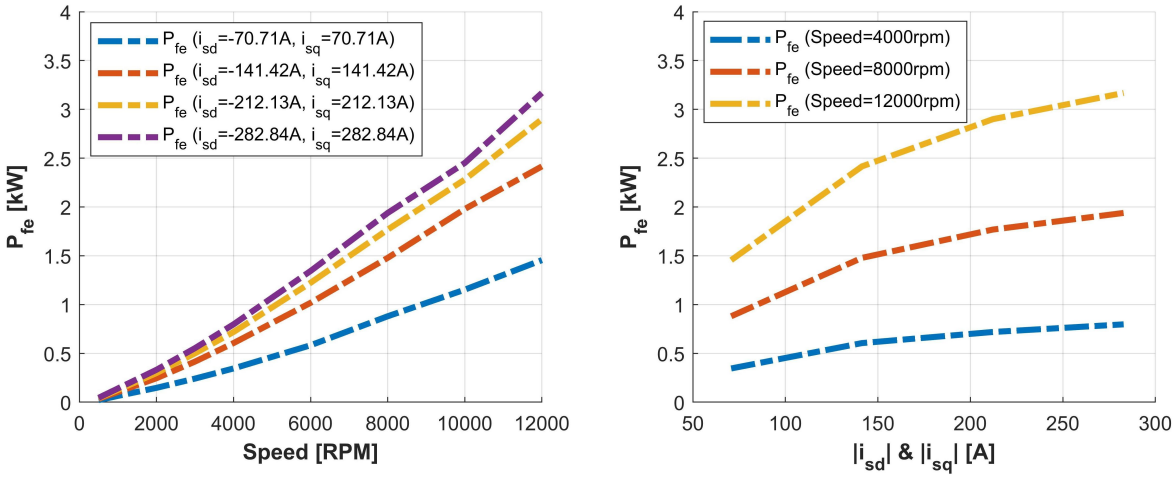

Figure 3.12: The variation of iron losses with respect to the operating speed (left) and stator current (right)

3.2.5 Operating Region Determination

The operational range of an IPMSM can be generally categorized into two different regions: the constant torque region and the constant power region. In the constant torque region, the maximum achievable torque generated by the IPMSM depends on both the peak phase current amplitude $i_{s,max}$ and the current angle β.

The determination of the β that corresponds to the $i_{s,max}$ includes applying a non-linear programming method, specifically the MATLAB function $fmincon$. This method facilitates the automatic calculation of the β while considering the current limitations. By iteratively adjusting β within these limits, the objective is to identify the β that yields the maximum output torque. This approach allows for the optimization of torque production in the IPMSM.

In Fig.3.13, the optimal input dq-current combination that generates the maximum torque is indicated by the blue point. The figure also provides visualizations of the torque distribution, the corresponding current angle, and the limit boundary of the current magnitude.

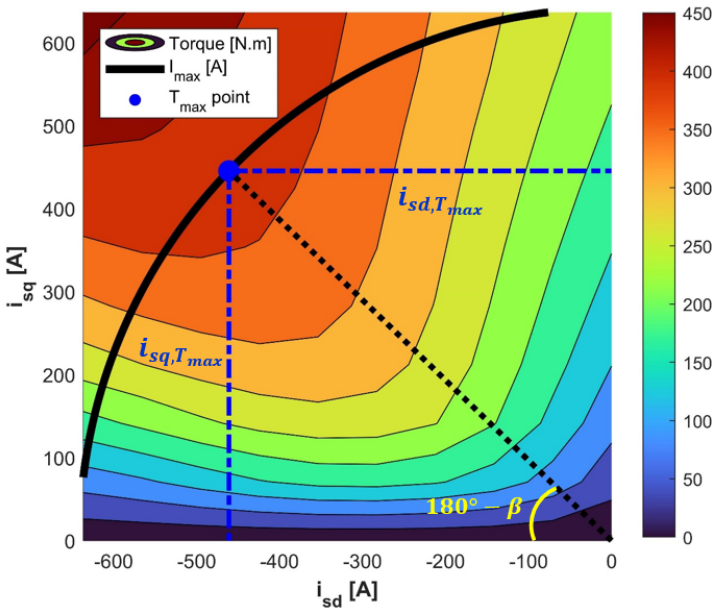

Figure 3.13: The dq-current Combination that Generate Maximum Torque

For the given configuration, the calculated β is measured at approximately 135.98 degrees. This value indicates that the corresponding i_{sd} and i_{sq} are -460.99A and 445.43A respectively. These current values represent the optimal current flow in the IPMSM, resulting in the maximum torque generation.

The 2D interpolation method $interp2$ is utilized to obtain the corresponding values of L_{sd}, L_{sq} and ψ_m based on the discussed distribution maps. This method employs the value of i_{sd} and i_{sq} that generate the maximum torque and provides the interpolated values for L_{sd}, L_{sq} and ψ_m. Subsequently, the function $fsolve$ is employed to

determine the rotor speed at which the stator voltage reaches its peak, representing the rated speed of the IPMSM. Through this calculation, the rated speed is identified as $2322rpm$.

In the constant power region, the peak torque produced by the IPMSM begins to diminish as the rotor speed increases, due to the imposition of field-weakening control. Consequently, the constant torque characteristic becomes less sustainable. To address this situation, it is crucial to identify a suitable range of operating speeds within this region. Moreover, determining the optimal values for maximum torque, output power and dq-current associated with these identified speeds is also essential. These chosen parameters are demonstrated in Table 3.3.

Table 3.3: Parameters Within the Different Operating Speeds During Field-weakening Control

Speed $[rpm]$	T_{max} $[Nm]$	P_e $[kW]$	i_{sd} $[A]$	i_{sq} $[A]$
2322	414.46	100.78	-460.99	445.43
4000	176.06	73.75	-216.20	71.18
6000	102.90	85.18	-168.06	41.48
8000	72.40	60.65	-148.40	29.90
10000	55.82	58.45	-137.67	23.53
12000	45.44	57.10	-131.08	19.46

Fig.3.14 depicts the relationships between shaft torque, output power and rotor speed, providing an overview of the example operating points within the IPMSM. In the graph, the solid line represents the torque and power in the constant torque region, where the motor operates at its maximum torque capability. Conversely, the dotted line represents the torque and power within the field-weakening region.

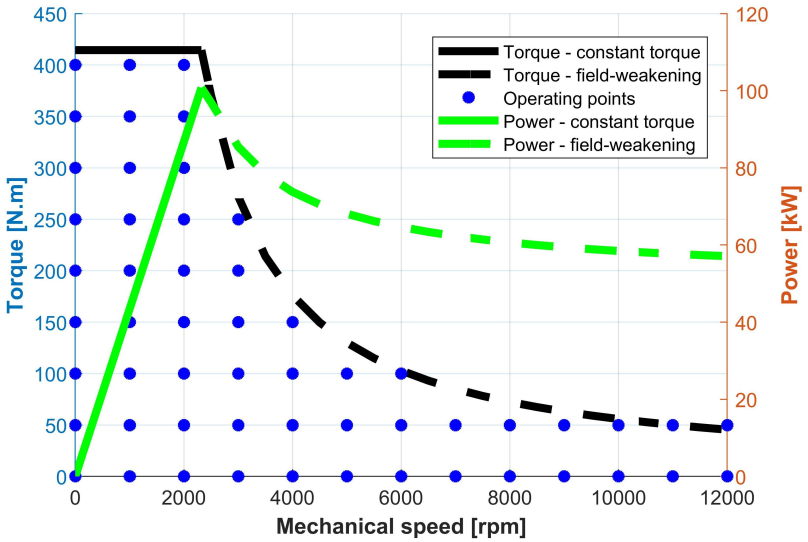

Figure 3.14: Torque-speed and power-speed lines with represented operating points of an IPMSM

It is worth noting that when the motor operates at a speed exceeding its rated value, the output power continuously drops with rising speed rather than remaining a constant value. This phenomenon occurs because the motor is constrained by the maximum voltage and the minimum demagnetization current in this range, which prevents it from maintaining its maximum torque produced. As the speed continues to rise, the maximum torque gradually decreases, resulting in a decline in output power.

This visualization allows for a better understanding of how the torque and power characteristics vary in different regions of operation, providing insights into the performance of the IPMSM.

3.3 Power Inverter Circuit

A three-phase power inverter circuit is constructed using the component library available in Simplorer. The model consists of 24 power SiC MOSFETs and 24 body diodes, as shown in Fig.A.2. In order to operate these MOSFETs, 6 gate drivers are parameterized and employed according to the specification of the MOSFETs.

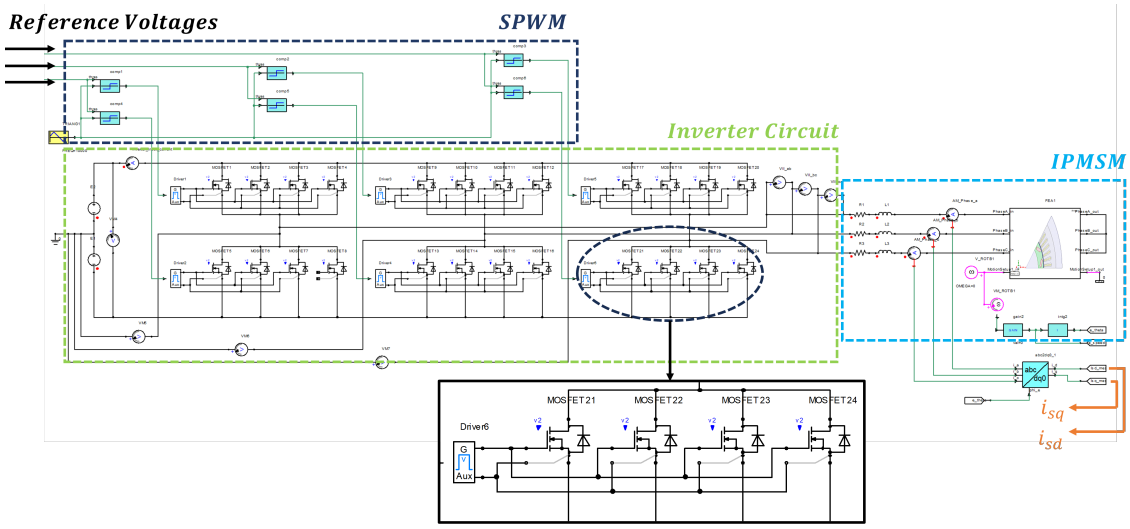

Figure 3.15: Power inverter circuit combined with IPMSM in Simplorer

The transient co-simulation of an IPMSM and an inverter circuit was performed by integrating the 2D model from Maxwell with Simplorer. Based on the desired operating point derived from the IPMSM analysis, the reference dq-current can be obtained. The control circuit utilized these reference currents to calculate the corresponding reference dq-voltage and transformed it to 3-phase voltages. These reference voltages are then fed into the inverter circuit to implement SPWM control.

This process resulted in the generation of a three-phase PWM voltage output containing the fundamental voltage and other high-frequency harmonic components. For example, a voltage waveform with parameters $M_a = 0.75$, $f_{el} = 200Hz$, and $f_{sw} = 10kHz$ is simulated and the result is shown in Fig.3.16.

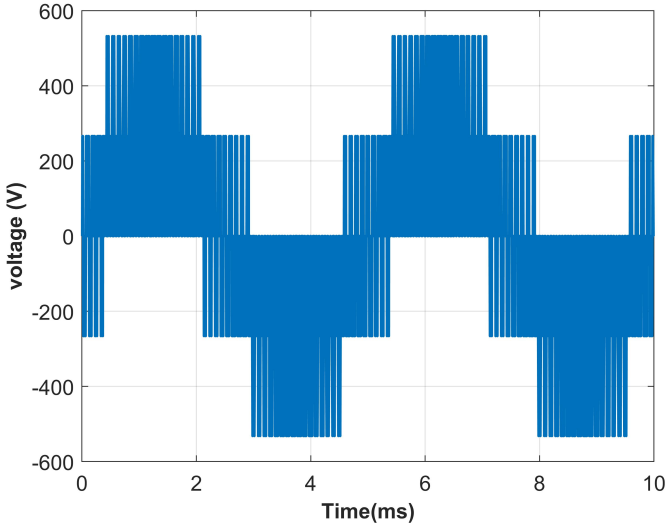

Figure 3.16: Line to neutral voltage in phase A (SPWM)

Fig.3.17 shows the harmonic spectrum of the voltage waveform evaluated using the fast Fourier transform (FFT) function. The major significant side-band harmonics are in the form of $af_{sw} \pm bf_{el}$, where a and b are integers and $a+b$ is an odd integer.

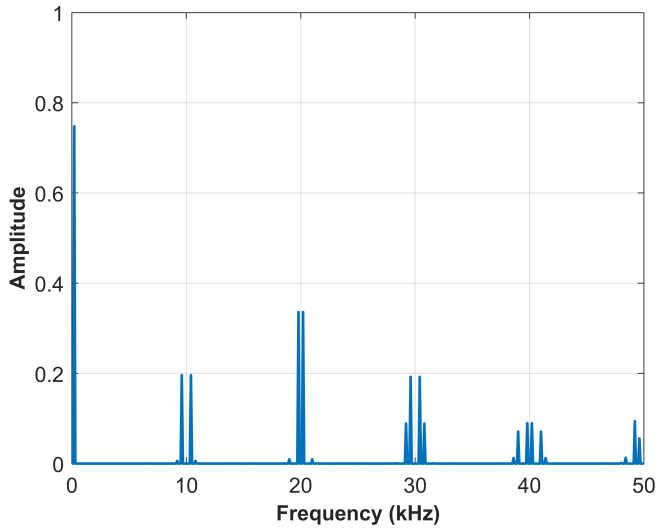

Figure 3.17: Harmonic spectrum of line to neutral voltage in phase A (SPWM)

3.3.1 Power Inverters

The DC-link voltage generated from the power battery side is $800V$, with the corresponding breakdown voltage at $1200V$[37]. In this thesis, the power SiC MOSFET $CAS300M17BM2$ manufactured by $Cree$, with a breakdown voltage of $1700V$ is selected as the switching component. The main characteristics of this MOSFET type, including its body diode, are described in Table 3.4.

Table 3.4: Inverter Parameters

Parameter	Symbol	Value	Unit	Test conditions
Maximum Parameters				
Drain-source voltage	V_{DS}	1700	V	
Gate-source voltage (max)	V_{GSmax}	-10∼25	V	
Gate-source voltage (typ.)	V_{GSop}	-5∼20	V	
DC continues drain current	I_D	325	A	T_c=25°C
		225	A	T_c=95°C
DC source-drain current (diode)	I_{SDBD}	556	A	T_c=25°C
		353	A	T_c=95°C
MOSFET Characteristics				
Drain-source breakdown voltage	$V_{(BR)DSS}$	1700	V	
Gate threshold voltage (typ.)	$V_{GS(th)}$	2.5	V	I_{DS}=104mA
Gate-source leakage current	I_{GSS}	1	nA	
Drain-source on-state resistance	$R_{DS(on)}$	8.0	$m\Omega$	T_c=25°C
Turn-on switching energy	E_{on}	13.0	mJ	T_c=150°C
Turn-off switching energy	E_{off}	10.0	mJ	T_c=150°C
Input capacitance	C_{iss}	20	nF	
Output capacitance	C_{oss}	2.5	nF	
Reverse transfer capacitance	C_{rss}	80	pF	
Thermal resistance, junction-case	R_{th-JCM}	0.067	°C/W	
Body Diode Characteristics				
Forward voltage	V_{SD}	1.7	V	T_c=25°C
		2.2	V	T_c=125°C
Total capacitive charge	Q_c	4.4	μC	
Thermal resistance, junction-case	R_{th-JCD}	0.060	°C/W	

Each electrical parameter is determined under specific testing conditions, such as junction temperature, gate-source voltage, and drain current, which can be regarded as references. However, it is important to note that in practical applications, these parameters may exhibit variations under different working conditions. Therefore, it is necessary to reevaluate or recalibrate the parameters to ensure their suitability for the specific operating conditions.

3.3.1.1 Effect of Gate Resistance

SiC inverters provide a wide bandwidth of switching speeds, improving energy efficiency and power density. Fig.3.18 shows the turn-on and turn-off switching waveforms of the MOSFET with various gate resistances. Also shown in Table 3.5, apparently, a smaller gate resistance results in a faster switching speed and lower switching energy. However, parasitic inductance and capacitance become larger as the switching speed increases, which leads to an increase in turn-on and turn-off losses.

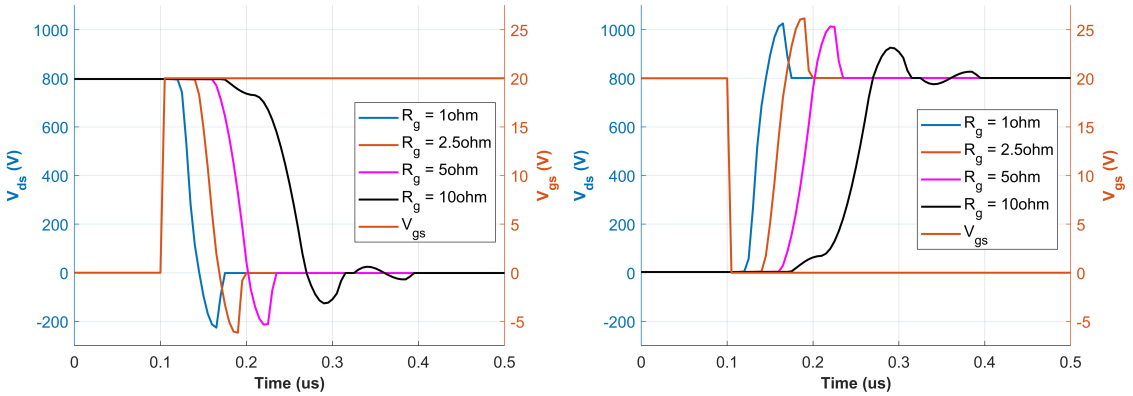

Figure 3.18: Turn-on (left) and turn-off (right) switching waveform with various gate resistances

High switching speeds and high switching frequency may lead to overvoltage at the motor terminals and also the generation of electromagnetic interference (EMI) [50]. These excessive overvoltages and the ringing effects the motor insulation causing deterioration and subsequent failure of the motor. The EMI generated may also cause nearby components to malfunction leading to system failure.

Table 3.5: Slew Rates of the used SiC Module

Gate resistance(Ω)	**Turn-on Slew Rate (V/ns)**	**Turn-off Slew Rate (V/ns)**
1	42.67	42.67
2.5	42.67	42.67
5	21.33	21.33
10	14.22	14.22

3.3.1.2 Thermal Model of Inverters

In power electronic inverters, the junction temperature is influenced by both the power losses P_l and the thermal resistance R_{th}, as described in (2.65). The thermal model of the $CAS300M17BM2$ is depicted in Fig.3.19, illustrating the power losses and thermal resistance at each stage of the heat transfer process, as well as the temperature at each layer.

During the heat conduction process from the junction to the base plate, the temperature at the junction of the MOSFET $T_{J,Mos}$ and the body diode $T_{J,Dio}$ may differ due to their different power losses and thermal resistances. However, as heat is transferred from the case plate to the ambient conditions, the temperature across each layer becomes uniform.

Nowadays, the hybrid electric vehicles use a separate liquid cooling system with coolant temperature at 65°C, together with the 105°C engine cooling system[51]. The coolant is used to specifically remove the heat from the electric drive system,

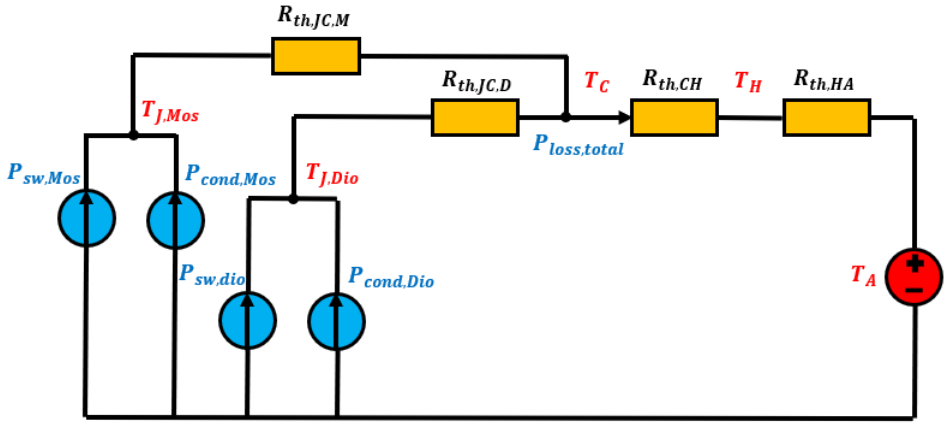

Figure 3.19: Thermal Model of Power SiC MOSFET $CAS300M17BM2$

considering the temperature limitations of power electronics. As a result, the ambient temperature T_A of the thermal system is set at 65°C, which corresponds to the temperature of the coolant.

At the beginning, T_J is assumed to be equal to the coolant temperature (65°C), and the corresponding electric parameters are determined accordingly. However, in reality, the actual T_J exceeds 65°C due to the thermal conduction from ambient conditions to the junction. This temperature difference introduces an error between the simulated and actual power losses.

An iterative method can be employed to reasonably estimate T_J using power losses and thermal resistance, as depicted in Fig.3.20. Due to the absence of $R_{th,CH}$ and $R_{th,HA}$ in the datasheet, the thermal resistance from the coolant to the junction can be simplified as $R_{th,JC}$.

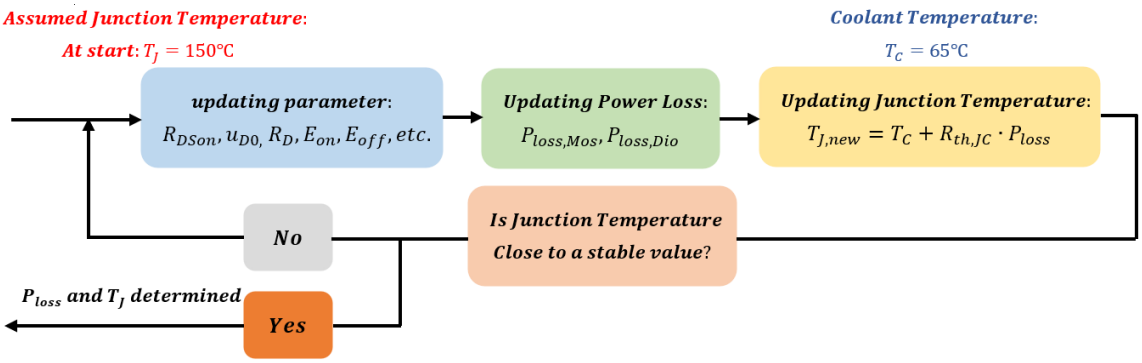

Figure 3.20: Flow chart for determining junction temperature

Firstly, based on the worst-case conditions specified in the datasheet ($T_J = 150$°C), the corresponding power losses can be determined, and the T_J can be updated according to (2.65). For a more accurate estimation, the parameters obtained at the updated T_J can be utilized to calculate the new power losses, which can in turn provides a new T_J. This iterative process can be repeated several times until

T_J approaches a stable value, allowing for determination of the actual junction temperature and power losses.

3.3.1.3 Determination of Electrical Characteristics

As mentioned previously, the accurate determination of significant electrical parameters, such as R_{DSon}, E_{on} and E_{off}, is crucial for power losses calculation under specific operating conditions. In the case of an IPMSM, different operating regions require various drain currents, leading to varying degrees of power losses.

These variations in power losses result in different junction temperatures through thermal conduction, subsequently impacting the inverter parameters. Therefore, it is necessary to establish a series of models representing the electrical parameters of the $CAS300M17BM2$, considering the variations in test conditions as specified in the datasheet.

The conduction loss of SiC MOSFETs is greatly influenced by R_{DSon}. The relationship between R_{DSon} and I_{DS}, as well as R_{DSon} and T_J is illustrated in Fig.3.21.

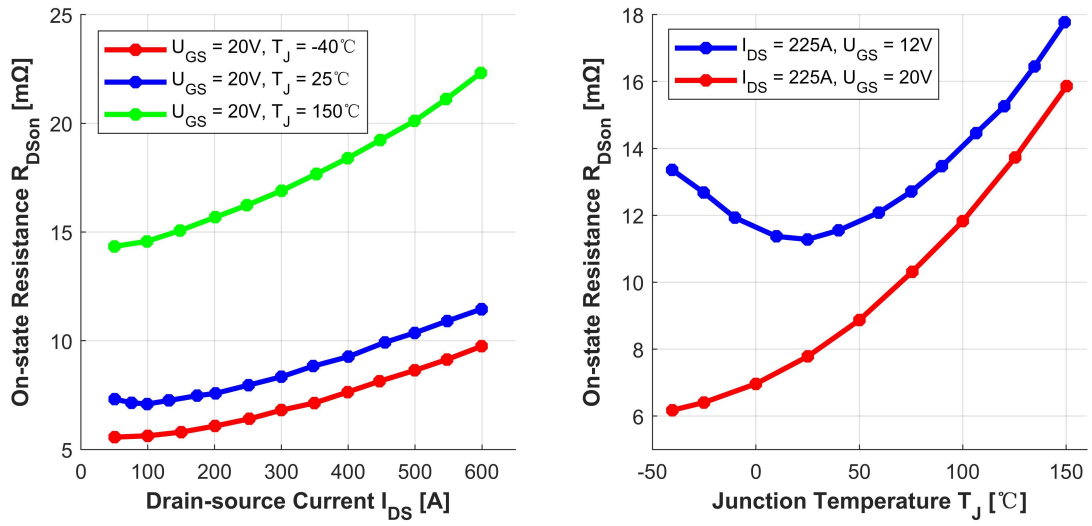

Figure 3.21: On-state resistance vs drain current (left) and On-state resistance vs junction temperature (right) in MOSFET

When U_{GS} equals to $20V$, both of the above two relationships at T_J=25°C and I_{DS}=225A can be modeled by cubic polynomial functions, which can be expressed as

$$\begin{cases} R_{DSon} = a_1 I_{DS}^3 + a_2 I_{DS}^2 + a_3 I_{DS} + a_4 \\ R_{DSon} = b_1 T_J^3 + b_2 T_J^2 + b_3 T_J + b_4 \end{cases} \tag{3.8}$$

In Fig.3.22, the relationship between U_{DS} and I_{DS} of body diode under different testing temperatures is clearly modeled on the left. It is worth noting that the conduction loss of the body diode is estimated using the diode's on-state zero-current

voltage V_{D0} and diode on-state resistance R_D, which can be represented by the line intercept with the x-axis and its slope.

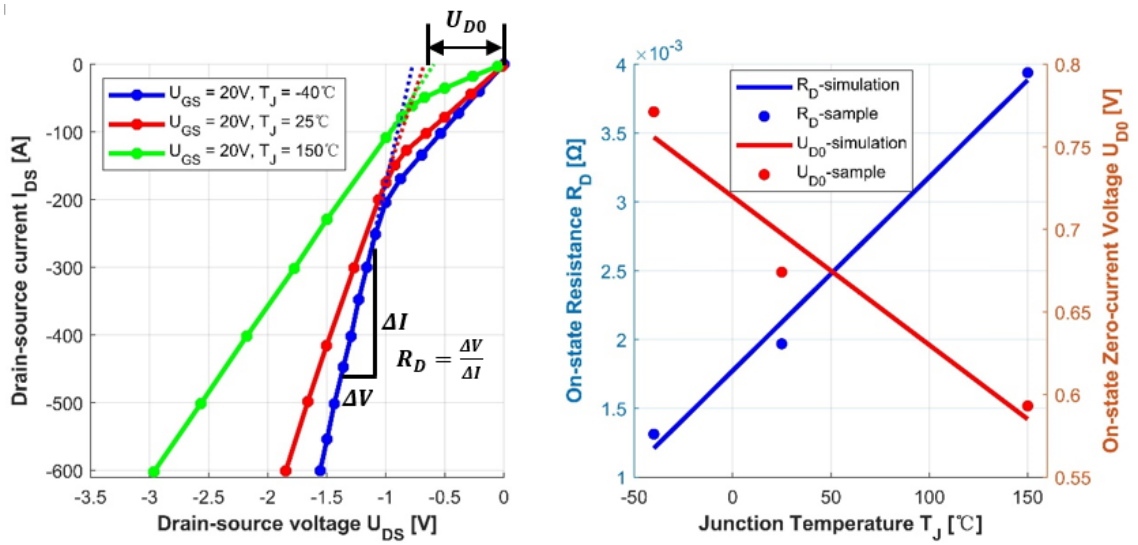

Figure 3.22: Drain-source current vs drain-source voltage (left) and on-state resistance/on-state zero-current voltage vs junction temperature (right) in diodes

After obtaining the data of V_{D0} and R_D at different temperatures, the relationship between V_{D0}/R_D and T_J can be modeled as shown on the right side, which are expressed by

$$\begin{cases} V_{D0} = c_1 T_J + c_2 \\ R_D = d_1 T_J + d_2 \end{cases} \tag{3.9}$$

Similarly, the turn on/off switching energy in MOSFETs is influenced by the junction temperature, drain-source voltage and current to a certain extent. Under normal conditions, the relationship between switching energy loss and V_{DS}/I_{DS} can be directly determined based on the datasheet. This relationship can be expressed as

$$E_x = \frac{E_{x,datasheet}}{V_{DS,ref} \cdot I_{DS,ref}} V_{DS} I_{DS} \tag{3.10}$$

However, it is also necessary to construct corresponding models to illustrate the impact of temperature on E_{on}/E_{off}, as revealed in Fig.3.23.

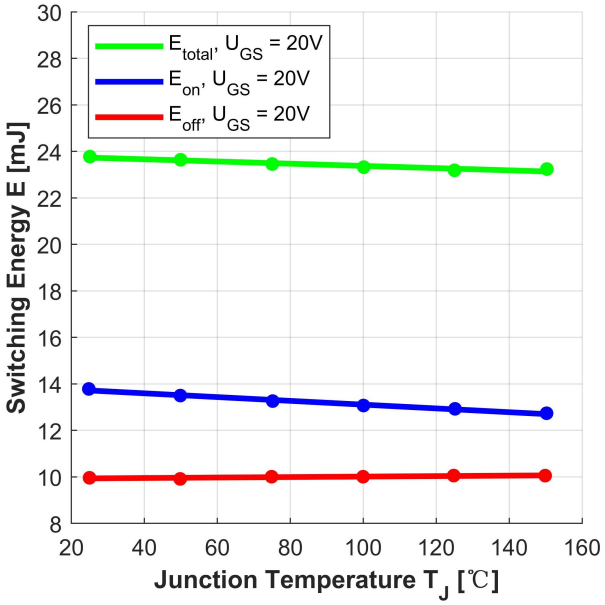

Figure 3.23: Turn-on/off and total switching energy vs junction temperature

The relationship between E_{on}/E_{off} and T_J can be modeled as two linear polynomials, as expressed as

$$\begin{cases} E_{on} = e_1 T_J + e_2 \\ E_{off} = f_1 T_J + f_2 \end{cases} \tag{3.11}$$

Finally, all the modeling coefficients related to the electrical characteristics of power SiC MOSFETs, as well as the corresponding testing conditions, are demonstrated in Table 3.6.

Table 3.6: Coefficients of Modeled Electrical Characteristics

Coefficient	1	2	3	4	Test conditions
a	-2.415·10^{-8}	3.363·10^{-5}	-4.69·10^{-3}	7.365	$T_J = 25°C$
b	-1.403·10^{-8}	2.104·10^{-4}	2.791·10^{-2}	6.963	$I_{DS} = 225A$
c	-8.984·10^{-4}	7.199·10^{-1}			$t_p = 200\mu s$
d	1.408·10^{-5}	1.773·10^{-3}			$t_p = 200\mu s$
e	-6.994·10^{-3}	13.96			$U_{DD} = 900V, I_{DS} = 300A$
f	1.02·10^{-3}	9.912			$U_{DD} = 900V, I_{DS} = 300A$

3.3.1.4 Design of Power MOSFETs in Parallel

In the constant torque region, the peak value of the input phase current when the motor generates maximum torque is $641.03A$, which far exceeds the maximum allowable DC continuous drain current I_D. Hence, the parallel operation method should be employed in the design of the inverter circuit arrangement. According to

(2.67) and assuming an initial junction temperature of $65°C$, the number of parallel SiC MOSFETs can be presented by

$$n = \frac{R_{DSon,max}(I - I_{max})}{R_{DSon,min} \cdot I_{max}} + 1 \tag{3.12}$$

$$\Rightarrow n = \frac{10 \cdot (641.03 - 270)}{6 \cdot 270} + 1 \approx 3.29$$

In general, if the impact of dynamic current sharing is disregarded, the number of parallel devices required exceeds 3. And with considering the actual junction temperature, which is expected to be higher than $65°C$ due to thermal conduction, the final number of branches is selected as 4.

3.4 Controller

The FOC introduced in this section primarily consists of two parts: a look-up table module for obtaining the reference currents and the corresponding dynamic parameters, and a current controller for generating the 3-phase reference voltages. The conceptual model of the controller is illustrated in Fig.3.24.

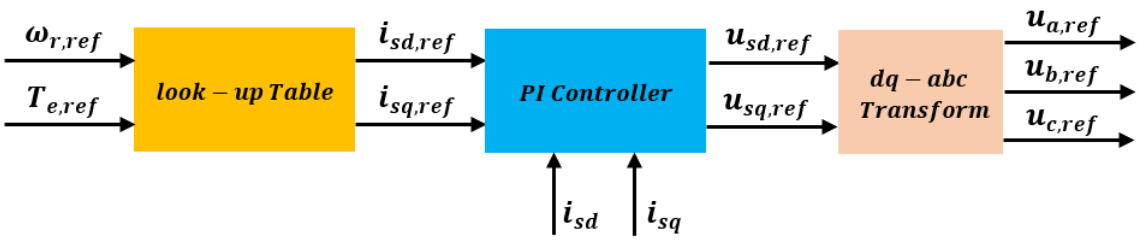

Figure 3.24: Conceptual diagram of FOC

3.4.1 Look-up Table

In contrast to the traditional speed controller, the current table-based control method is employed in this thesis[52], which is more conducive to obtain the reference dynamic parameters within a fixed control strategy and specific operating points.

As illustrated in Fig.3.25, once the reference motor speed ω_{ref} and torque T_{ref} within the operating range are given, the corresponding reference currents $i_{sd,ref}$ and $i_{sq,ref}$ can be determined based on 2D interpolation from the look-up tables. The same method can also be applied to obtain the reference stator inductance $\hat{L_{sd}}$ and $\hat{L_{sq}}$, as well as the magnetic flux linkage $\hat{\psi_m}$ from the reference currents.

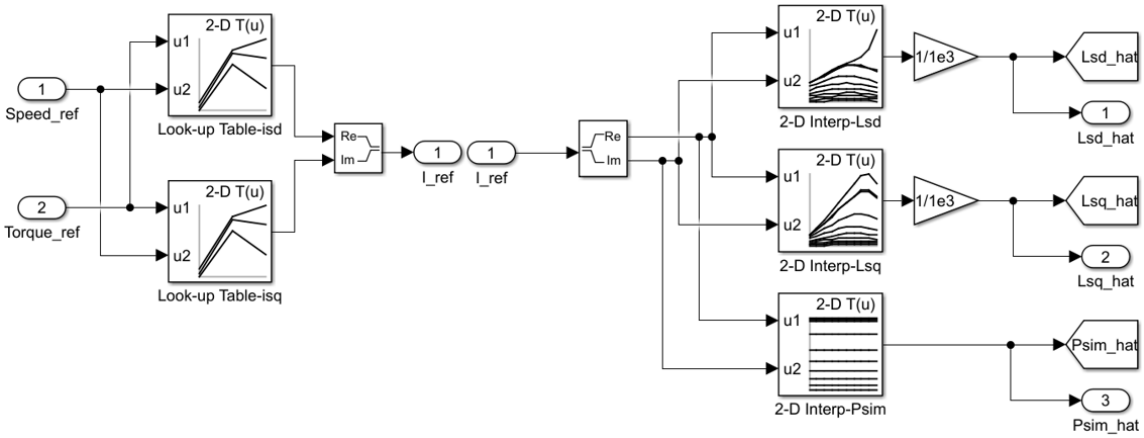

Figure 3.25: Look-up table for obtaining reference parameters in MATLAB

3.4.2 Current Controller

The two input types to the current controller are measured dq-currents from the IPMSM (i_{sd} and i_{sq}), and reference dq-currents ($i_{sd,ref}$ and $i_{sq,ref}$) obtained from the look-up table based on desired operating point. The current controller implemented in Simplorer is illustrated in Fig.3.26, primarily incorporating the three modules introduced in Section 2.4.

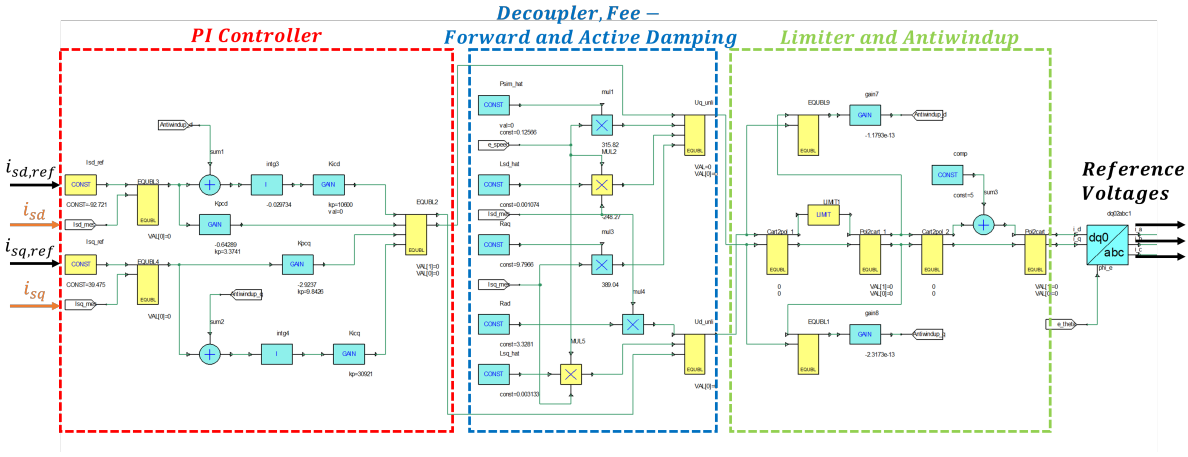

Figure 3.26: Current controller model in Simplorer

The error $\bar{e}$ between $i_{s,ref}$ and i_s is fed as input to the PI controller, which in turn determines the voltage u'_s across the winding resistance. Afterwards, the reference input voltage u_s is calculated, taking into account the decoupler, feed-forward, and active damping, and is subsequently limited by the voltage saturation. Finally, the limited dq-voltage is transformed into a 3-phase reference voltage signal which is fed to the SPWM module.

3.5 Power Losses of Entire Drive System

The energy efficiency of electric drive systems, particularly for vehicle applications, is a key focus, and achieving reduced system losses can be approached through different perspectives. In this research, the investigation of losses in the electric machine and inverter is performed under different switching frequencies. The losses in the motor are based on the quality of the current waveform. At lower switching frequencies due to large current ripples, the losses are higher, increasing the switching frequency can improve the quality of the current waveform and therefore reduce the losses. The losses in the inverter increase with the increase in switching frequency due to the energy loss for every switching cycle.

As shown in Fig.3.27, a decaying trend in the motor losses and linear behavior of the inverter losses with respect to switching frequency. For any given operating point on the torque-speed envelope, a minimum point of the total losses can be found.

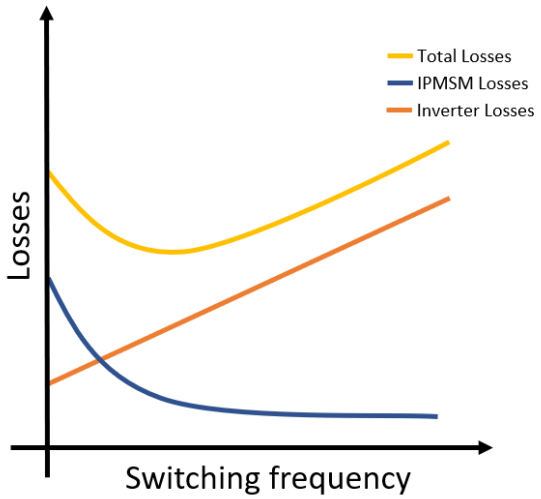

Figure 3.27: Generic behavior of motor, inverter, and total system losses

4

Methods

In this chapter, two main current vector control algorithms for the IPMSM will be extensively discussed based on their performance: the MTPA control strategy and the loss minimization control strategy. Subsequently, a comprehensive comparison will be made to determine the optimal motor control strategy. Furthermore, the junction temperature of MOSFETs and body diodes, along with the total power loss distribution at different switching frequencies, will be analyzed and presented.

4.1 Test Operating Speeds

The test speeds within the entire speed range are illustrated in Fig.4.1, serving as the reference for the following two control strategies. To ensure the testing accuracy, the speed range is set from 100 to 12000rpm with the gap not higher than 500rpm.

Test Speed [RPM]				
Const. T	*Const. P*			
100	2500	5200	8000	10800
500	3000	5600	8400	11200
1000	3200	6000	8800	11600
1500	3600	6400	9200	12000
2000	4000	6800	9600	
2322	4400	7200	10000	
	4800	7600	10400	

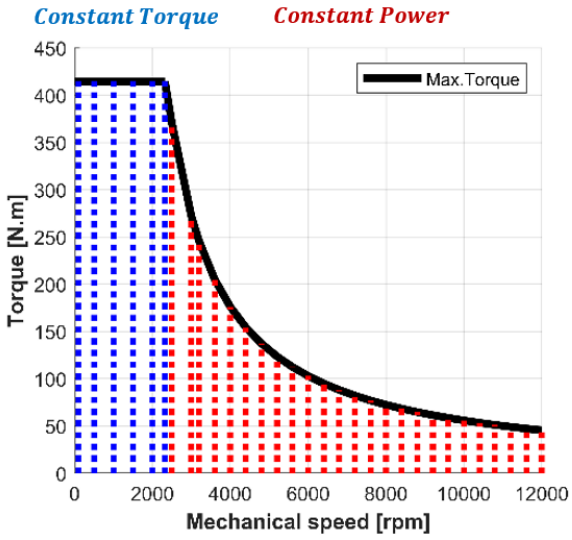

Figure 4.1: List of test operating speeds

4.2 Current Vector Control Strategies for IPMSM

4.2.1 MTPA Control Strategy

The purpose of MTPA control strategy is to achieve the optimal match between the input current and output torque of the motor, ensuring that the motor can generate

maximum electromagnetic torque with the minimum required input current.

According to (2.9), for SPMSM, the stator inductance in dq-direction is equal ($L_{sd} = L_{sq}$), which results in the reluctance torque T_R generated by motor equals to 0, meaning i_{sd} has no effect. Therefore, in order to improve magnet torque and current utilization as much as possible, the control strategy through setting i_{sd}=0 is selected to maximize i_{sq} under the same current amplitude. The output electromagnetic torque under this condition can be rewritten as

$$T_e = \frac{3n_p}{2}\psi_m i_{sq} \tag{4.1}$$

However, for the IPMSM drive system employed in this thesis, the impact of i_{sd} needs to be considered due to the generation of reluctance torque. In this regard, the MTPA control strategy can be adopted to determine the optimal electrical parameters to the IPMSM.

The MTPA control algorithm is primarily implemented using a nested loop structure, as shown in Fig.4.2. This involves analyzing each operating point to determine the optimal input current i_{sd}, i_{sq}.

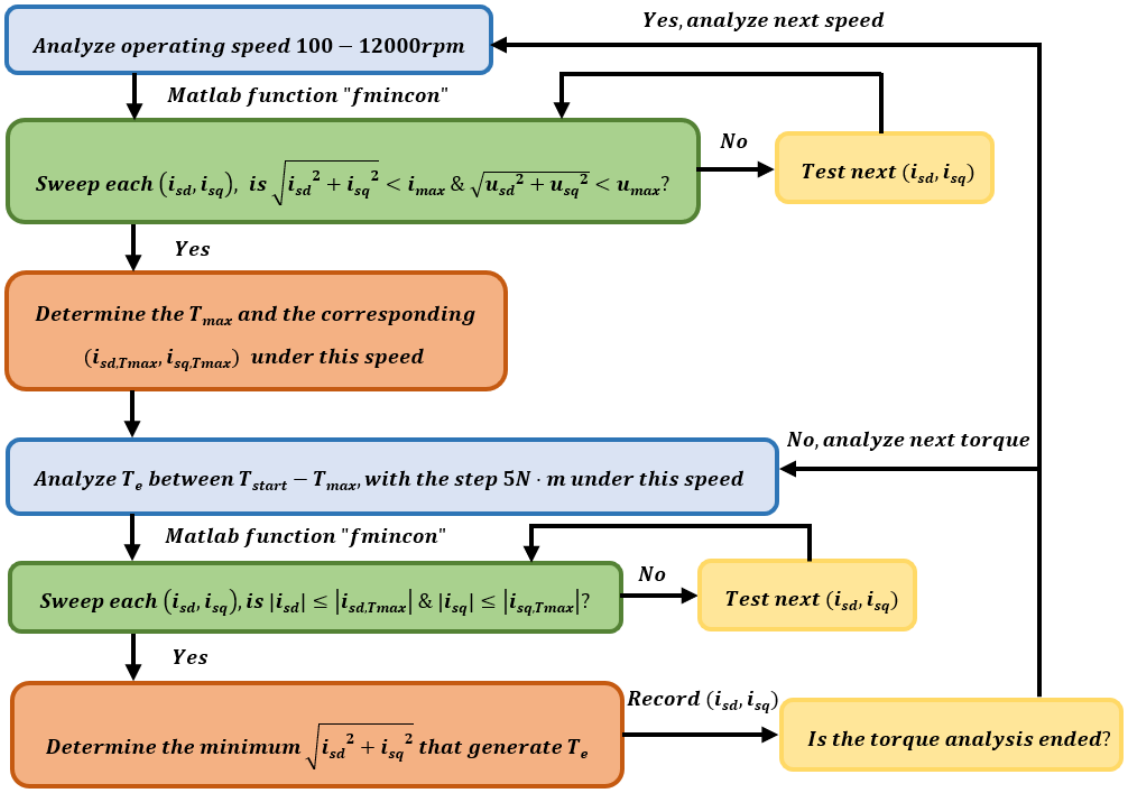

Figure 4.2: The process for MTPA control strategy

Based on the above process, the current trajectory under different operating speeds along with the maximum current limitation and output electromagnetic torque distribution is illustrated in Fig.4.3.

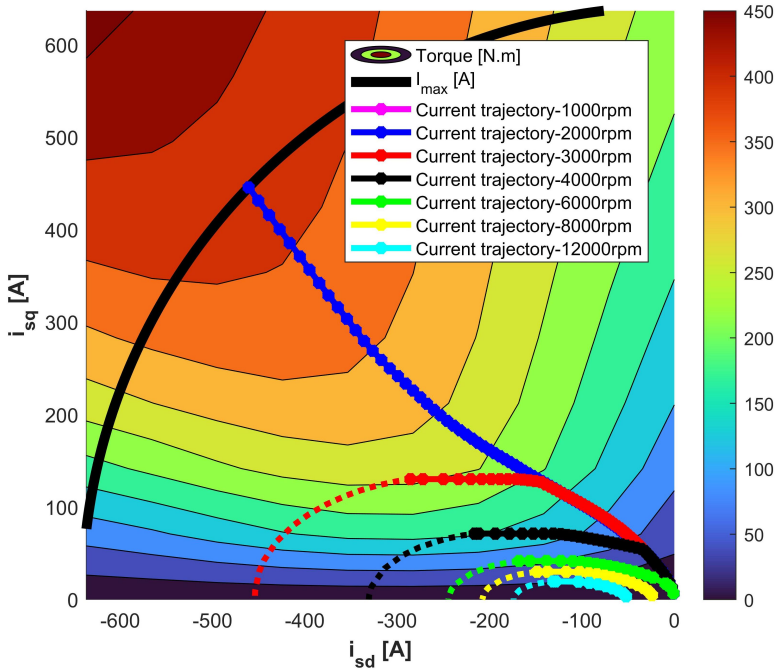

Figure 4.3: Current trajectories under different motor operating speed using MTPA control strategy

It is worth noting that the trajectory remains the same when the speed is below the rated speed, as shown by the pink ($1000rpm$) and blue ($2000rpm$) lines in the figure. However, if the speed continues to increase, the trajectory will shift along the voltage limit ellipse exceed a certain point. This can be clearly observed in the lines representing the speed 3000-6000rpm. Additionally, the yellow ($8000rpm$) and cyan ($12000rpm$) lines are completely limited by the maximum voltage and no longer originate from the coordinate origin. After transforming into the dashed current trajectory, the output torque under the corresponding speed will not continue to rise.

The distribution map of input current and voltage amplitudes across the entire operating region using the MTPA control strategy is illustrated in Fig.4.4. As the IPMSM operates in the constant torque region, it is apparent that the current remains constant even as the speed increases. This is because, in this region, the current trajectory is not limited by the voltage limit ellipse and continues to move towards the direction that can generate maximum torque. However, as the speed continues to rise and the motor enters the constant power region, the current trajectory begins to be affected by the maximum voltage constraint. Consequently, the torque generated by the same amplitude of input current gradually decreases.

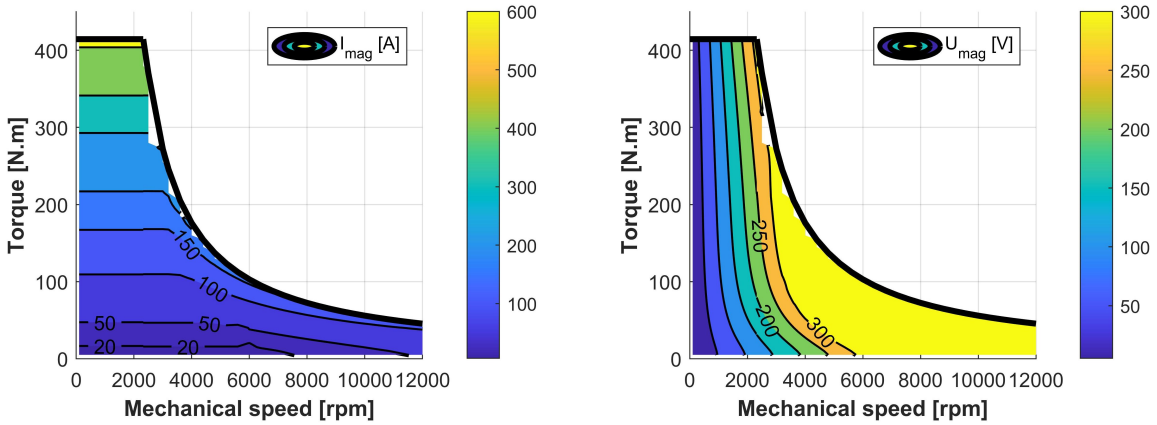

Figure 4.4: The input current (left) and voltage (right) distributions under the entire operating region using MTPA control strategy

Furthermore, it is observed that the stator voltage reaches its maximum value of $320V$ when the motor operating speed exceeds approximately $6000rpm$. This indicates that the current trajectory starts to become completely constrained by the maximum voltage at this speed.

As shown in Fig.4.5, the distribution of copper loss in each operating region under MTPA control follows a similar pattern to the current distribution due to their direct proportionality. The copper loss reaches its peak at around $24kW$ when the motor operates at low speeds (0-$2000rpm$) and generates high torque.

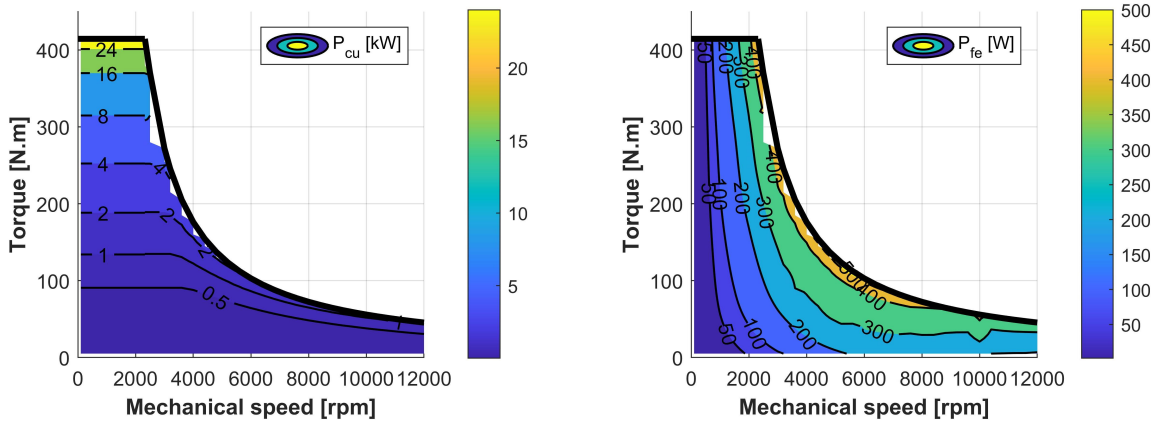

Figure 4.5: The copper loss (left) and iron loss (right) distribution under the entire operating region using MTPA control strategy

On the contrary, the iron loss reaches its peak at around $500W$ when the machine operates in the 4000-$6000rpm$ range. Moreover, in high-speed regions where the motor's output torque is low, it is often observed that the iron loss is comparable to the copper loss.

4.2.2 Loss Minimization Control Strategy

The loss minimization control algorithm is depicted in Fig.4.6. In contrast to the MTPA control, this strategy aims to find the input current combination that generates the torque T_e while minimizing total motor power losses, instead of solely focusing on achieving the minimum input current.

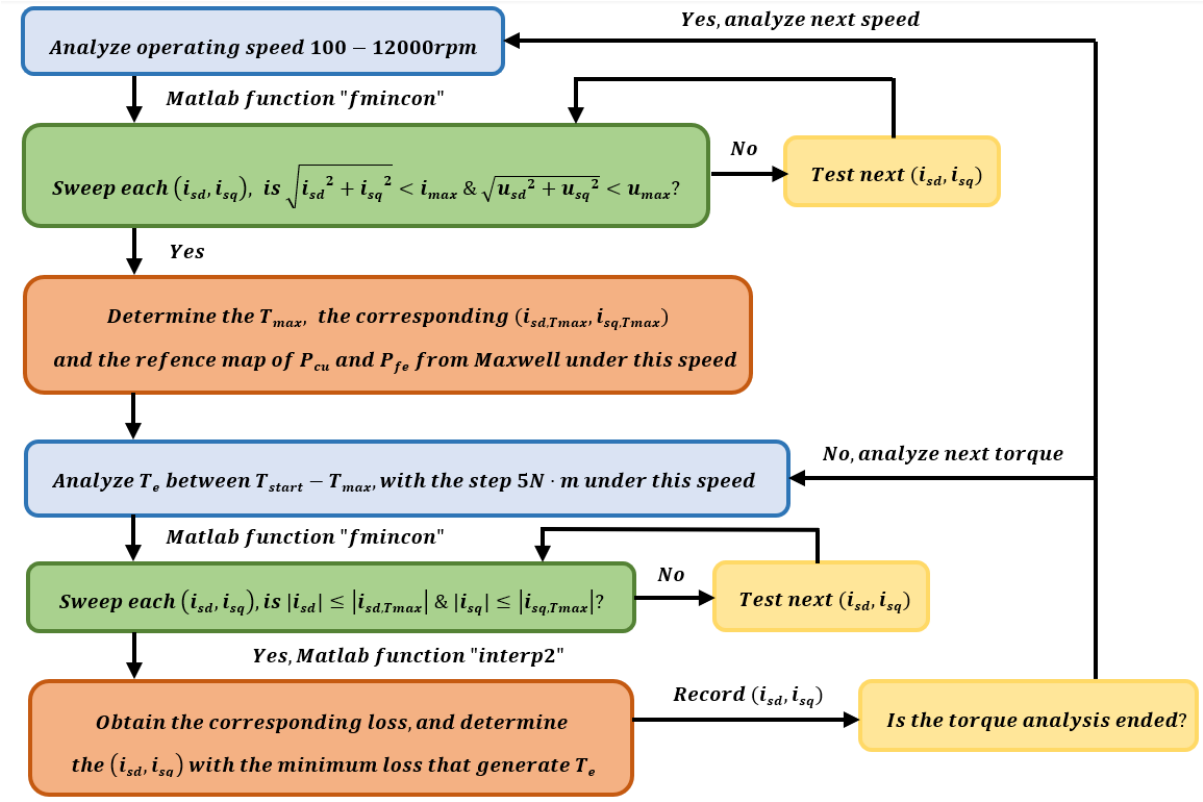

Figure 4.6: The process for loss minimization control strategy

The reference map of copper losses and iron losses is obtained from Maxwell, and adopting 2D interpolation, the various losses incurred at a specific input current can be determined. The small eddy current losses in the permanent magnet can be neglected since there is no ripple in the three-phase reference current input during the test.

Within the same testing speed range, Fig.4.7 displays the current trajectories under various motor operating speeds for the loss minimization control strategy.

Compared with MTPA control strategy, a noticeable difference is that when the motor operates below the rated speed, the trajectories are no longer the same due to variations in the iron loss. In addition, minor changes are observed in other trajectories within the speed range of 3000-12000rpm. This occurs because the direction of the trajectory is now guided by minimizing motor power losses instead of minimizing current magnitude.

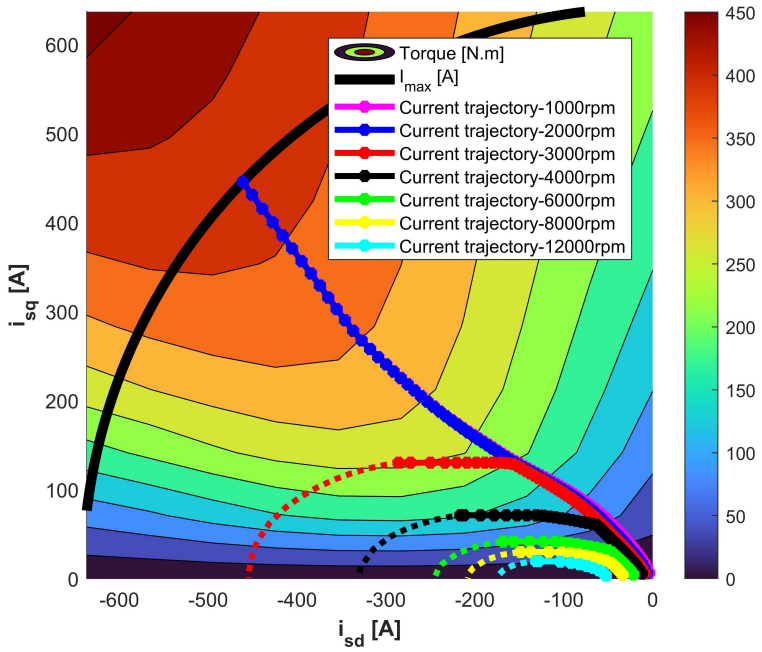

Figure 4.7: Current trajectories under different motor operating speed using loss minimization control strategy

As illustrated in Fig.4.8, the distribution of input current and voltage amplitude across entire operating regions using the loss minimization control strategy differs from that observed using the MTPA control strategy. In the constant torque region, the current distribution is no longer uniform, and a higher current magnitude is required to generate the same torque as the speed increases.

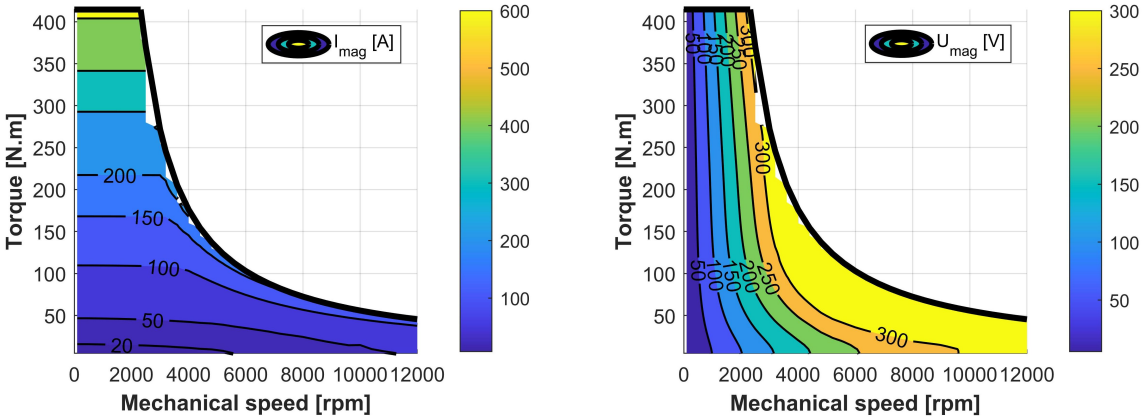

Figure 4.8: The current (left) and voltage (right) distributions under entire operating regions using loss minimization control strategy

The corresponding distributions of power losses are shown in Fig.4.9. Similarly, the maximum value of copper loss and iron loss that can be achieved in the constant torque region and medium-speed regions are also close to $24kW$ and $500W$, respectively.

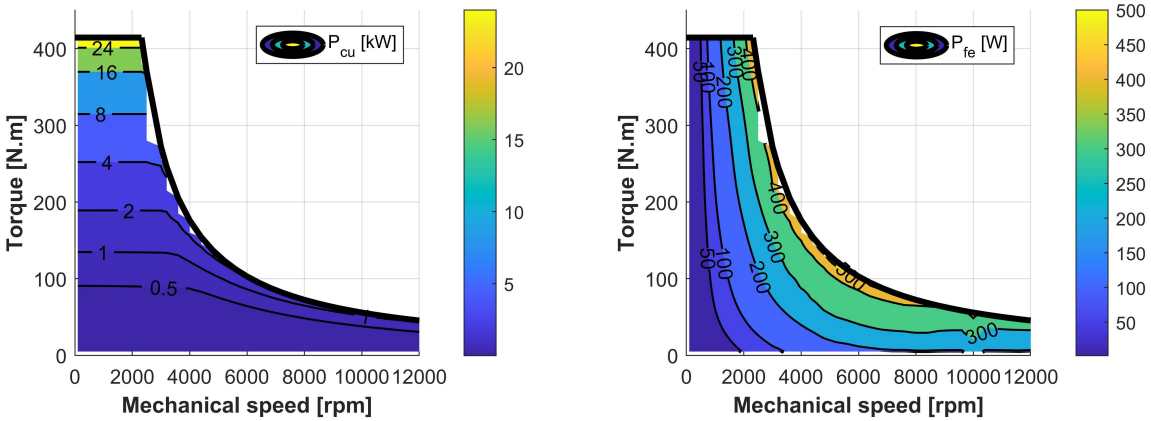

Figure 4.9: The copper loss (left) and iron loss (right) distribution under entire operating region using loss minimization control strategy

4.2.3 Comparison Between Different Control Strategies

The MTPA and loss minimization control strategies will be comprehensively compared in terms of energy efficiency, reference input current, and feasibility. Based on this comparison, the optimal control strategy will be selected for the power loss analysis of the entire electric drive system.

4.2.3.1 Comparison of Energy Efficiency in IPMSM

The distribution of total power losses in IPMSM when utilizing different control strategies are illustrated in Fig.4.10, which combines both copper losses and iron losses. In general, as the motor operating speed rises while maintaining the same output torque, the total motor power loss also increases.

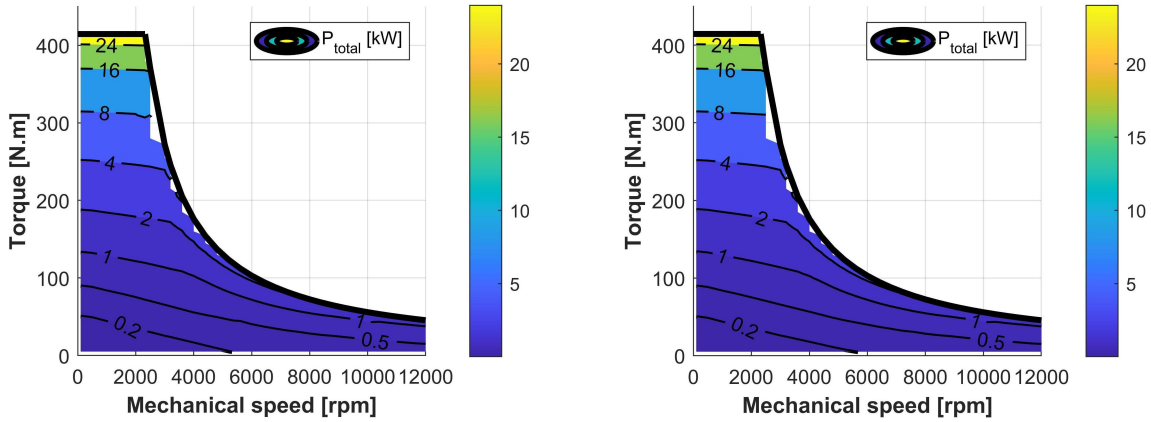

Figure 4.10: Total loss distribution under entire operating region using MTPA (left) and loss minimization (right) control strategies

The energy efficiency of IPMSM under these two control strategies can be calculated based on (2.24). As the efficiency distribution map shown in Fig.4.11, the most

significant difference between them is roughly located at the highest efficiency (98%) area. In contrast, the distributions in other regions are nearly identical.

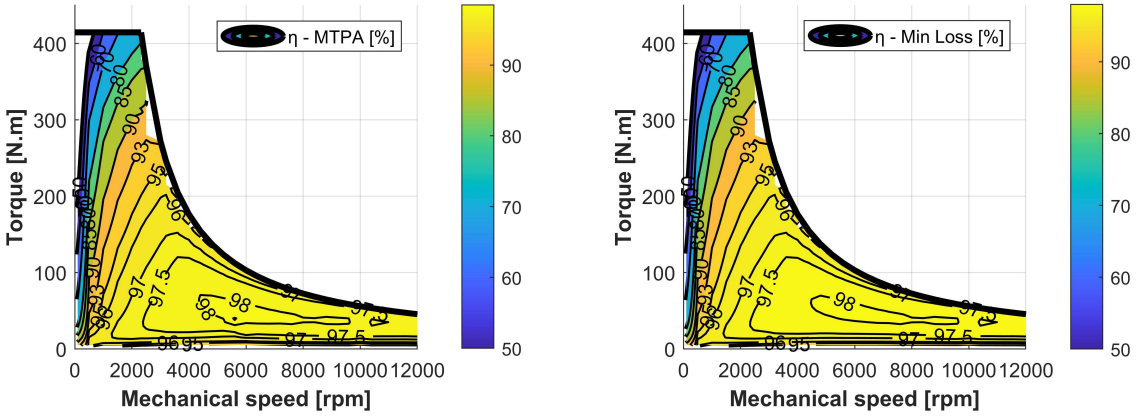

Figure 4.11: Energy efficiency distribution under entire operating region using MTPA (left) and loss minimization (right) control strategies

The difference of motor power losses and energy efficiency between various control strategies can be expressed by

$$\begin{cases} \Delta P_{total} = P_{MTPA} - P_{LossMin} \\ \Delta \eta_e = \eta_{LossMin} - \eta_{MTPA} \end{cases} \tag{4.2}$$

where P_{MTPA}/η_{MTPA} and $P_{LossMin}/\eta_{LossMin}$ represent the motor power losses/energy efficiency under MTPA and loss minimization control strategies, separately. The corresponding difference distributions are indicated in Fig.4.12.

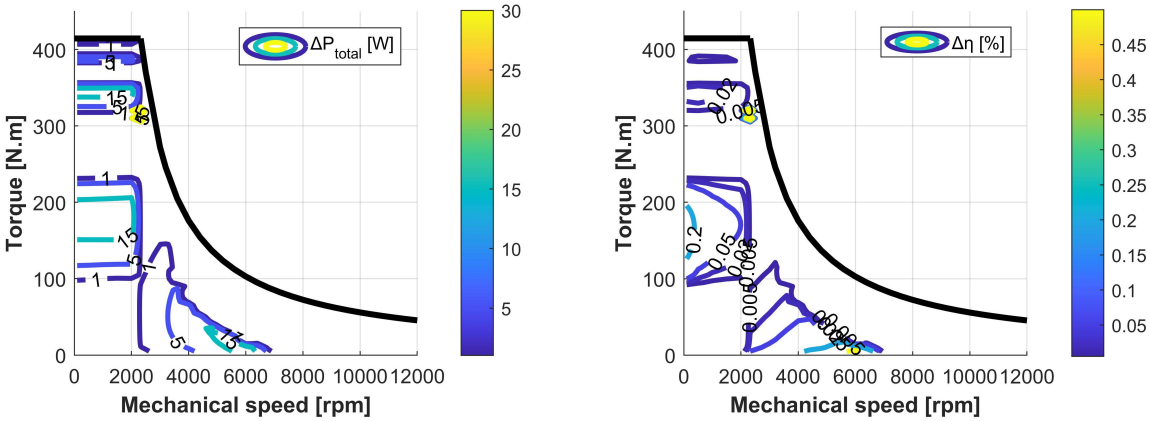

Figure 4.12: Difference distribution of motor energy efficiency (left) and power loss (right) between different control strategies

When adopting loss minimization control strategy, the energy efficiency in most operating regions is higher than when using MTPA control strategy, especially in medium-speed regions generating low torque (0-50$N{\cdot}m$) and the constant torque region with torque between 100-400$N{\cdot}m$. However, overall, the energy efficiency raise

brought by this control strategy is not significant in the remaining operating regions.

To better reveal this phenomenon, Fig.4.13 illustrates the variation trend of motor efficiency and losses under the two control strategies at specific operating speeds.

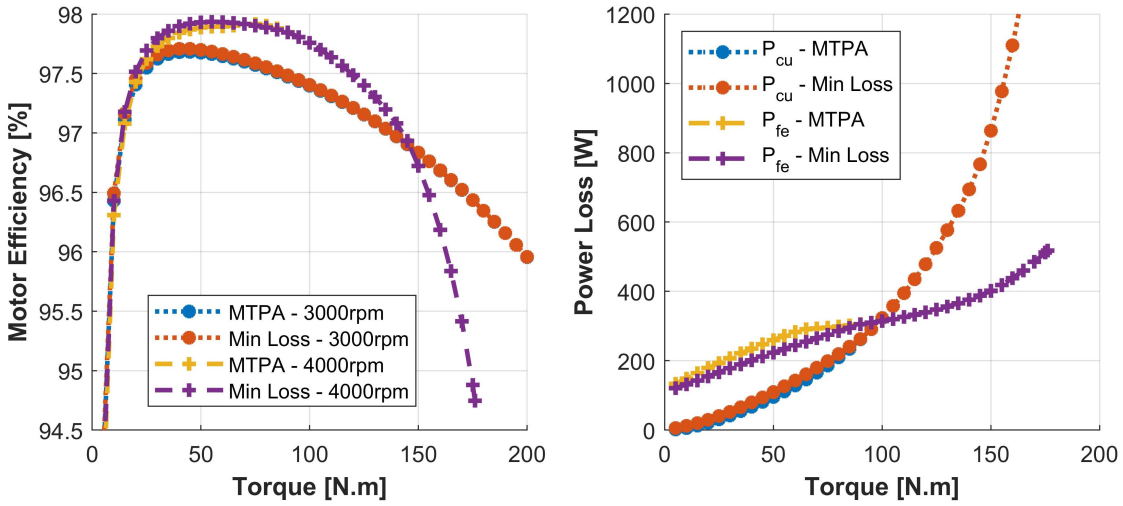

Figure 4.13: The comparison of motor energy efficiency at 3000 and 4000rpm (left) and the comparison of motor power losses at 4000rpm (right) between the two control strategies.

Starting at the output torque of 5$N{\cdot}m$ at the speed of 3000rpm and 4000rpm, it is noticeable that the loss minimization control strategy can improve the motor energy efficiency to a certain extent. However, this improvement gradually becomes less evident as the output torque increases. After reaching output torques of 150$N{\cdot}m$ and 90$N{\cdot}m$ at the two respective speeds, the motor efficiency under both control strategies becomes nearly identical.

Furthermore, the increase in output torque is attributed to the rise in input current, which also leads to a quadratic increase in copper losses. However, the iron losses increases at a slower rate, causing its proportion to the total losses to diminish as the output torque increases. As a result, under the same amplitude of stator current, the motor losses become nearly identical. Therefore, the loss minimization control begins to nearly transform into MTPA control at the same time.

4.2.3.2 Comparison of Input Current in IPMSM

The distribution of i_{sd} and i_{sq} under two control strategies are shown in Fig.4.14 and Fig.4.15, respectively. As mentioned before, during MTPA control, the input current used to generate the same torque at the constant torque region is evenly distributed, as it is within the limit range of the maximum voltage. However, due to the control strategy no longer tend to seek the minimum current, the current distribution in the same area is no longer uniform in loss minimization control, especially in low torque regions.

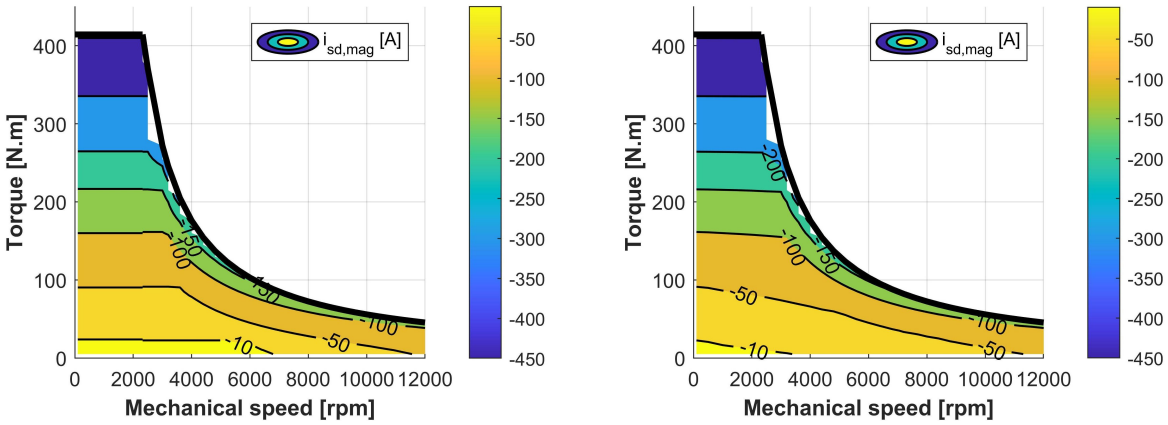

Figure 4.14: The d-current distribution under entire operating region using MTPA (left) and loss minimization (right) control strategies

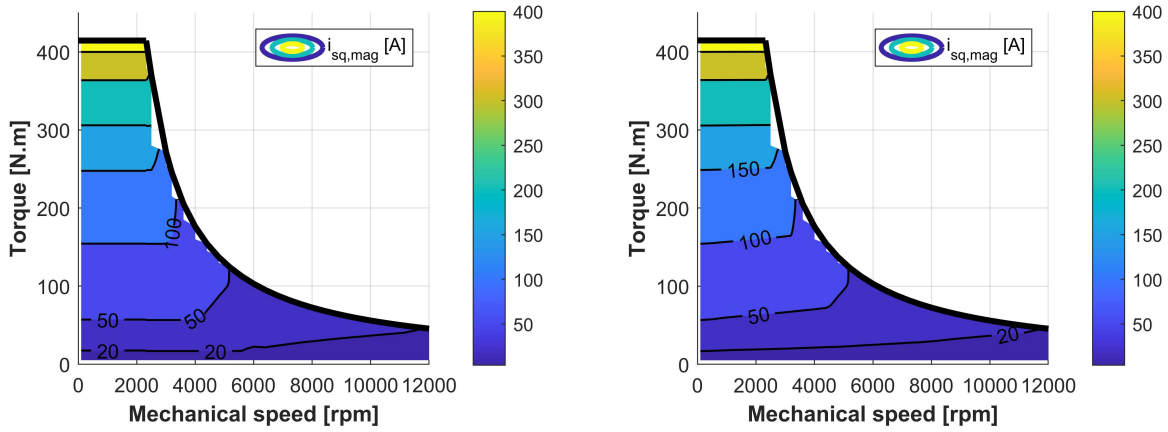

Figure 4.15: The q-current distribution under entire operating region using MTPA (left) and loss minimization (right) control strategies

It is self-evident that when the output torque is less than a specific value, the i_{sq} required for MTPA control is slightly greater than that for loss minimization control. On the contrary, it consumes significantly less magnitude of i_{sd}. This feature is well reflected in Fig.4.16 at the test speed of $6000rpm$. Overall, compared with loss minimization control, the motor consistently requires less input current when using MTPA control at the same operating point.

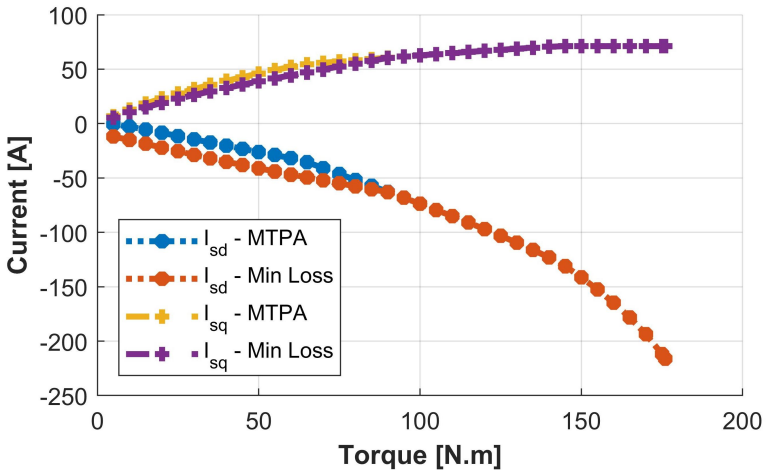

Figure 4.16: The comparison of input i_{sd} and i_{sq} at $6000rpm$ between the two control strategies

4.2.3.3 Feasibility Analysis

In the majority of working regions, especially when the motor generate high output torque, the energy efficiency improvement brought by the loss minimization control strategy will not exceed 0.01%. This phenomena can be represented in Table.4.1, which shows the error in input current and energy efficiency at two operating speeds.

Table 4.1: Comparison of input current and motor energy efficiency between MTPA and loss minimization control strategy at different operating points

Speed$[rpm]$	Torque$[N{\cdot}m]$	Para.	MTPA	Loss Min.	Error
3000	25	i_s	29.97 A	32.32 A	7.84 %
		η	97.55 %	97.59 %	0.04 %
3000	50	i_s	52.86 A	57.79 A	9.33 %
		η	97.68 %	97.70 %	0.02 %
3000	75	i_s	72.99 A	74.53 A	2.11%
		η	97.57 %	97.59 %	0.01%
3000	100	i_s	92.44 A	93.56 A	1.21%
		η	97.40 %	97.41 %	0.007%
4000	25	i_s	29.97 A	34.20 A	14.11%
		η	97.62 %	97.69 %	0.08%
4000	50	i_s	52.86 A	56.45 A	6.69%
		η	97.89 %	97.93 %	0.05%
4000	75	i_s	73.54 A	75.99 A	3.33%
		η	97.90 %	97.91 %	0.01%
4000	100	i_s	96.82 A	96.82 A	0%
		η	97.76 %	97.76 %	0%

It is apparent that at these two speeds, when the motor efficiency visibly improves,

the value of input current consumption also increases. Similarly, when the input current declines, the efficiency improvement decreases accordingly. Thus, compared to MTPA control, introducing the minimum loss control has little significance.

During the process of IPMSM control, the eddy current loss in PMs and iron loss are typically influenced to some extent by the inverter switching frequency, leading to the unpredictability of the total power losses of motor. As a result, achieving the loss minimization control based on a given total loss distribution becomes challenging. Moreover, this control strategy also neglects the impact of inverter losses, which makes it difficult to accurately minimize the losses of the entire drive system.

Overall, the MTPA control strategy proves to be effective in utilizing the minimum current to generate maximum torque while ensuring high energy efficiency. Therefore, it can be considered a suitable control strategy for the entire drive system.

4.3 Efficiency Analysis for Inverter Circuit

As stated in Section 3.3, the junction temperature T_J of power inverters is initially set at $65°C$, which corresponds to temperature of the coolant or heatsink. Additionally, the power losses P_{loss} are assumed to be obtained based on the maximum allowable temperature $150°C$. To refine the calculations and obtain accurate data for T_J and P_{loss}, the thermal conduction process (2.65) is used to recalculate T_J iteratively several times until convergence is achieved.

By employing the MTPA control strategy, when the motor is running at $3000rpm$, two operating points are provided as examples, with output torques of $100N{\cdot}m$ and $250N{\cdot}m$ respectively. As shown in Fig.4.17, with a switching frequency of $10kHz$, the junction temperature and total power losses of MOSFETs and body diodes stabilize around certain values after 5 iterations.

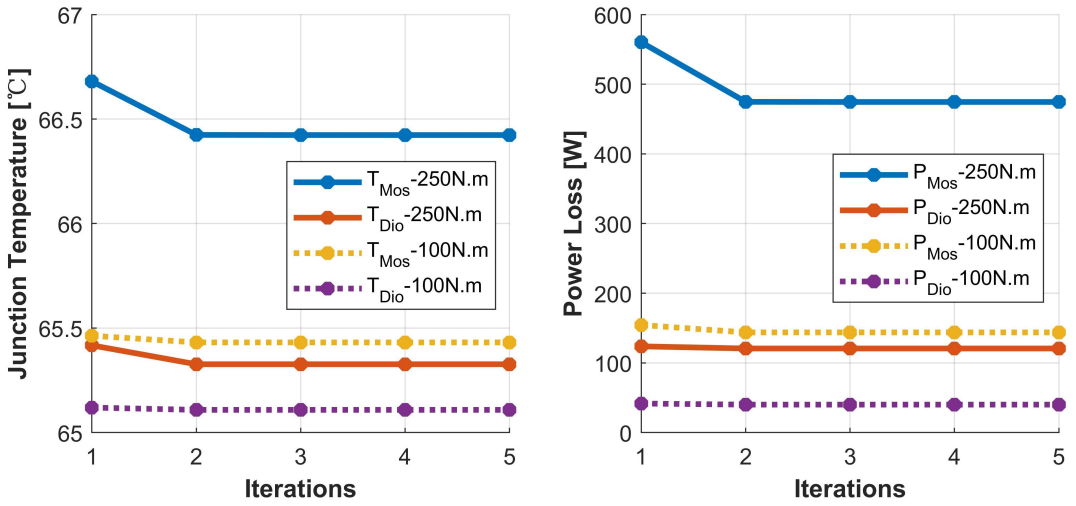

Figure 4.17: Iterations of junction temperature (left) and total power losses (right) at $3000rpm$ in MOSFETs and body diodes

4.3.1 Junction Temperatures

Indeed, after each round of iterations, the respective junction temperatures and power losses decrease to varying degrees, as the simulated junction temperature after each iteration remains higher than the actual one. After 5 iterations, Fig.4.18 provides an overview of the junction temperature distribution across the entire operating region for each MOSFET and diode.

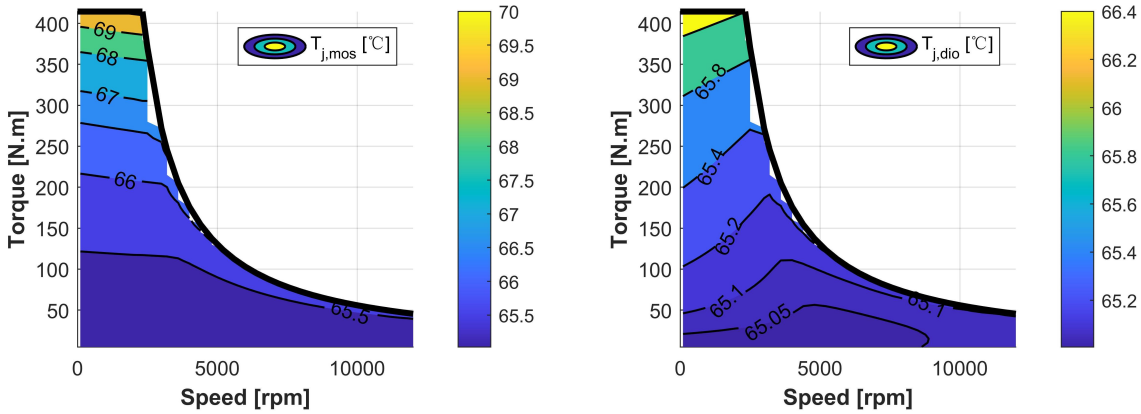

Figure 4.18: The junction temperature distribution of MOSFET (left) and body diode (right) under entire operation region with the switching frequency of $10kHz$

Among these strategies, the maximum junction temperature that each MOSFET and diode can reach is around $70°C$ and $66.5°C$ respectively. Both of these temperatures are observed within the operating range of the maximum input current.

4.3.2 Inverter Power Losses

The distribution of IPMSM's power factor $cos\psi$ and modulation index M_a are shown in Fig.4.19, which are crucial for calculating inverter power losses. The value ranges of them are mainly between 0.4-0.95 for $cos\psi$ and 0.1-0.8 for M_a.

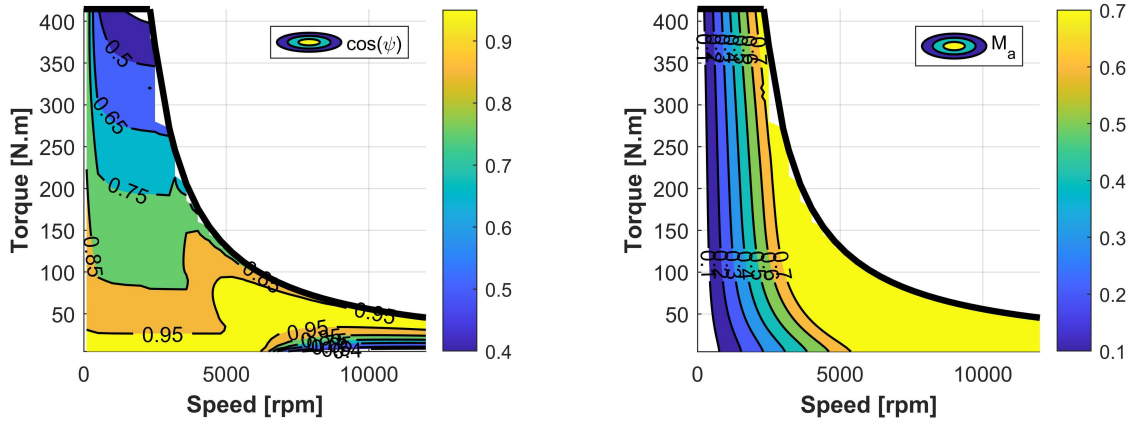

Figure 4.19: The distribution of power factor (left) and modulation index (right) under entire operating region

In automotive traction inverters, the switching frequency typically remains below $10kHz$[53]. To investigate the power losses distribution, four different switching frequency values are utilized in the inverter circuit: $2.5kHz$, $5kHz$, $7.5kHz$ and $10kHz$.

When integrating the IPMSM with the 3-phase inverter circuit introduced in Chapter 3 and applying the MTPA control strategy, the distribution of various types of inverter losses, along with the total inverter losses across different f_{sw} values are illustrated in Fig.4.20.

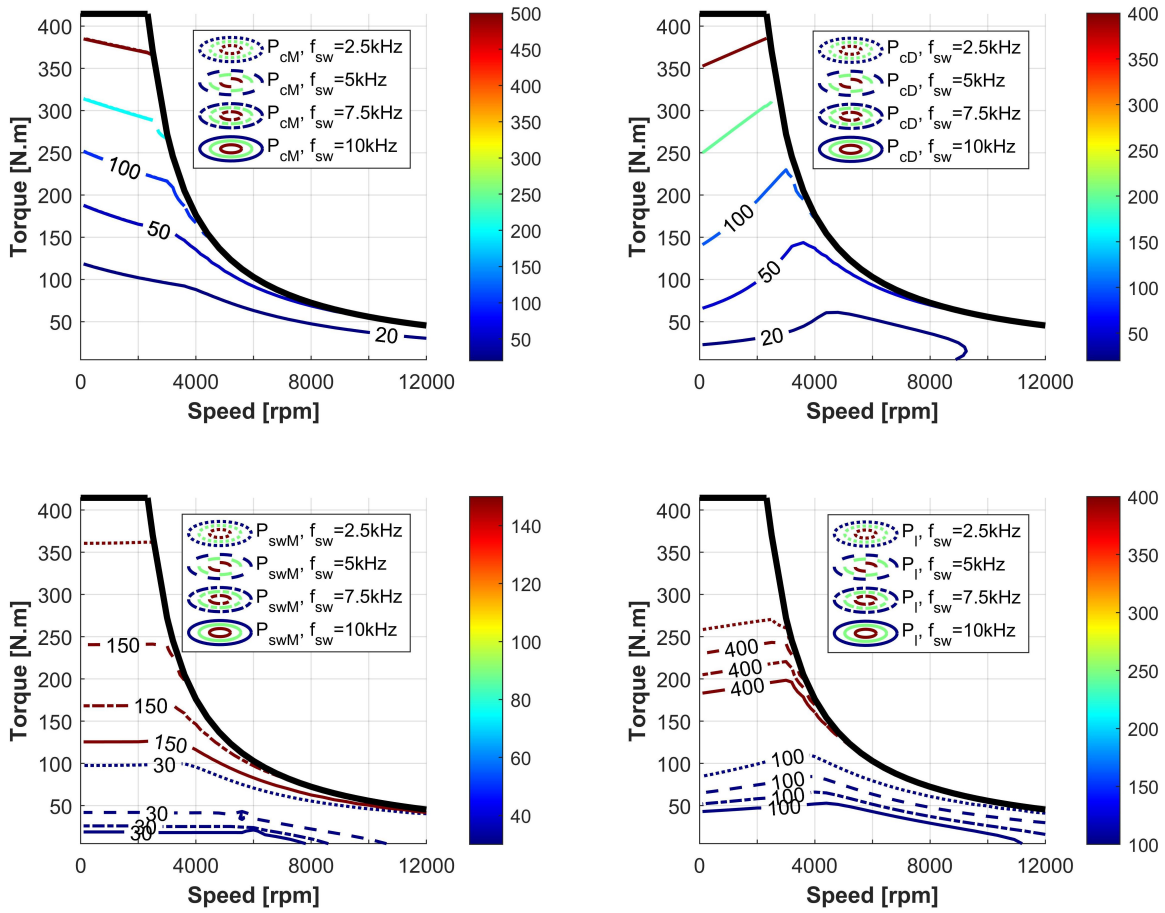

Figure 4.20: The distribution of conduction loss in MOSFETs (upper left), conduction loss in body diodes (upper right), switching loss in MOSFETs (lower left) and total inverter power losses (lower right) across the switching frequencies of $2.5kHz$, $5kHz$, $7.5kHz$ and $10kHz$ under entire operating regions

Obviously, for a fixed operating point, when the f_{sw} value is selected as the lowest, both of the switching loss and the total losses are minimized. Although this trend also holds for conduction loss in MOSFETs and diodes, their variation between different f_{sw} values is generally limited to within $10W$, making it less prominent and not well represented in the figure. This occurs because, the switching loss shows an almost linearly proportional relationship with the f_{sw} value, whereas the increase in conduction losses is primarily attributed to the rise in T_J caused by the higher switching frequency.

When f_{sw} is $10kHz$, as depicted in Fig.4.21, the switching loss are the primary contributor to the total power loss in the low load region, whereas conduction loss dominate in other operating regions. Furthermore, the power loss in MOSFETs consistently constitute more than half of the total power loss and are most significant in the high-speed region.

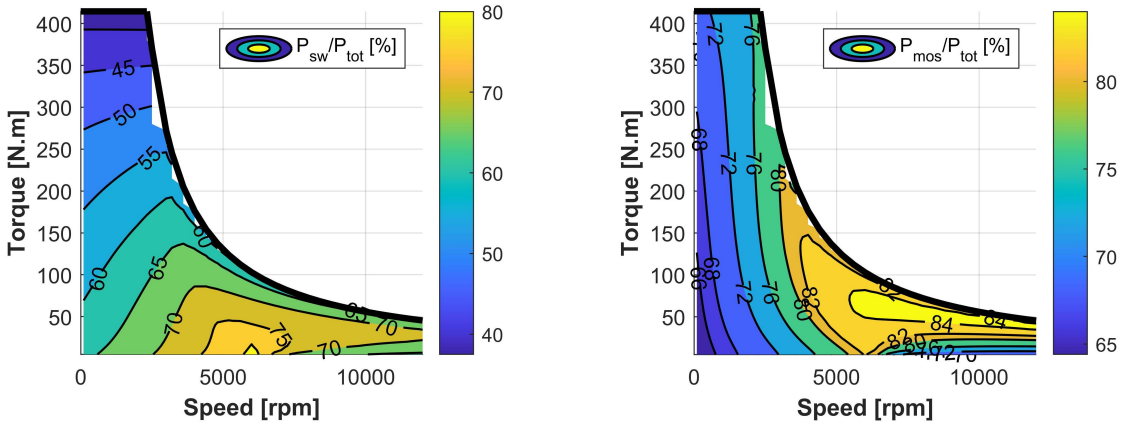

Figure 4.21: The distribution of switching losses and MOSFET losses as a percentage of the total power losses in the inverter circuit

In the next chapter, an exploration of several different f_{sw} values will be investigated at each operating point, and a detailed analysis of the inverter power losses distribution will be conducted for the specific case.

5

Results & Discussions

In this chapter, based on the previously introduced model and methods, the impact of different switching frequencies on the drive system will be thoroughly examined. Afterwards, a comprehensive discussion of the optimal switching scheme across the entire operating region of the IPMSM will be presented.

5.1 Power Losses Analysis of Entire Drive System

The following section will provide a power loss analysis for the IPMSM and the power SiC inverter circuit at two different operating points. One operating point will be from the low-speed region, and the other from the high-speed region.

5.1.1 Power Losses in IPMSM

The injected 3-phase currents of IPMSM when operating at $3000rpm$ and $6000rpm$ is illustated in Fig.5.1 and Fig.5.2, which generates an electromagnetic torque of $200N{\cdot}m$ and $50N{\cdot}m$, respectively.

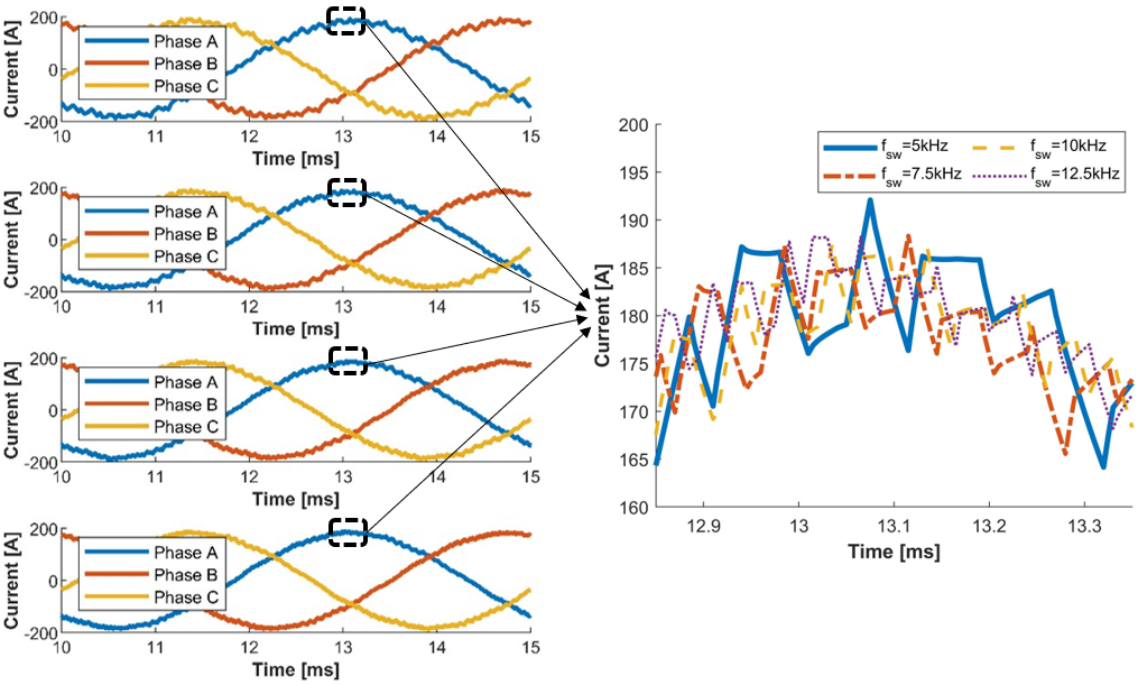

Figure 5.1: The 3-phase currents injected to IPMSM at $3000rpm$, $200N{\cdot}m$

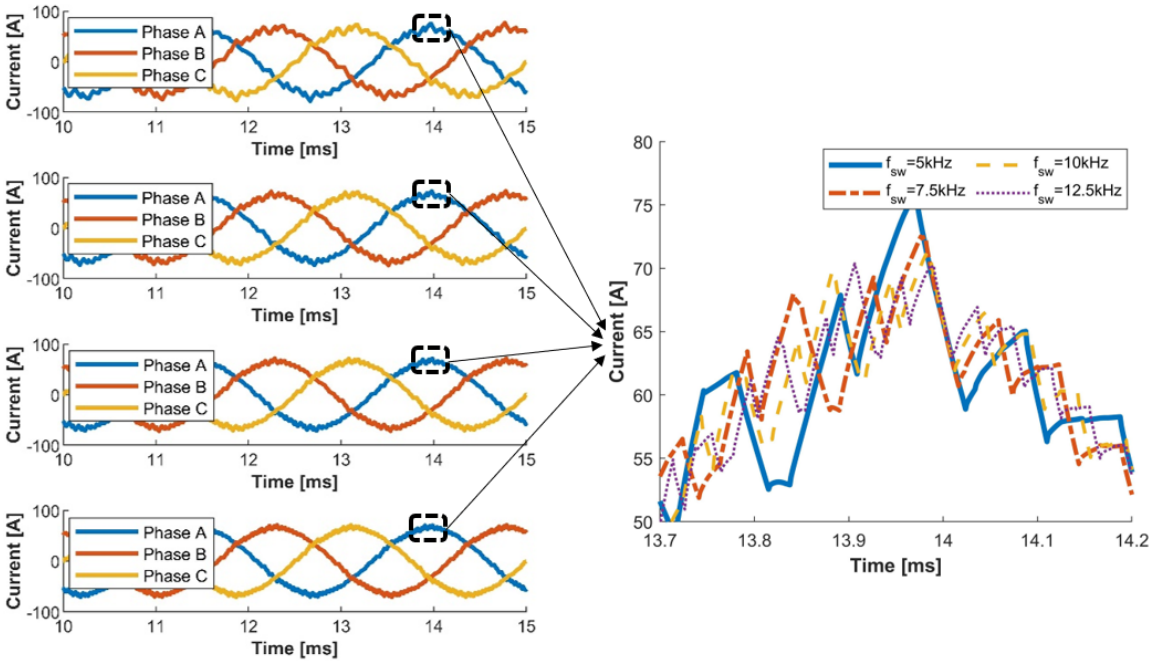

Figure 5.2: The 3-phase currents injected to IPMSM at $6000rpm$, $50N{\cdot}m$

The testing covered a range of f_{sw} values from 5-12.5kHz, with intervals of 2.5kHz. In the figures, the generated three-phase currents under these different f_{sw} values from the inverter circuit are arranged from top to bottom. The corresponding FFT of these currents, depicted in Fig.5.3, the switching frequency components of these currents account for the losses, and as the switching frequency increases, these coefficients are suppressed making the waveform close to pure sinusoidal.

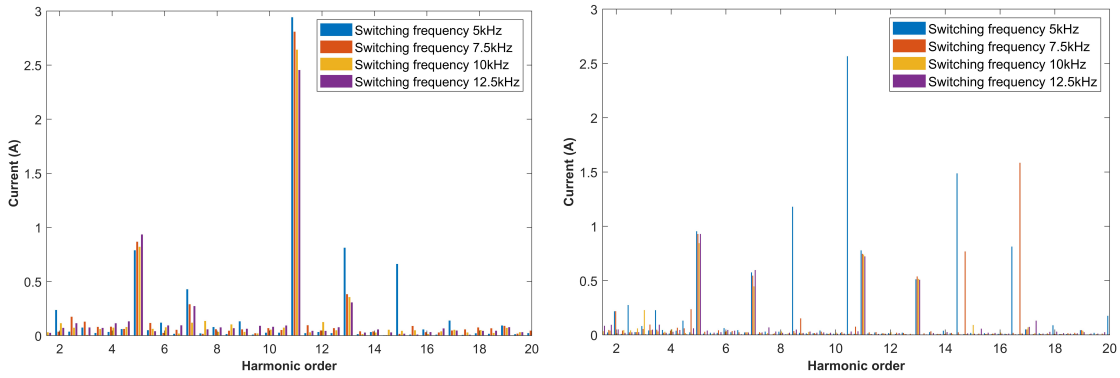

Figure 5.3: FFT of the current waveform at $3000rpm$, $200N{\cdot}m$ (left) and $6000rpm$, $50N{\cdot}m$ (right)

Fig.5.4 shows the output torque of the IPMSM. The torque ripple decreases with the rise in switching frequency. It can be seen clearly in Fig.5.5 that the torque harmonics are of the order 6, 12, and 18 with the $12th$ being the most significant. The lower-order harmonics are reduced with the increase in switching frequency.

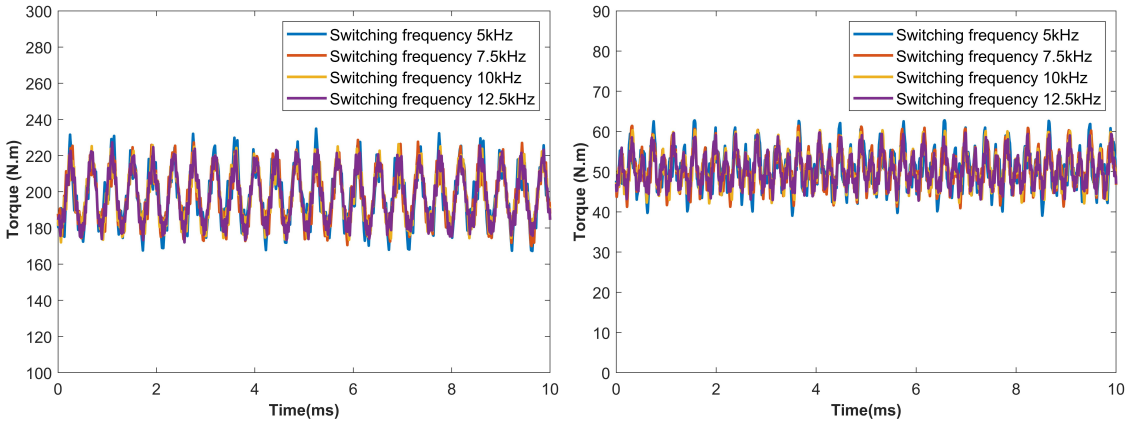

Figure 5.4: Output torque at $3000rpm$, $200N{\cdot}m$ (left) and $6000rpm$, $50N{\cdot}m$ (right)

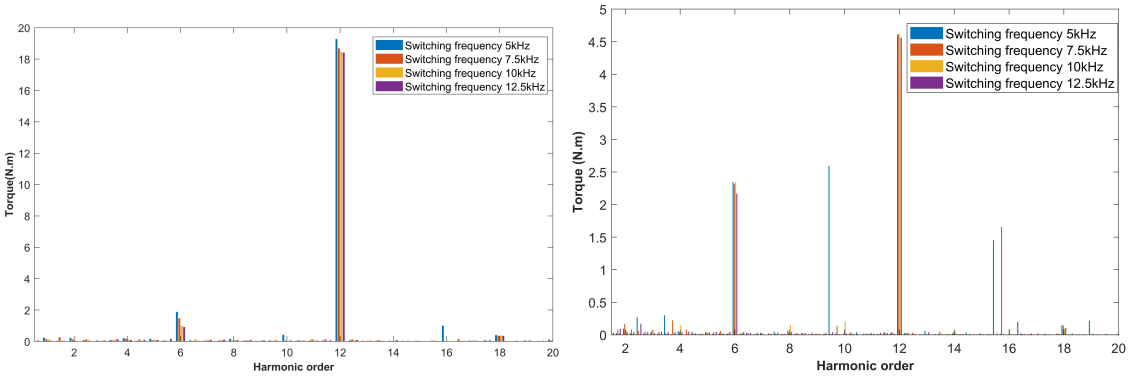

Figure 5.5: FFT of the output torque waveform at $3000rpm$, $200N{\cdot}m$ (left) and $6000rpm$, $50N{\cdot}m$ (right)

As shown in Fig.5.6, the corresponding power losses in IPMSM under the tested f_{sw} values are divided into three parts: copper loss, iron loss, and magnet eddy current loss. These components are visualized in individual columns with different colors.

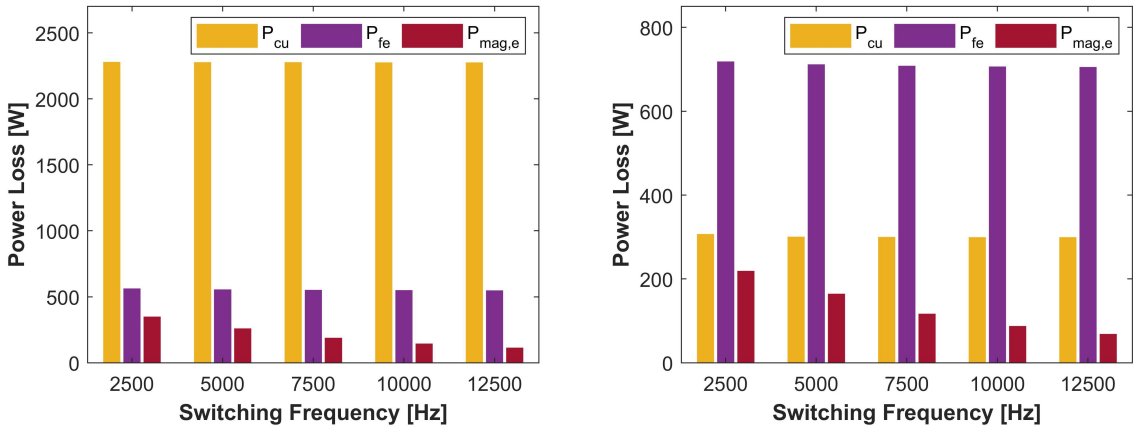

Figure 5.6: The power losses in IPMSM at $3000rpm$, $200N{\cdot}m$ (left) and $6000rpm$, $50N{\cdot}m$ (right)

As the switching frequency increase from $2.5kHz$, there is a significant drop in magnet eddy current loss in both operating points, which is attributed to the decrease of the current ripples brought by higher f_{sw} values. However, although the decrease in iron loss is also influenced by the same reason, it is much less obvious, with the overall drop from 2.5-12.5kHz being lower than $20W$ at both operating points. Moreover, the magnitude of the copper loss remains almost independent of the switching frequency, because of the fixed value of the winding material resistance.

5.1.2 Power Losses in Inverter Circuit

The induced 3-phase voltages generated by SPWM control through the inverter circuit at these operating points are displayed in Fig.5.7, which also reflect the specific waveform of the input PWM signals. The tested f_{sw} values are still shown from top to bottom, ranging from 5-12.5kHz. Similarly, when the switching frequency is higher than $10kHz$, the improvement in the induced voltage waveform by the inverter circuit system becomes less evident.

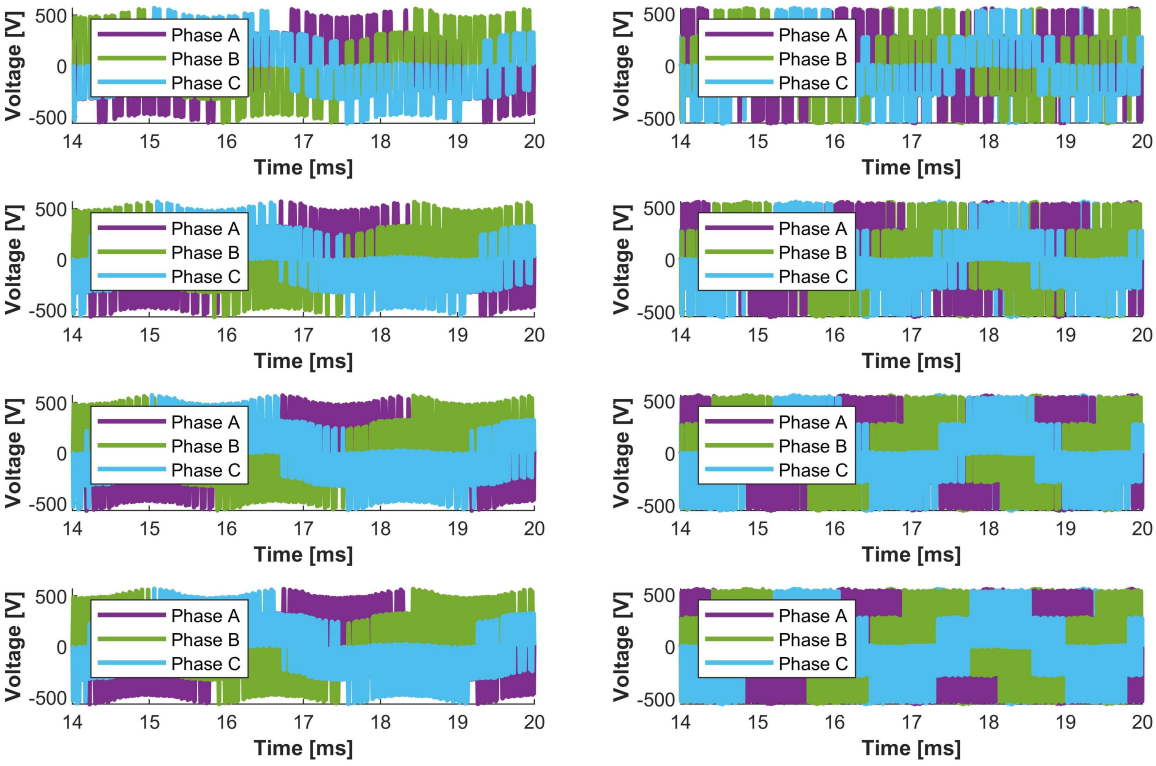

Figure 5.7: The 3-phase induced voltages generated in the inverter circuit at 3000rpm, 200$N{\cdot}m$ (left) and 6000rpm, 50$N{\cdot}m$ (right)

Fig.5.8, shows the FFT of the voltages at 3000rpm and 200$N{\cdot}m$. The lower order harmonics remain almost the same regardless of the switching frequency.

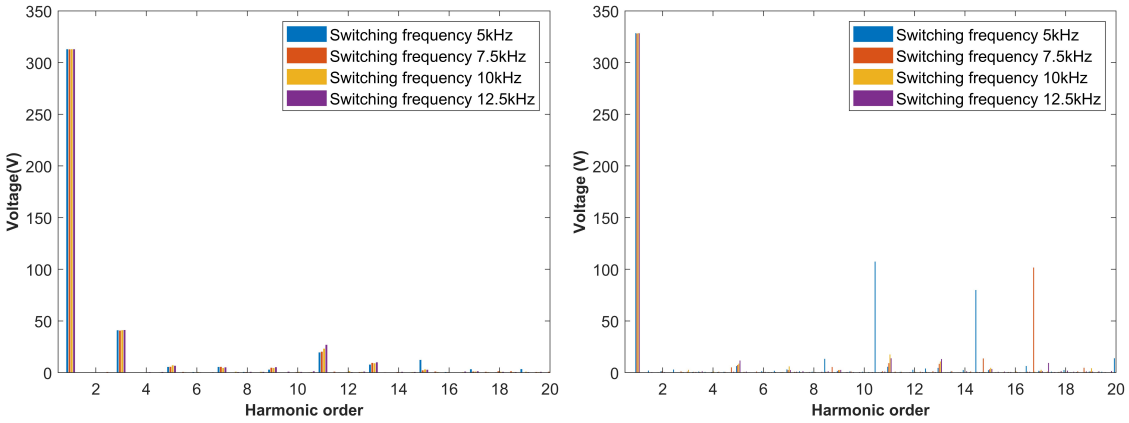

Figure 5.8: FFT of the voltage waveform at 3000rpm, 200$N{\cdot}m$ (left) and 6000rpm, 50$N{\cdot}m$ (right)

Table 5.1: Results for Both Cases (3000rpm, 200$N{\cdot}m$ and 8000rpm, 50$N{\cdot}m$)

Operating point	**Parameter**	**units**	$5kHz$	$7.5kHz$	$10kHz$	$12.5kHz$
3000rpm 200$N{\cdot}m$	THD_V	%	15.48	15.15	15.68	16.41
	THD_i	%	1.79	1.64	1.53	1.46
	Torque ripple	%	34.1	29.13	26.51	25.52
6000rpm 50$N{\cdot}m$	THD_V	%	3.23	4.67	7.24	7.01
	THD_i	%	2.2	2.15	1.99	2.15
	Torque ripple	%	46.87	40.55	35.97	33.57

Fig.5.9 illustrated the corresponding power losses in the inverter circuit related to the different switching frequencies. Because of the zero reverse recovery phenomenon from the body diodes of the selected power SiC MOSFET product, only the switching loss in MOSFETs was taken into consideration. In addition, conduction losses were also included in these power losses.

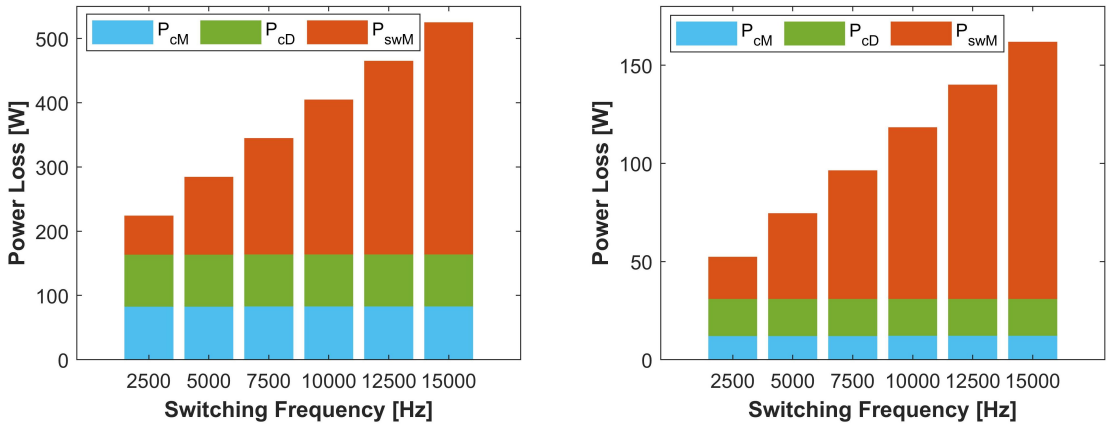

Figure 5.9: The power losses in inverter circuit at 3000rpm, 200$N{\cdot}m$ (left) and 6000rpm, 50$N{\cdot}m$ (right)

Apparently, the total power losses of the inverter circuit exhibits an approximately linear correlation with the f_{sw} values, which mainly arises from the relationship between the switching loss and the f_{sw} values. Moreover, the conduction loss in both SiC MOSFETs and body diodes nearly remains constant.

5.1.3 Switching Frequency Determination

With the expansion of the tested range of switching frequencies from 2.5-20kHz, the trend of the total losses of the entire drive system, including the losses in IPMSM and inverter circuit, changing with the f_{sw} values becomes more evident in Fig.5.10.

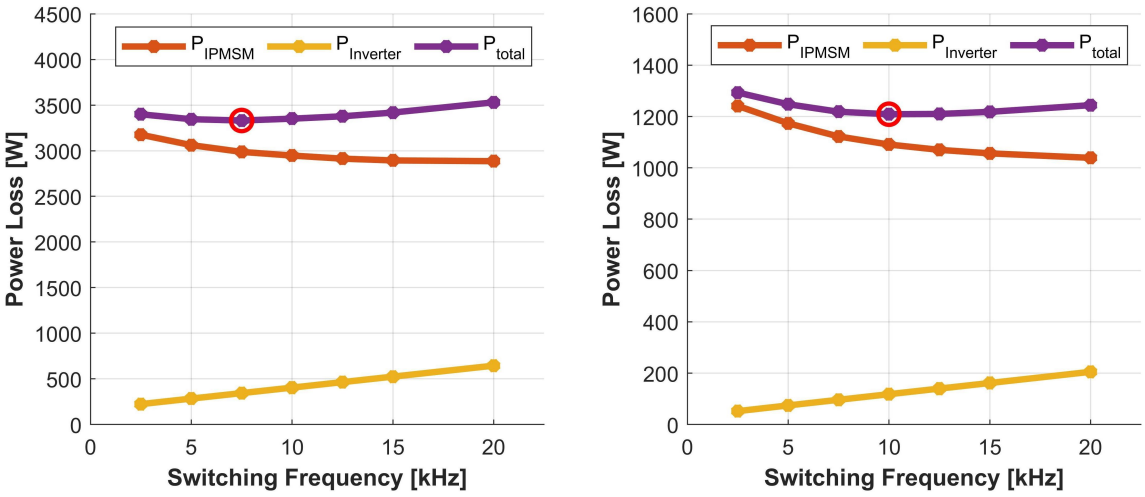

Figure 5.10: The power losses in entire drive system at 3000rpm, 200$N{\cdot}m$ (left) and 6000rpm, 50$N{\cdot}m$ (right)

As illustrated in the figure, as the rise in switching frequency, on one hand, the trend of decline in IPMSM losses gradually slows down; on the other hand, the losses in the inverter circuit increase linearly. Therefore, at a specific switching frequency, the magnitudes of these two trends tend to be balanced, resulting in the lowest total losses for the entire drive system. These f_{sw} values for the example operating points are chosen at 7.5kHz and 10kHz respectively, which marked by the red circles.

5.2 Optimal Switching Scheme of Drive System

This section mainly employs a specific segment of the filed-weakening region as an illustration to reveal the influence of varying switching frequencies on the distribution of system energy efficiency. Furthermore, the optimal switching frequency distribution across the entire operating region will be statistically determined.

5.2.1 Energy Efficiency at Various Switching Frequencies

When the medium-speed and high-speed operating regions of IPMSM are selected for display, and the upper limit of tested switching frequency range is further expanded to 30kHz, the system energy efficiency of this operating area is depicted in Fig.5.11.

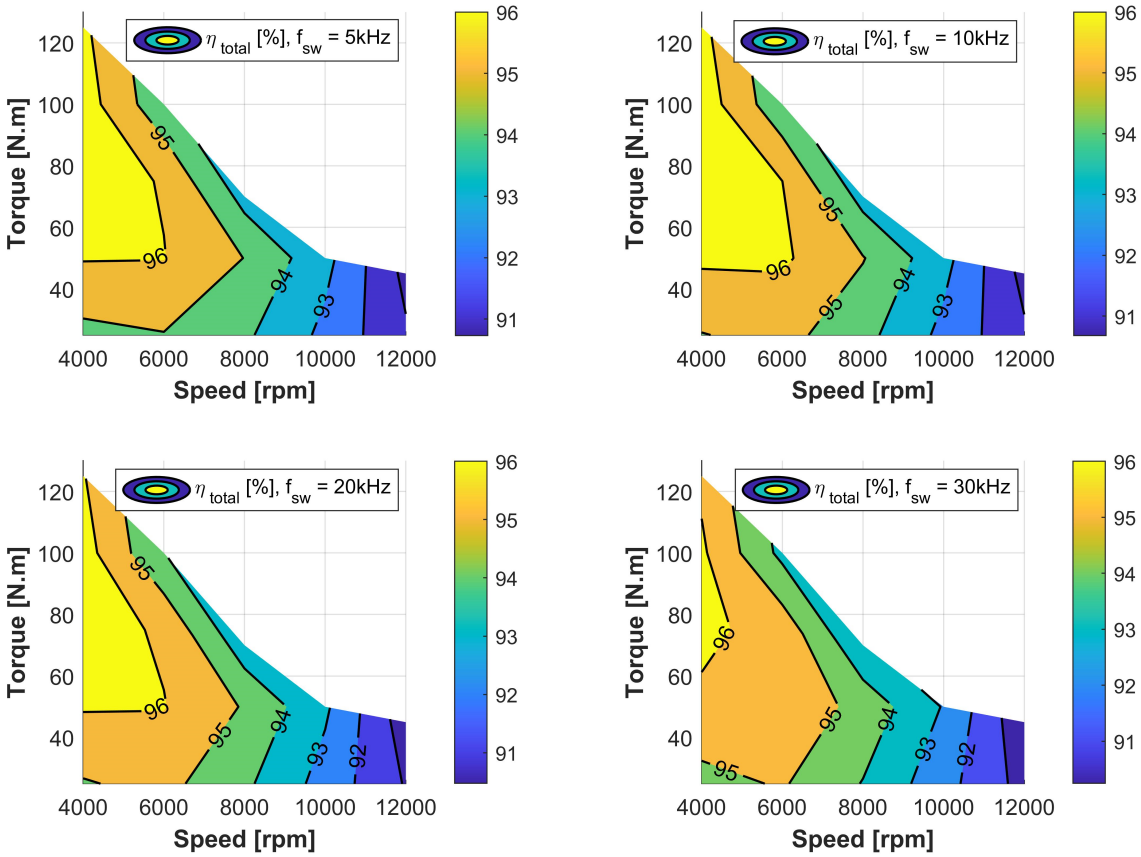

Figure 5.11: The distribution of system energy efficiency across 5-30kHz under 4000-12000rpm

As the switching frequency changes from 5-10kHz, the proportion of the region with energy efficiency higher than 95% experiences a noticeable increase. Subsequently, from 10-20kHz, the energy efficiency across the entire region remains relatively stable. However, when the switching frequency further increases to 30kHz, the proportion of high energy efficiency distribution reduces significantly, while on the contrary, the proportion of efficiency distribution below 92% begins to rise. This indicates that the optimal switching frequency within this region lies approximately between 10kHz and 20kHz.

5.2.2 Determination of The Optimal Switching Scheme

Based on the previously employed methods and further extending its application to the entire operational range, a series of operating points are tested under various switching frequencies. To enhance the energy efficiency of the drive system, the optimal switching scheme within the tested region, along with the corresponding system efficiencies and the proportion of IPMSM losses at total losses, is illustrated in Fig.5.12. Additionally, linear interpolation is employed to determine the data between each operating point.

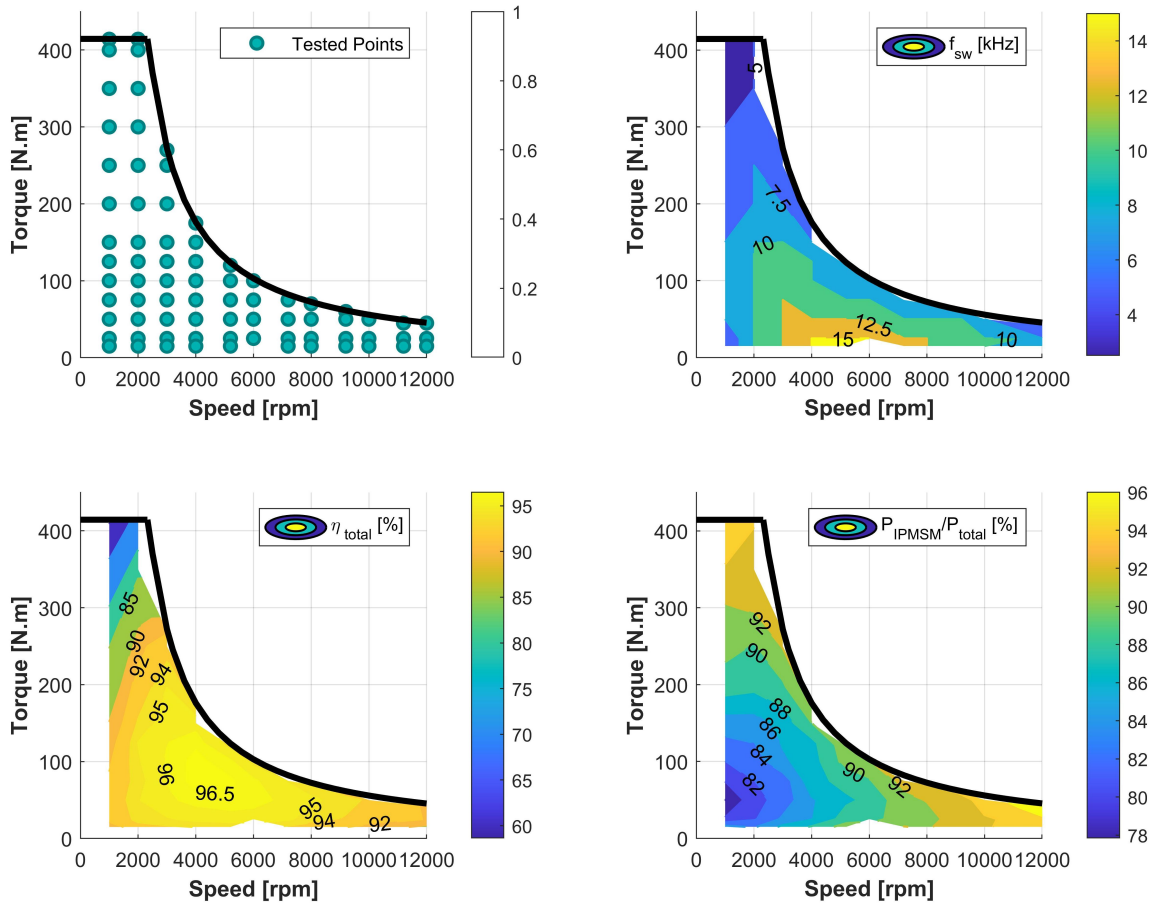

Figure 5.12: Tested operating points (upper left), along with the corresponding optimal switching scheme (upper right), the distribution of system efficiency (lower left) and the distribution of IPMSM losses proportion to the total losses (lower right)

It is worth noting that the distribution of the optimal f_{sw} tends to exhibit a shape characterized by concentric layers, when the f_{sw} value decreases, it becomes closer to the outermost layer. When the motor operates within the medium-speed range between 4000-6000rpm and the output torque is low, a f_{sw} value of 12.5/15kHz yields the highest system efficiency. However, for high torque regions, low f_{sw} values (2.5/5kHz) are generally more suitable. Additionally, in the high-speed region, the optimal f_{sw} value gradually drops as the speed rises.

Correspondingly, the energy efficiency of the drive system touches the highest in the medium-speed region, with the output torque around 100$N{\cdot}m$, reaching close to 96.5%. Moving away from this region, the efficiency decreases successively. While the efficiency drops sharply to about 60% across the high-torque region, due to the rapid rise of copper loss. Moreover, within the low-speed and low-torque region, the IPMSM losses occupy the lowest proportion of the total losses, with the scope between 78-85%. This value increases to more than 95% with higher speed and output torque.

6
Conclusion

In this thesis, an electric drive system centered around an IPMSM drawing inspiration from the 2004 Toyota Prius is constructed using ANSYS platform, which includes a well-matched PI control circuit. Based on the co-simulation with the WBG SiC-based inverter circuit through 3-phase current feeding and PWM feeding, a series of the drive system performances are conducted such as power losses, output torque and induced voltage.

Based on the output results derived from Maxwell simulations and the inverter characteristics provided by the manufacturer, a series of electrical parameters such as L_s and ψ_m are calculated by employing functions in MATLAB, and the process of power loss and heat transfer within the inverter are mathematically modeled. Furthermore, the entire operating region of the IPMSM is delineated by incorporating the constraints of stator current and voltage.

The algorithm of the IPMSM control strategy for minimizing the total motor loss is developed, and its performance is compared in detail with the traditional MTPA control algorithm. Although this strategy can enhance the motor efficiency to a certain extent within the medium-speed region (4000-6000rpm) with low output torque and in the low-speed region (0-2000rpm), the improvements in other regions remains restricted or even negligible (lower than 0.1%). In addition, because of certain shortcomings like the absence of inverter loss data and higher current consumption of loss minimization control, the MTPA algorithm is ultimately selected as the optimal motor current control strategy.

Finally, by varying the switching frequency and documenting the f_{sw} value at which the minimum total loss is attained for each tested operating point, the optimal switching frequency distribution over the entire motor operating area is derived. After testing over 50 operating points, a notable trend emerged: as closer to the medium-speed and low torque region, higher switching frequencies (12.5/15kHz) led to maximal system efficiency. Conversely, as operations move away from this central region, there is a more pronounced reduction in the optimal switching frequency. For instance, the highest torque scenario experiences the optimal switching frequency drop to as low as 2.5kHz.

7
Future Work

In this thesis, only the SPWM control strategy is employed, and the entire electric drive system can be expanded to investigate different switching schemes like SVPWM and THIPWM control strategies. Afterwards, the system efficiency under different control strategies can be compared.

In the process of thermal analysis of power SiC MOSFETs, the type of the heatsink and baseplate can be selected in detail. The simulation of the junction temperature of the SiC MOSFETs will be more accurate if the heat transfer related to them is taken into account in the thermal resistance model.

This work only considers the factor of system energy efficiency when selecting the optimal switching frequency, and sometimes the variations of total power loss caused by the f_{sw} values with the interval of 2.5-5kHz might not be substantial. In this regard, more reference factors can be introduced, such as harmonics.

Analytical equations were employed to calculate the inverter losses. However, acquiring these losses through simulation using the IPMSM model in software can provide more accurate data.

Moreover, exploring the drive system within a drive cycle context can serve as a means to analyze the dynamic behavior of the system. Additionally, an exploration into the impact of turn-on and turn-off transients on the IPMSM can be carried out.

8

Sustainability & Ethics

Many countries have declared that they will gradually replace internal combustion engine vehicles (ICEVs) with EVs over the upcoming decades to meet net-zero carbon emission standards[54]. As the important system inside electric vehicles, the impact of the large-scale application of PMSMs and lithium-ion batteries (LIBs) on the environment and sustainable development should become the focus of attention.

LIBs can be regarded as among the most critical components of EVs and play an significant role in shaping the long-term sustainability of the EV industry. But the extraction of raw materials for LIBs is an environmentally intrusive technology to a certain extent, which will cause damage to the local landscape, groundwater and vegetation. Chile, Argentina, Bolivia, and several other South American countries predominantly employ lithium extraction techniques in salt flats. This technology consumes substantial amounts of water, which not only impacts the well-being of local communities but also poses the risk of toxic substances from lithium mines potentially seeping into water supplies. Additionally, as an significant proportion of the LIB cost, the positive electrode still rely on costly metals like nickel, cobalt, and other valuable metals that with limited reserves. This condition could considerably impact the long-term sustainability of these materials[55].

Similarly, the permanent magnet rare earth materials, represented by NdFeB, is one of the important functional materials for manufacturing PMSMs at present. However, neglecting careful environmental assessment during the phases of mining, processing, and manufacturing can cause significant dust pollution. Additionally, the abandoned mines could possibly lead to natural disasters like landslides, endangering the safety of the local population and their properties.

However, on the other side, when compared to the traditional ICEVs, medium-sized EVs still have lower greenhouse gas emissions throughout the entire life circle, such as vehicle manufacturing, mineral processing, and battery production[56]. Effectively recycling for LIBs can also diminish the necessity for virgin raw materials, thereby reducing the introduction of toxic waste into the environment and water pollution[57]. Moreover, if reliable environmental evaluations can be carried out and the sources of pollution can be reliably controlled before mining these raw materials, the impact of harmful dust and air on local populations will be greatly mitigated.

Bibliography

[1] A. Loganayaki and R. Bharani Kumar. Permanent magnet synchronous motor for electric vehicle applications. In *2019 5th International Conference on Advanced Computing & Communication Systems (ICACCS)*, pages 1064–1069. IEEE, 2019.

[2] Jianglin Zhu, Hyeokjin Kim, Hua Chen, Robert Erickson, and Dragan High efficiency sic traction inverter for electric vehicle applications. In *2018 IEEE Applied Power Electronics Conference and Exposition (APEC)*, pages 1428–1433. IEEE, 2018.

[3] Suleman Yunus, Wenlong Ming, and Carlos E. Ugalde-Loo. Efficiency improvement analysis of a sic mosfet-based pmsm drive system with variable switching frequency. In *2021 23rd European Conference on Power Electronics and Applications (EPE'21 ECCE Europe)*, pages 1–9, 2021.

[4] Alexandre Battiston, El-Hadj Miliani, Serge Pierfederici, and Farid Meibody-Tabar. Efficiency improvement of a quasi-z-source inverter-fed permanent-magnet synchronous machine-based electric vehicle. *IEEE Transactions on Transportation Electrification*, 2(1):14–23, 2016.

[5] Jianhua Wu, Jing Wang, Chun Gan, Qingguo Sun, and Wubin Kong. Efficiency optimization of pmsm drives using field-circuit coupled fem for ev/hev applications. *IEEE Access*, 6:15192–15201, 2018.

[6] Wei Tong. *Mechanical design of electric motors*. CRC press, 2014.

[7] Wawan Purwanto, Risfendra Risfendra, Donny Fernandez, Dwi Sudarno Putra, and Toto Sugiarto. Design comparison of five topologies rotor permanent magnet synchronous motor for high-speed spindle applications. *International Journal of GEOMATE*, 13(40):148–154, 2017.

[8] Anders Kronberg. Design and simulation of field oriented control and direct torque control for a permanent magnet synchronous motor with positive saliency, 2012.

[9] Juha Pyrhönen, Tapani Jokinen, and Valeria Hrabovcova. *Design of Rotating Electrical Machines*. John Wiley Sons, United Kingdom, 2008.

[10] Thomas M. Jahns, Gerald B. Kliman, and Thomas W. Neumann. Interior permanent-magnet synchronous motors for adjustable-speed drives.

IEEE Transactions on Industry Applications, IA-22(4):738–747, 1986. DOI: 10.1109/TIA.1986.4504786.

[11] Joon-Hyoung Ryu, June-Hee Lee, and June-Seok Lee. Switching frequency determination of sic-inverter for high efficiency propulsion system of railway vehicle. *Energies*, 13(19):5035, 2020.

[12] Tapani Jokinen, Valeria Hrabovcova, and Juha Pyrhonen. *Design of rotating electrical machines*. John Wiley & Sons, 2013.

[13] Timijan Velic, Maximilian Barkow, David Bauer, Patrick Fuchs, Johannes Wende, Thomas Hubert, Michael Reinlein, Jan Nägelkrämer, and Nejila Parspour. Efficiency optimization of electric drives with full variable switching frequency and optimal modulation methods. In *2021 17th Conference on Electrical Machines, Drives and Power Systems (ELMA)*, pages 1–6, 2021.

[14] G. Bertotti. General properties of power losses in soft ferromagnetic materials. *IEEE Transactions on Magnetics*, 24(1):621–630, 1988.

[15] Liyi Li, Xuzhen Huang, Baoquan Kao, and Baiping Yan. Research of core loss of permanent magnet synchronous motor (pmsm) in ac servo system. In *2008 International Conference on Electrical Machines and Systems*, pages 602–607, 2008.

[16] Wen Jis-bin Wei Yong-tian, Meng Da-wei. *Thermal exchange of motor*. Mechanical Industry Publishing House, 1998.

[17] Myung-Seop Lim, Ji-Hyun Kim, and J.P. Hong. Experimental characterization of the slinky-laminated core and iron loss analysis of electrical machine. *IEEE Transactions on Magnetics*, 51:1–1, 07 2015.

[18] K. Atallah, D. Howe, P.H. Mellor, and D.A. Stone. Rotor loss in permanent magnet brushless ac machines. In *IEEE International Electric Machines and Drives Conference. IEMDC'99. Proceedings (Cat. No.99EX272)*, pages 60–62, 1999.

[19] H. Polinder and M.J. Hoeijmakers. Eddy-current losses in the segmented surface-mounted magnets of a pm machine. 146:261–266, 1999.

[20] Youhua Wang, Jinguang Ma, Chengcheng Liu, Gang Lei, Youguang Guo, and Jianguo Zhu. Reduction of magnet eddy current loss in pmsm by using partial magnet segment method. *IEEE Transactions on Magnetics*, 55(7):1–5, 2019.

[21] Soo-Hwan Park, Eui-Chun Lee, Jin-Cheol Park, Sung-Woo Hwang, and Myung-Seop Lim. Prediction of mechanical loss for high-power-density pmsm considering eddy current loss of pms and conductors. *IEEE Transactions on Magnetics*, 57(2):1–5, 2021.

[22] A. Fukuma, S. Kanazawa, D. Miyagi, and N. Takahashi. Investigation of ac loss of permanent magnet of spm motor considering hysteresis and eddy-current losses. *IEEE Transactions on Magnetics*, 41(5):1964–1967, 2005.

[23] Juha Pyrhönen, Sami Ruoho, Janne Nerg, Martti Paju, Sampo Tuominen, Harri Kankaanpää, Raivo Stern, Aldo Boglietti, and Nikita Uzhegov. Hysteresis losses in sintered ndfeb permanent magnets in rotating electrical machines. *IEEE Transactions on Industrial Electronics*, 62(2):857–865, 2015.

[24] M. Zordan, P. Vas, M. Rashed, S. Bolognani, and M. Zigliotto. Field-weakening in high-performance pmsm drives a comparative analysis. In *Conference Record of the 2000 IEEE Industry Applications Conference*, pages 1718–1724. IEEE, 2000. DOI: 10.1109/IAS.2000.882112.

[25] Claudio Bianchini, Giorgio Bisceglie, Ambra Torreggiani, Matteo Davoli, Elena Macrelli, Alberto Bellini, and Matteo Frigieri. Effects of the magnetic model of interior permanent magnet machine on mtpa, flux weakening and mtpv evaluation. *Machines*, 11(1):77, 2023. DOI: 10.3390/machines11010077.

[26] Thomas M. Jahns. Flux-weakening regime operation of an interior permanent-magnet synchronous motor drive. *IEEE Transactions on Industry Applications*, IA-23(4):681–689, 1987. DOI: 10.1109/TIA.1987.4504966.

[27] Leopold Sepulchre, Maurice Fadel, Maria Pietrzak-David, and Guillaume Porte. Mtpv flux-weakening strategy for pmsm high speed drive. *IEEE Transactions on Industry Applications*, 54(6):6081–6089, 2018.

[28] Ned Mohan, Tore M Undeland, and William P Robbins. *Power electronics: converters, applications, and design*. John wiley & sons, 2003.

[29] Tiefu Zhao, Jun Wang, Alex Q. Huang, and Anant Agarwal. Comparisons of sic mosfet and si igbt based motor drive systems. In *2007 IEEE Industry Applications Annual Meeting*, pages 331–335, 2007.

[30] Leon M Tolbert, Burak Ozpineci, Syed K Islam, and Fang Z Peng. Impact of sic power electronic devices for hybrid electric vehicles. *SAE Transactions*, pages 765–771, 2002.

[31] B. Ozpineci and L.M. Tolbert. Characterization of sic schottky diodes at different temperatures. *IEEE Power Electronics Letters*, 1(2):54–57, 2003.

[32] K Vinoth Kumar, Prawin Angel Michael, Joseph P John, and S Suresh Kumar. Simulation and comparison of spwm and svpwm control for three phase inverter. *ARPN journal of engineering and applied sciences*, 5(7):61–74, 2010.

[33] George J Wakileh. *Power systems harmonics: fundamentals, analysis and filter design*. Springer Nature, 2019.

[34] TRAN Hoan, Bernardo COUGO, and Gilles SEGOND. Loss reduction of wbg inverter by pwm techniques for the motion control of pmsm. In *2019 IEEE 4th International Future Energy Electronics Conference (IFEEC)*, pages 1–9. IEEE, 2019.

[35] Yi Deng, Zach Pan, Harish Suryanarayana, Arun Kadavelugu, Liming Liu, Christopher Belcastro, and Esa-Kai Paatero. Power loss evaluation for active and magnetic components in a sic mosfet-based power electronic system. In

2017 IEEE Energy Conversion Congress and Exposition (ECCE), pages 3228–3234, 2017.

[36] Dusan Graovac, Marco Purschel, and Andreas Kiep. Mosfet power losses calculation using the data-sheet parameters. *Infineon application note*, 1:1–23, 2006.

[37] Ali Rabiei. Energy efficiency of an electric vehicle propulsion inverter using various semiconductor technologies. 2013.

[38] Zhen Hu, Mingxing Du, and Kexin Wei. Online calculation of the increase in thermal resistance caused by solder fatigue for igbt modules. *IEEE Transactions on Device and Materials Reliability*, 17(4):785–794, 2017.

[39] Ke Heng, Xin Yang, Xinlong Wu, Junjie Ye, and Guoyou Liu. A temperature-dependent physical thermal network model including thermal boundary conditions for sic mosfet module. *IEEE Transactions on Electron Devices*, 69(8):4444–4452, 2022.

[40] Infineon Technologies. Transient thermal measurements and thermal equivalent circuit models, 2018.

[41] Dusan Graovac. Parallel operation of power mosfets. *Infineon application note*, 1:1–7, 2009.

[42] Team Nexperia. Using power mosfets in parallel. *Nexperia application note*, 1:1–18, 2015.

[43] Vishal Virani, Swapnil Arya, Jaydeepsinh Baria, et al. Modelling and control of pmsm drive by field oriented control for hev. *C, Modelling and Control of PMSM Drive by Field Oriented Control For HEV (February 12, 2019). Advances in Power Generation from Renewable Energy Sources (APGRES)*, 2019.

[44] Asri Samar, Pais Saedin, A. Idzwan Tajudin, and Nor Adni. The implementation of field oriented control for pmsm drive based on tms320f2808 dsp controller. In *2012 IEEE International Conference on Control System, Computing and Engineering*, pages 612–616, 2012.

[45] Hakan Celik and Tevfik Yigit. Field-oriented control of the pmsm with 2-dof pi controller tuned by using pso. In *2018 International Conference on Artificial Intelligence and Data Processing (IDAP)*, pages 1–4, 2018.

[46] Mohammad Marufuzzaman, Mamun Bin Ibne Reaz, Labonnah Farzana Rahman, and Tae Gyu Chang. High-speed current dq pi controller for vector controlled pmsm drive. *The Scientific World Journal*, 2014, 2014.

[47] Wahyu Kunto Wibowo and Seok-kwon Jeong. Genetic algorithm tuned pi controller on pmsm simplified vector control. *Journal of Central South University*, 20:3042–3048, 2013.

[48] Hiva Nasiri, Ahmad Radan, Abbas Ghayebloo, and Kiarash Ahi. Dynamic modeling and simulation of transmotor based series-parallel hev applied to toy-

ota prius 2004. In *2011 10th International Conference on Environment and Electrical Engineering*, pages 1–4, 2011.

[49] ANSYS. Ansys maxwell 2022: low-frequency electromagnetic field simlation, 2022. [online] accessed April 11, 2023 `https://www.ansys.com/Products/Electronics/ANSYS-Maxwell`.

[50] Audrey Dearien, Shuang Zhao, Chris Farnell, and H. Alan Mantooth. Slew rate control of high-voltage sic mosfets using gate resistance vs. intermediate voltage level. In *2019 10th International Conference on Power Electronics and ECCE Asia (ICPE 2019 - ECCE Asia)*, pages 2146–2152, 2019.

[51] Zhuxian Xu, Fan Xu, Puqi Ning, and Fred Wang. Development of a 30 kw si igbt based three-phase converter for operation at 200 °c with high temperature coolant in hybrid electric vehicle applications. In *2013 Twenty-Eighth Annual IEEE Applied Power Electronics Conference and Exposition (APEC)*, pages 3027–3033, 2013.

[52] Jianhua Wu, Jing Wang, Chun Gan, Qingguo Sun, and Wubin Kong. Efficiency optimization of pmsm drives using field-circuit coupled fem for ev/hev applications. *IEEE Access*, 6:15192–15201, 2018.

[53] Emma Arfa Grunditz and Torbjörn Thiringer. Electric vehicle igbt power module sizing and drive cycle energy efficiency for various switching frequencies-based on a scalable module model. In *2018 20th European Conference on Power Electronics and Applications (EPE'18 ECCE Europe)*, pages P.1–P.10, 2018.

[54] Zhijie Yang, Haibo Huang, and Feng Lin. Sustainable electric vehicle batteries for a sustainable world: Perspectives on battery cathodes, environment, supply chain, manufacturing, life cycle, and policy. *Advanced Energy Materials*, 12(26), 5 2022.

[55] Micah S Ziegler, Juhyun Song, and Jessika E Trancik. Determinants of lithium-ion battery technology cost decline. *Energy & Environmental Science*, 14(12):6074–6098, 2021.

[56] R Nealer and TP Hendrickson. Review of recent lifecycle assessments of energy and greenhouse gas emissions for electric vehicles. *Current Sustainable/Renewable Energy Reports*, 2:66–73, 2015.

[57] Dominic A. Notter, Marcel Gauch, Rolf Widmer, Patrick Wäger, Anna Stamp, Rainer Zah, and Hans-Jörg Althaus. Contribution of li-ion batteries to the environmental impact of electric vehicles. *Environmental Science & Technology*, 44(17):6550–6556, 2010. PMID: 20695466.

A

Appendix

The aim for creating the same electric drive system model in MATLAB/Simulink is to verify the accuracy of the FEM model built in ANSYS platform, due to the much faster simulation process of Simulink.

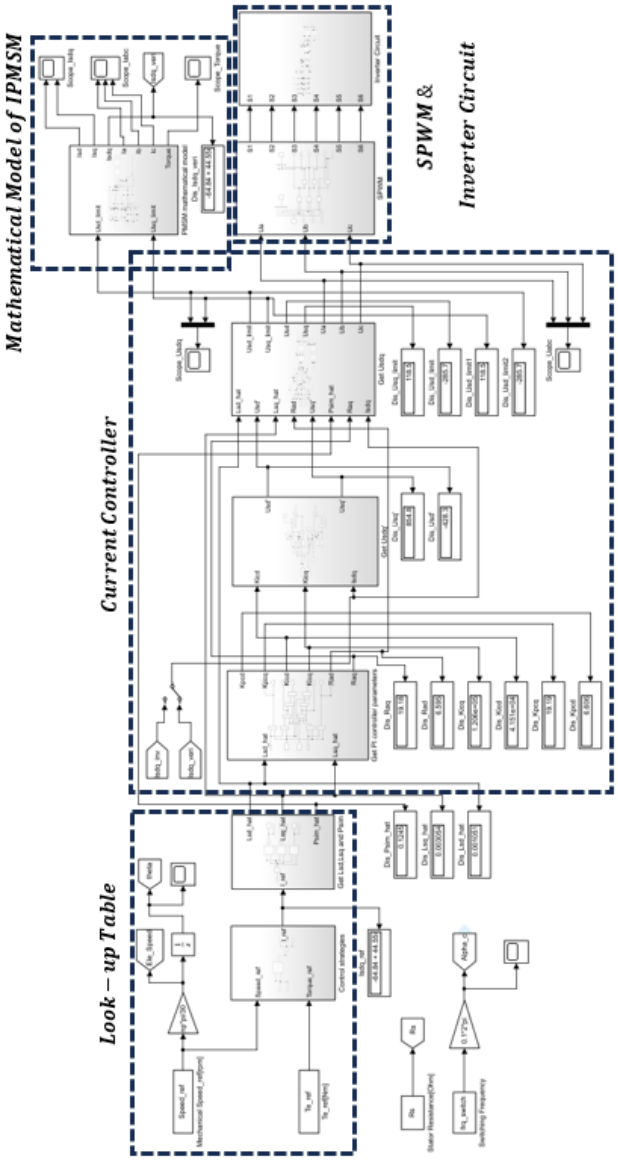

Figure A.1: Entire electrical drive system built in Simulink, mainly including an mathematical model of IPMSM, a 3-phase inverter circuit and a controller circuit

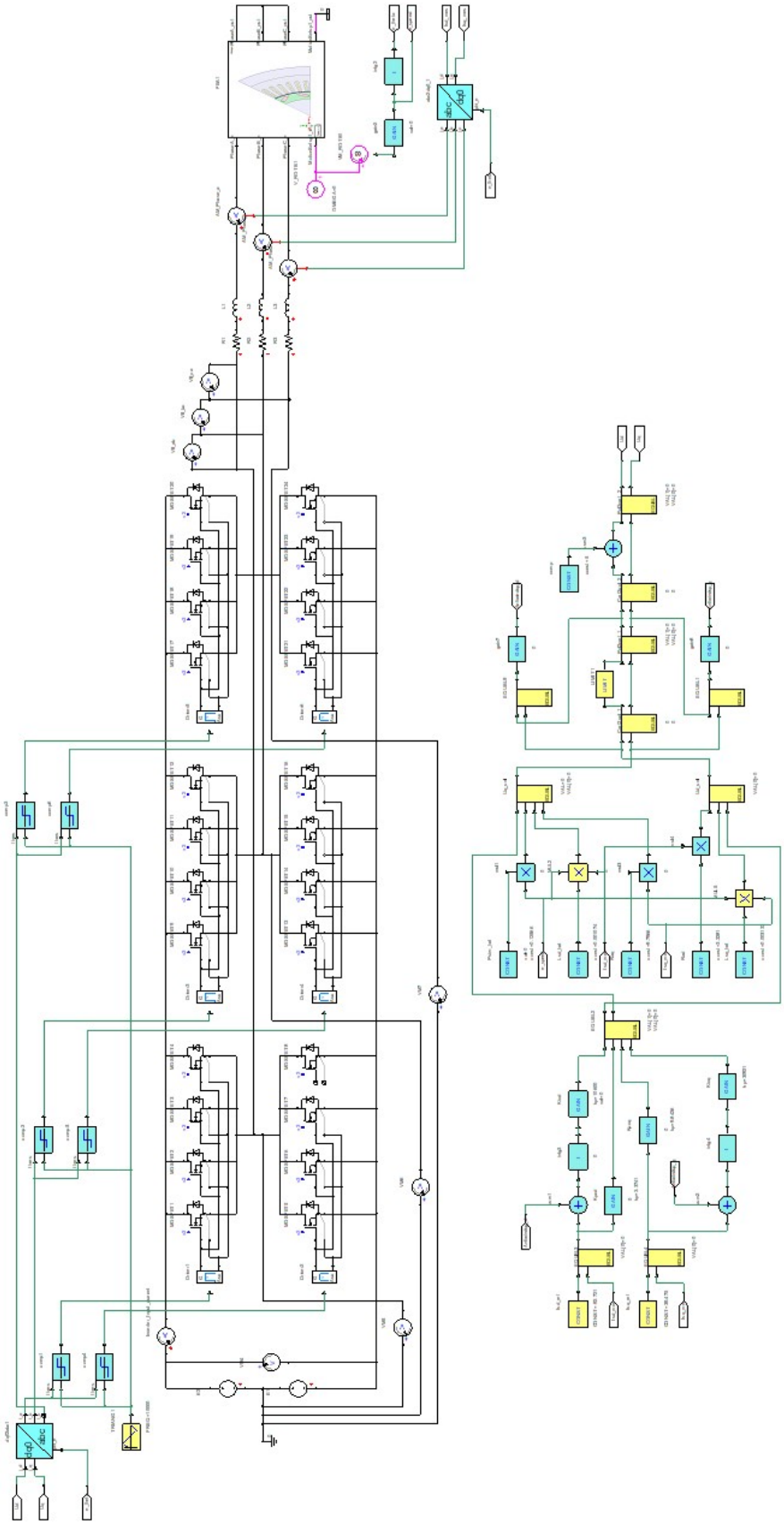

Figure A.2: Entire electrical drive system built in ANSYS platform, mainly including an FEM model of IPMSM, a 3-phase inverter circuit and a controller circuit

DEPARTMENT OF SOME SUBJECT OR TECHNOLOGY
CHALMERS UNIVERSITY OF TECHNOLOGY
Gothenburg, Sweden
www.chalmers.se

CHALMERS
UNIVERSITY OF TECHNOLOGY